PNAS

Supplementary Information for

Scavenger Receptor-Targeted Plaque Delivery of MicroRNA-Coated Nanoparticles for Alleviating Atherosclerosis

Qianqian Bai, [†] *Yu Xiao,* [†] *Huiling Hong,* [‡] *Xiaoyun Cao,* [‡] *Lei Zhang,* [†] *Ruifang Han,* [†] *Leo Kit Cheung Lee,* [†] *Evelyn Y. Xue,* [§] *Xiao Yu Tian,* [*,‡] *Chung Hang Jonathan Choi*[*,†]

[†]Department of Biomedical Engineering, [‡] School of Biomedical Sciences, [§] Department of Chemistry, The Chinese University of Hong Kong, Shatin, New Territories, Hong Kong SAR

*Xiao Yu Tian, *Chung Hang Jonathan Choi
Email: xytian@cuhk.edu.hk, jchchoi@cuhk.edu.hk

This PDF file includes:

SI Materials and Methods

Synthesis and characterization of polyethylene glycol-coated superparamagnetic iron oxide nanoparticles (PEG-SPIONs). PEG-SPIONs with carboxylate groups were prepared by thermal decomposition following our published protocol *(1))* Briefly, 262.5 mg of ferric acetylacetonate [$Fe(acac)_3$; Sigma-Aldrich] was added to 1 mL of oleylamine (Sigma-Aldrich) and 3.0 g of dicarboxyl-terminated PEG (HOOC-PEG-COOH; molecular weight: 2000 Da; Sigma-Aldrich) in 12.5 mL of diphenyl ether (Sigma-Aldrich). After aging the mixture at 80°C under nitrogen for 4 h, the reaction proceeded under reflux at 255°C for 30 min. By redispersing PEG-SPIONs in ethanol and subsequently precipitating with chilled diethyl ether (RCI Labscan) for three cycles, the nanocrystals were purified and collected for further characterization. Cyanine 5 amine (Lumiprobe) were used to generate Cy5-tagged PEG-SPIONs *via* DCC/NHS chemistry, respectively. Briefly, 5 mg of carboxylated PEG-SPIONs was dissolved in 0.5 mL of anhydrous dimethyl sulfoxide (DMSO; J&K Seal) and activated with 4.12 mg *N*,*N′*-dicyclohexylcarbodiimide (DCC; Sigma-Aldrich) and N-hydroxysuccinimide 3.45 mg of (NHS; Sigma-Aldrich) for 2 h. Next, 6 nmol Cy5-NH_2 was added to the reaction mixture and left shaking overnight. Cy5-SPIONs were dialyzed against DEPC-treated (BIA0881, J&K) nanopure water by using a dialysis membrane (molecular weight cutoff size: 50000 Da; Yi Bo Biological) for 2-3 days, passed through 0.2 μm aqueous syringe filters, and resuspended in Nanopure water. The physical size and morphology of the resultant PEG-SPIONs were examined by transmission electron microscopy (TEM) at 100 kV voltage (Hitachi H7700). The hydrodynamic size and surface charge of NPs were measured by dynamic light scattering (DLS, Zetasizer Nano ZS90, Malvern). The concentration of PEG-SPIONs were analyzed by ICP-MS (Agilent 7900).

Preparation of microRNA-functionalized SPIONs (miR-SPIONs). Amine-modified, phosphorothioated (PS) microRNA strands (miR-NH_2; Idobio) were covalently attached to carboxylate-terminated PEG-SPIONs. Typically, 5 mg of carboxylated PEG-SPIONs was dissolved in 0.5 mL of DMSO and activated with 4.12 mg DCC and 3.45 mg of NHS for 2 h. Next, 6 nmol miR-NH_2 was added to the reaction mixture and left shaking overnight. miR-SPIONs were processed under same procedure with Cy5-SPIONs. The hydrodynamic size and surface charge of the NPs were measured by DLS. Conjugation of miRs to PEG-SPIONs was confirmed by gel electrophoresis. The loading of miR on the SPION core was calculated based on a fluorescence-based assay, following literature precedent *(1)*. The concentration of Cy5-labeled miR before and after their DCC/NHS reaction with PEG-SPIONs was measured by plate reader (MULTISKAN GO, Thermo Scientific), followed by dividing the difference in miR concentration by the concentration of PEG-SPIONs to obtain the loading of miR. See sequence of oligonucleotides in Table S2.

Agarose gel electrophoresis. 6 μL of 50 mg/mL PEG-SPIONs or miR-SPIONs (with or without Cy5) and 2 μL of 15% (w/v) Ficoll® 400 (Sigma) were loaded onto a 1% agarose (Baygene Biotech) gel in 0.5× TBE buffer. The bands were resolved by electrophoresis at 120 V for 25 min using a Mini-300 (Major Science) power supply.

Denaturing polyacrylamide-urea gel electrophoresis (urea-PAGE). In each sample, 1 μL of 6X DNA Gel Loading Dye (Thermo Fisher Scientific) were added to 5 μL of free miR-146a, PEG-SPIONs, miR-146a-SPIONs, miR-nc-SPIONs, abasic-SPIONs, or a physical mixture of PEG-SPIONs and free miR-146a in diethyl pyrocarbonate (DEPC; J&K)-treated Nanopure water. The mass of nucleic acid, in free or NP forms, was kept constant at 120 ng per sample. The amount of SPIONs added was kept constant at 1.5 μg of Fe per sample. Each 6 μL sample and 10 μL of microRNA marker (New England Biolabs) were denatured at 95°C for 5 min. After cooling down to room temperature (RT), the samples were kept on ice until use. Also, 10 μL of microRNA marker (New England Biolabs) was similarly denatured, cooled, and kept on ice. Next, a 15% (w/v) denaturing polyacrylamide-urea gel was prepared by adding 4.8 g of urea (TCI) in 5 mL 30% (w/v) acrylamide/bis solution (Bio-Rad) and 1 mL 10X TBE buffer (Beyotime). After gelation at RT for ~10 min, each sample (6 μL) or microRNA marker (10 μL) was loaded into each well of the denaturing PAGE gel. After resolving the loaded gel at 40 V for 6 h using Power PAC 300 (Bio-Rad), the gel was stained with 10 mL of 5X SYBR Gold Nucleic Acid Gel Stain (Thermo Fisher Scientific) for 5 min. The stained gel was imaged under “SYBR Gold” mode using the ChemiDocTM Touch Imaging System (Bio-Rad) to reveal the free oligonucleotides inside the gel.

Cell culture. RAW 264.7 (mouse macrophage; ATCC) and C166 (mouse endothelial; ATCC) cells were cultured in complete Dulbecco's Modified Eagle Medium (DMEM; Gibco) [i.e., DMEM supplemented with 10% fetal bovine serum (FBS; Gibco) and 1% penicillin-streptomycin (Gibco)] and maintained at 37°C and 5% CO_2.

Cellular uptake by TEM imaging. Freshly harvested cell pellets were fixed with glutaraldehyde (2.5% in phosphate buffer; pH = 7.2-7.4; J&K Scientific) for 2 h and stained by osmium tetroxide [1%; Electron Microscopy Sciences (EMS)] for another 2 h. Pellets were dehydrated in increasing ethanol gradients and propylene oxide, embedded in Epon 812 resins (EMS), and polymerized at 55°C for 2 d. Ultrathin sections of 70 nm thick were deposited onto 200-mesh copper grids (EMS) and stained with 4% uranyl acetate (EMS, in 50% methanol/water) and Reynolds lead citrate (Sigma) for TEM imaging at a beam voltage of 100 kV (Hitachi H7700).

Cytotoxicity of SPIONs. Cells were plated in a 96-well plate at a density of 10^5 cells per well 24 h before the experiment. The cells were incubated with 5 nM SPIONs in medium for 24 h at the same concentration used in the cellular uptake experiments. After removing the medium and rinsing the cells, the alamarBlue reagent (Invitrogen) was used to test the cell viability according to the manufacturer's instructions by measuring the optical absorbance at 570 nm and 600 nm by plate reader. Reported data represent mean ± SEM from six independent experiments.

Preparation of cell samples for *in vitro* efficacy by qRT-PCR. Pre-seeded in 6-well plates and grown to ~80% confluency, cells were transfected with 1 mL of DMEM supplemented with 1% FBS and containing either 5 nM miR-146a-SPIONs or 5 nM non-targeting control miR-nc-SPIONs for 24 h. Next, the NP-containing medium was replaced by 1 mL of NP-free DMEM supplemented with 1% FBS. RAW 264.7 cells were treated with 100 ng/mL lipopolysaccharide (LPS; Sigma, from E. coli) and C166 cells were treated with 10 ng/mL tumor necrosis factor alpha (TNF-α; Peprotech) for another 24 h before harvest. RNA was isolated using Trizol (Thermo Fisher Scientific) and reverse-transcribed using the RevertAid First Strand cDNA Synthesis Kit (Thermo Fisher Scientific) to generate cDNA. qRT-PCR was performed on the ViiATM 7 System using TB SYBR Green Premix Ex Taq kit (Takara) following the manufacturer's instructions. Transcript levels were analyzed using the $\Delta\Delta C_T$ method and normalized to the house-keeping gene glyceraldehyde 3-phosphate dehydrogenase (GAPDH). Gene expression was quantified using pre-designed primers purchased from Shanghai Rui Mian Bio Tech (see sequences below).

Gene	Forward sequence (5' to 3')	Reverse sequence (5' to 3')
Mouse GAPDH	ATGGTGAAGGTCGGTGTGAA	GAGGTCAATGAAGGGGTCGT
Mouse Traf6	CTGACGGTAAAGTGCCCAAA	CTTCTGGAAAGGACGTTGGC
Mouse Irak2	TGAAAACTGATGCACCCGAC	GCTTGGACGACATCTGCTTC
Mouse Irf5	TGGGTCAACGGGGAAAAGAA	ACCCCTTCAGTGTACTTCCC
Mouse Il1b	TGGACCTTCCAGGATGAGGAC	GTTCATCTCGGAGCCTGTAGTG
Mouse Tnfa	GGTGCCTATGTCTCAGCCTCTT	GCCATAGAACTGATGAGAGGGAG
Mouse Mcp1	CATCCACGTGTTGGCTCA	GATCATCTTGCTGGTGAATGAGT

Mouse Icam1	AAACCAGACCCTGGAACTGCAC	GCCTGGCATTTCAGAGTCTGCT
Mouse Vcam1	ACAGACAGTCCCCTCAATGG	TCCTCAAAACCCACAGAGCT

Animal model. All animal procedures followed the guidelines stipulated by the Animal Experimentation Ethics Committee (AEEC) at The Chinese University of Hong Kong (CUHK) (AEEC No.19/259/GRF). ApoE$^{-/-}$ mice were purchased from the Jackson Laboratory and shipped to the CUHK Laboratory Animal Services Centre (LASEC). ApoE$^{-/-}$ male mice (5–6 weeks old) were fed with a high cholesterol diet (HCD, Research Diets rodent diet D12336) for 9–12 weeks to induce the formation of atherosclerotic plaques in the aorta and aortic root.

Expression of miR-146a in cells or the aorta by qRT-PCR. Relative expression of mature mmu-miR-146a was evaluated by using the QuantiMir RT kit (System Biosciences, RA420A-1) followed by qRT-PCR analysis according to the manufacturer's instruction, but with minor modifications. Briefly, the microRNAs were tagged with poly A tail, annealed with an oligo-dT adaptor, and converted into first strand cDNA. qRT-PCR was then performed with the following primers by using the TB SYBR Green Premix Ex Taq kit (Takara) in a StepOnePlus (Applied Biosystems): miR-146a forward, 5′-TAG GAA CTG AAT TCC ATG GGT T-3′; U6 forward, 5′-CTC GCT TCG GCA GCA CA-3′, and a universal reverse primer supplied in the assay kit. The forward primer sequences were designed based on the miRbase database (www.mirbase.org). The analysis was performed at 95°C for 5 min, followed by 50 cycles at 95°C for 10 s and at 60°C for 10 s. Fluorescence signal was acquired at the end of the elongation step of every PCR cycle to monitor the increasing amount of amplified DNA. Transcript levels were analyzed using the ΔΔCT method and normalized to U6. All the measurements were conducted in triplicates. Melting curve analysis was performed after the amplification phase to eliminate any nonspecific amplification or primer dimer formation.

Cellular uptake by ICP-MS. Pre-seeded in 24-well plates until the cell population reached ~70% confluence, cells were incubated with 0.3 mL of SPIONs (formulated at a concentration of 5 nM in complete DMEM) over different durations of time. After that, the cells were rinsed with phosphate-buffered saline (PBS) twice and trypsinized (0.25% Trypsin-EDTA, Gibco) for cell counting by a hemocytometer. The cells were further centrifuged at 8000 rpm for 5 min to form a pellet for further ICP-MS analysis of the Fe content associated with the cells. The cell pellets were digested in 0.3 mL of concentrated trace-metal grade HNO_3 (BDH ARISTAR) at RT overnight. After adding 5.7 mL of 2% HNO_3, the Fe content of the resultant solution was measured by ICP-MS (Agilent 7900) after subtracting the background Fe content of untreated cells. Data are shown as the mean ± standard error of the mean (SEM) from three biological replicates (i.e., 3 wells per treatment group).

Pharmacological inhibition. Seeded in 24-well plates, cells were pre-treated with 300 μL of OptiMEM that contains fucoidan (50 μg/mL, Santa Cruz) for 1 h. After removing the inhibitor-containing medium, 0.3 mL of serum-containing DMEM that contains the same inhibitor at the original concentration and 5 nM SPIONs were subsequently added to the cells. After 2 h of incubation, the SPIONs- and inhibitor-containing medium was removed, and the cells were rinsed with PBS. Cell pellets were harvested for ICP-MS analysis.

Histology. The aortic roots with the upper heart were embedded in Tissue-Tek optimal cutting temperature (OCT) compound (Sakura Finetek), stored at −80 °C, and serially sectioned into 10 μm-thick slices. Cryo-sections were serially collected when the three aortic valves were recognized, generating a total of 50-60 slices per aortic root with the three leaflets of aortic valves. Other tissues like the lower heart, liver, spleen, and kidney were fixed in 10% buffered formalin for 48 h, then dehydrated in ethanol, cleared in xylene, and embedded in paraffin blocks. Paraffin-embedded tissues were cut into sections of 5 μm thick by using a rotary microtome (Leica RM 2235) and mounted on Superfrost PlusTM Adhesion microscope slides (Thermo Scientific).

Tissue-level distribution by confocal IF. The aortic roots with the upper heart were collected from plaque-bearing mice and incubated in serum-containing DMEM which contains

5 nM Cy5-labeled PEG-SPIONs or miR-146a SPION for 2 h with gentle shaking (200 rpm). The aortic roots with the upper heart were embedded in OCT, stored at −80°C for cryosection to verify the association of Cy5-SPIONs to the aortic macrophages and ECs in the plaque. After fixation, cryosections were blocked with 5% goat serum (Vector Laboratories) for 30 min, and then stained with PBS containing 5% goat serum and primary antibodies at 4°C overnight. The primary antibodies include mouse monoclonal primary antibody against CD68 (5 μg/mL, ab31630, Abcam), mouse monoclonal primary antibody against ICAM-1 (4 μg/mL, SC 107; Santa Cruz), and rabbit monoclonal primary antibody against CD204 (12.8 μg/mL, ab123946; Abcam). CD68 and ICAM-1 were visualized with Alexa Fluor 532-conjugated goat anti-mouse secondary antibody (5 μg/mL, A11002; Thermo Scientific), and CD204 was visualized with Cy3-conjugated goat anti-rabbit secondary antibody (5 μg/mL, A10520; Thermo Scientific) at RT for 1 h. Next, the slides were stained by 1 μg/mL DAPI for 10 min, washed and mounted with Antifade Mountant (P36980; Thermo Scientific) for visualization under a confocal laser scanning microscope (TCS SP8, Leica). The excitation wavelengths of DAPI, Alexa Fluor 532, and Cy3 are 405 nm, 532 nm, and 550 nm, respectively. The emission wavelength ranges of DAPI, Alexa Fluor 532 and Cy3 are 415–500 nm and 542–650 nm, 570–590 nm, respectively. To confirm the specificity of immunostaining and eliminate any bias of tissue autofluorescence, cryosections of the aortic root with the upper heart from healthy untreated C57BL/6 mice were similarly prepared and stained using the same primary and secondary antibodies as above, with the addition of rat monoclonal primary antibody against CD144 (20 μg/mL, 14-1441-82; Invitrogen). CD144 was visualized with Alexa Fluor 647-conjugated goat anti-rat secondary antibody (4 μg/mL, A21247; Thermo Scientific) under confocal imaging with excitation wavelength of 647 nm and emission wavelength range of 670–690 nm. Images were taken at the same laser settings for each fluorophore type (DAPI, AF 532, Cy3, and AF 647).

***Ex vivo* cellular-level distribution by flow cytometry.** Aortas dissected from plaque-bearing mice were longitudinally cut and incubated with 5 nM Cy5-labeled PEG-SPIONs or miR-146a-SPIONs for 2 h with gentle shaking (200 rpm). After washed by PBS for 3 times, the aortas were placed in 1x Hanks' Balanced Salt Solution (HBSS; Sigma-Aldrich) containing collagenase I (450 U/mL; Worthington, collagenase IV (125 U/mL; Worthington, DNase I (40 U/mL; Worthington), and hyaluronidase (60 U/mL; Worthington) at 37°C with gentle shaking (200 rpm) for 1 h 25. Digested aortas were minced and filtered (70 μm; BD Biosciences) to generate a single-cell suspension and centrifuged at 4°C at 1800 rpm for 10 min. Pelleted cells were resuspended in FACS buffer (2 mM EDTA and 1% FBS in PBS). After incubating the single cell suspension in 1 μg/mL Fc-block (BioLegend; 101302) and Live/Dead Fixable Aqua (Thermo Fisher Scientific; L34966) for 25 min, the cells were stained with different sets of antibodies (see below) at 4°C for 30 min in the dark. To probe the association of Cy5-labeled NPs to different aortic cell types, cells were washed and stained with CD45 (FITC; 30-F11; Ebiosciences; 11-0451-82), CD144 (BV605; BD Biosciences; 748261), CD204 (PE; Biolegend; 154709), CD64 (PE/Cy7; Biolegend; 139314), and Ly6C (PerCP-Cy5.5; Biolegend; 128012). Macrophages were gated as $CD45^{+}CD64^{+}$ cells. ECs were gated as $CD45^{-}CD144^{+}$ cells. Monocyte-macrophages were gated as $CD45^{+}CD64^{mid}Ly6C^{hi}$. Samples were fixed in FluoroFix buffer (BioLegend) and kept at 4°C before analyzed by a flow cytometer (BD FACSAria™ Fusion. Data were analyzed by the FlowJo software (Tree Star).

***In vivo* cellular-level distribution by flow cytometry.** Mice received an i.v. injection of Cy5-labeled miR-146a-SPIONs, Cy5-labeled miR-nc-SPIONs (10 mg/kg Fe and 1.5 mg/kg miR), Cy5-labeled miR-146a (1.5 mg/kg miR) complexed with Lipofectamine 3000 (60 μg/kg, Invitrogen) encapsulated or free Cy5 dye at the same intensity of fluorescence via the tail vein. 2 h post-injection, the mice were sacrificed and perfused with PBS. Aorta was digested same as *ex vivo* preparation (see Supplementary Information). The dissected livers were sliced into small pieces and placed in RPMI 1640 medium (Thermo Fisher Scientific) containing collagenase IV (125 U/mL; Worthington) and DNase I (60 U/mL; Worthington) suspended in at 37°C with gentle shaking for 1 h. Livers were dissociated with the gentle MACS dissociator system (Miltenyi Biotec) and incubated at 37°C for another 15 min. Digested livers were minced and filtered (70 μm; BD Biosciences) to generate a single-cell suspension. Liver cells were treated with red blood cell (RBC) lysis buffer (BioLegend; 420302) for 10 min at RT. The staining and gating processes are same with *ex vivo* flow studies.

Blood pharmacokinetics. Mice received an intravenous (i.v.) injection of SPIONs at a concentration of 10 mg Fe/kg mouse via the tail vein. A total of 0.5 mL of blood was

withdrawn by cardiac puncture from mice that were sacrificed at different time points, and the blood samples were stored inside EDTA-coated tubes (Becton Dickinson). After centrifugation at 1500 ×g for 10 min, 0.2 mL of the blood plasma in the supernatant was collected and lysed by adding 0.5 mL of trace metal grade 65% HNO_3. The lysate was diluted to a 2% HNO_3 solution with Nanopure water and passed through a 0.2 μm hydrophilic syringe filter for measurement of Fe content by ICP-MS. Blood collected from uninjected mice was used to account for the background Fe content. Data were fitted to a mono-exponential decay model by using the Prism Graphpad software.

***Ex vivo* imaging of aorta.** Plaque-bearing ApoE$^{-/-}$ mice that were fed with a high-cholesterol diet for 12 weeks received an i.v. injection of Cy5-labeled PEG-SPIONs (10 mg/kg Fe), Cy5-labeled miR-146a-SPIONs (10 mg/kg Fe and 1.5 mg/kg miR), or free Cy5 dye at the same fluorescence intensities via the tail vein. 2 h post-injection, mice were sacrificed and perfused with 50 mL of PBS for 5–10 min each to remove any endogenous iron as much as possible. Ex vivo fluorescence imaging of the excised aorta was performed using an Odyssey infrared imaging system (excitation wavelength: 680 nm, emission wavelength: $\geqslant$ 700 nm). The images were digitised and analysed by the Odyssey imaging system software (no. 9201-500).

Extraction of plasma proteins from SPIONs. In a typical reaction of 60 μL, 25 nM PEG-SPIONs or miR-146a-SPIONs were incubated in fresh blood plasma collected from plaque-bearing ApoE$^{-/-}$ mice that were fed with high-cholesterol diet for 12 weeks at 37°C for 2 h to allow for protein adsorption. Next, the protein-coated SPIONs were washed in PBS to remove unbounded proteins by three rounds of centrifugation at 13500 rpm at 4°C and resuspended in PBS containing 0.05% v/v Tween 20 (Sigma). After pelleting the washed SPIONs, the supernatant was discarded, leaving 25 μL of the SPIONs pellet. 10 μL of Laemmli sample buffer (4×; Bio-Rad) and 5 μL of 4.8 M dithiothreitol (DTT) were added to the NP pellet, followed by incubation at 70°C for 1 h with shaking to release the adsorbed proteins. After pelleting the SPIONs by centrifugation at 13500 rpm at 4°C, the supernatant containing the desorbed proteins was transferred to a new tube.

Protein purification for proteomics analysis. Desorbed proteins were mixed with 5× loading buffer (Beyotime) and boiled for 5 min. After loading the prepared samples and protein marker into the wells of a 12% separating gel, the bands were resolved by PAGE at 80 kV for 15 min and then at 120 kV for another 15 min, the gel was stained with Coomassie blue dye (Beyotime). Three gel slices from each gel were cut into 1 mm3 cubes, transferred to a 1.5 mL microcentrifuge tube, and washed with 500 μL of 50 mM ammonium bicarbonate/acetonitrile (ACN) (1:1, v/v) solution until Coomassie blue disappeared. After discarding the supernatant, 500 μL of ACN was added and the mixture was incubated for 10 min until the gel pieces became opaque and stuck together. After removing the ACN, the gel slices were rehydrated in 10 mM dithiothreitol (DTT)/50 mM ammonium bicarbonate, incubated at 56°C for 1 h, and the supernatant was discarded. For the rinsing step, 500 μL of ACN was added, the mixture was incubated for another 10 min, and ACN was removed. Next, the gel slices were incubated in 50 mM iodoacetamide (IAA)/50 mM ammonium bicarbonate at RT in the dark for 1 h, and the IAA/ammonium bicarbonate was discarded. After repeating the rinsing step, the gel pieces were incubated in proteomics grade trypsin (Promega) digestion solution on ice for 45 min. Another 5-20 μL of enzyme digestion solution was added, followed by overnight digestion at 37 °C. Finally, after adding 100 μL of extraction solution (5% TFA-50% ACN-45% ddH2O) to each sample, the mixture was incubated in a 37°C water bath for 1 h and sonicated for another 5 min. The extract was transferred to a fresh microcentrifuge tube and extraction was repeated.

Proteomics analysis with LC-MS/MS. All reagents used for LC-MS/MS experiments were chromatography grade and bought from Thermo Fisher Scientific. The extracted peptides were lyophilized and resuspended in 10 μL of 0.1% formic acid for separation using an Orbitrap Eclipse Mass Spectrometer (Thermo Fisher Scientific), equipped with a 150 μm×15 cm in-house made column packed with Acclaim PepMap RPLC C18 (1.9 μm, 100 Å, Dr. Maisch GmbH). The organic gradient was driven by the Nanoflow UPLC system over 120 min using Buffer A (0.1% formic acid in water) and Buffer B (20% 0.1% formic acid in water - 80% acetonitrile) at a flow rate of 600 nL/min. The gradient was held from 4% to 8 % B for 3 min, from 8 % to 28% B for 86 min, from 28 % to 40% B for 20 min, from 40% to 95% B for 1 min and from 95% to 95% B for 10 min. Eluted peptides were directly sprayed into the mass

spectrometer. Ten MS/MS data-dependent scans were acquired simultaneously with one high-resolution (60000 at 400 m/z) full-scan mass spectrum to provide the amino acid sequence and mass-to-charge ratio for the selected peptide ions.

LC−MS/MS spectral data analysis. Raw MS files were analyzed and searched against the Uniprot-Mus musculus (Mouse) protein database based on the species of samples using MaxQuant (1.6.2.10) with the following parameters. Protein modifications were carbamidomethylation (C) (fixed), oxidation (M) (variable). Enzyme specificity was set as trypsin. Maximum missed cleavages were set as 2. Precursor ion mass tolerance was set as 20 ppm. MS/MS tolerance was set as 20 ppm. Only high confident identified peptides were chosen for protein identification analysis.

Protein concentration. 25 μL of purified desorbed proteins or different concentrations of serially diluted bovine serum albumin (BSA, Pierce) were transferred into a 96-well plate. After adding 200 μL of freshly prepared BCA Protein Assay working reagent (Pierce) to each well, the samples were incubated at 60°C for 30 min. Absorbance at 562 nm was measured by a Multiskan GO UV-absorbance microplate reader (Thermo Fisher Scientific). Protein concentrations were calculated by using BSA as a standard of calibration.

***In vivo* organ-level distribution by ICP-MS.** Mice received an i.v. injection of SPIONs at a concentration of 10 mg Fe/kg mouse via the tail vein. At different time points, mice were sacrificed and perfused with PBS for 5–10 min each to remove the endogenous iron as much as possible. The heart along with aorta and other major internal organs were excised, minced, and digested in 0.5 mL of 65% trace-metal grade HNO_3 over 2–3 d. The lysate was diluted to 2% HNO_3 solution with Nanopure water and passed through a 0.2 μm hydrophilic syringe filter, and its Fe content was measured by ICP-MS. Tissues from uninjected mice were used to account for the background Fe content.

Preparation of aorta samples for *in vivo* efficacy by qRT-PCR. Mice were sacrificed 24 h after the last injection of SPIONs, when their intact aortas were harvested. The freshly harvested tissue was snap frozen in liquid nitrogen. Frozen tissue was ground with mortar and pestle and RNA was isolated using Trizol.

***En face* Oil Red O staining of intact aorta and aortic root sections.** Following different treatments, $ApoE^{-/-}$ mice were euthanized and perfused with PBS for 5-10 min. Heart with whole aorta was collected and dissected. Aortic arch and thoracic aorta were longitudinally opened and fixed in 10% formalin for 30 min. Whole aortas were rinsed with 70% isopropanol (Sigma-Aldrich), stained with freshly prepared 0.3% Oil Red O solution (Sigma-Aldrich) for 15 min. 6–8 cryosection slices were washed with Nanopure water for three times to remove the OCT, stained with ORO similarly to the aorta for 15 min, and mounted with aqueous mounting medium (glycerol jelly; Sigma-Aldrich) for visualization under a Nikon Ni-U microscope. The intact aortas were photographed using a CCD camera that was connected to a dissection microscope (Zeiss, Stemi 305). The aortic root sections were visualized under a Ti-E motorized inverted fluorescence microscope (Nikon) in bright-field mode. The red area covered by plaque and the total artery area were quantified using the NIH ImageJ software.

Sirius Red staining of aortic root sections. 6–8 cryosection slices were washed with Nanopure water for three times to remove the OCT and the slices were immersed in picro Sirius Red solution and stained for 60 min at RT. All the slices were rinsed quickly in 2 changes of acetic acid solution, washed in distilled water, dehydrated in ethanol, cleared in xylene, and mounted with DPX mountant. Sections were photographed using a Ti-E motorized inverted fluorescence microscope (Nikon) with the polarized-light mode. Data were further analyzed by Image J.

Efficacy evaluation by confocal immunofluorescence. The contents of macrophages (CD68) within the aortic root lesions and adhesion molecules (ICAM-1) on ECs were quantified by IF (see process above in the ex vivo tissue-level distribution part). Data were further analyzed by Image J.

Efficacy evaluation by immunohistochemistry (IHC). The content of vascular smooth muscle cells (SMCs) was quantified by IHC. 6–8 frozen slices from each mouse were washed with PBS three times to remove the OCT. After fixation with 4% PFA in PBS for 30 min, the sections were blocked with 2.5% horse serum (Vector Laboratories) at RT for 2 h and stained

with 2.5% horse serum containing anti-α-SMA rabbit antibody (65 ng/mL, ab150301, Abcam) at 4 ºC overnight. After rinses with PBS, the sections were treated with 3% H2O2 (Merck Millipore) for 10 min, rinsed again, and incubated with ~50 µL of secondary antibodies (MP-7401-50; ImmPRESS HRP Polymer detection Kit; Vector Laboratories) for 30 min. The sections were developed by using 3,3'-diaminobenzidine (DAB) enzyme substrate (ImmPACTTM DAB, Vector Laboratories) for 4 min. All slides were counter-stained with Mayer's hematoxylin for 2 min, washed in distilled water, dehydrated in ethanol, cleared in xylene, and mounted with DPX mountant. Sections were photographed using a Ti-E motorized inverted fluorescence microscope (Nikon) with the bright-field mode. Data were further analyzed by Image J.

Whole-transcriptome analysis with total RNA sequencing (RNA-Seq). 24 h after the last injection in our efficacy studies, the aorta was harvested from each HCD fed mouse from four treatment groups (N=3 per group), including (i) untreated control, (ii) PEG-SPIONs, (iii) miR-146a-SPIONs, and (iv) miR-nc-SPIONs. The harvested aorta was snap frozen in liquid nitrogen, stored at -80 ºC, and sent to the Beijing Genomics Institute (BGI) for RNA extraction, RNA library construction, and bioinformatic analysis. The mRNA was isolated from total RNA using oligo (dT) magnetic beads following the manufacturer's instructions for cDNA library construction. Double stranded cDNA was sequenced using the DNBseq platform. At least 20 million clean reads per sample on the DNBseq platform were generated for data analysis. Differential expressed transcript (DET) detection, gene ontology analysis of DET, and other analysis were performed using the Dr. Tom analysis platform (BGI). GO terms and DETs with corrected p values (Q values) < 0.05 were considered significantly enriched.

Blood test and histological staining for *in vivo* toxicity. About 0.5 mL of whole blood was collected from the mouse heart via an intracardiac puncture (using a 25-Gauge needle) under anaesthesia before sacrifice. The whole blood was left to sit at RT for 30 min and then centrifuged at 2,000 ×g at 4°C for 10 min. About 200 µL of blood serum was collected from the supernatant and sent to the PathLab Medical Laboratories (Hong Kong) on the same day for blood biochemistry analysis. The lower heart, liver, spleen, and kidney were fixed in 4% PFA overnight, embedded in paraffin, and cut into sections of 5 µm thick. Paraffin-sections were deparaffinized in xylene (5 min × 3 times), rehydrated through a series of ethanol (100%, 90%, 70%; 3 min × 2 times at each ethanol concentration) as well as deionized water (MilliQ) (5 min × 5 times), and counterstained by hematoxylin and eosin (H&E; Sigma) for 2 min and 1 min, respectively. The stained sections were dehydrated in ethanol, cleared in xylene, and mounted with DPX mountant (Sigma) for visualization under a Ti-E motorized inverted fluorescence microscope (Nikon) in bright-field mode.

Data processing and statistical analysis. The Prism (GraphPad Software) and Excel software were used for data analysis and graph construction. To determine the statistical significance in the comparison of two groups, an unpaired two-tail t test was performed. To determine the statistical significance in the comparison of multiple groups, an unpaired one-way analysis of variance (ANOVA) was performed with Tukey's Test for post hoc analysis. Normality of sampling distribution of means was validated by Shapiro-Wilk test. Homogeneity of variance was validated by Bartlett's test. Results are considered significant at $P < 0.05$.

Table S1. Delivery of NPs to the atherosclerotic plaques *via* i.v. injection in the literature.

This table contains information from past publications that disclosed the values of NP delivery efficiency to atherosclerotic plaques in terms of %ID or %ID/g. Imaging studies that disclosed the delivery values in terms of fluorescence, photon, or radiance are not included because such values cannot be directly compared with the performance of our miR146a-SPION.

Abbreviations:

NPs: Nanoparticles

HD: Hydrodynamic diameter

HDL: High-density lipoprotein

MUDA: mercaptoundecanoic acid

Year	Type	HD	Organ	Time point	Delivery Efficiency (% ID or % ID/g)	Animal model
This work	miR-146a-coated iron oxide NPs	72.7 nm	Aorta and heart	2 h	1.2% ID	$ApoE^{-/-}$ mice
					8.9% ID/g	
				24 h	0.5% ID	
					4.1% ID/g	
	PEG-coated iron oxide NPs	59.3 nm	Aorta and heart	2 h	0.4% ID	
					3.5% ID/g	
				24 h	0.4% ID	
					3.0% ID/g	
2006 (*2*)	VCAM-1 peptide-targeting iron oxide NPs	38 nm	Heart	6 h	0.90±0.18% ID/g	$ApoE^{-/-}$ mice
2012 (*3*)	Anti-Mrp14 antibody lipid NPs	83 nm	Aorta	36 h	6% ID/g dry weight	$ApoE^{-/-}$ mice
2013 (*4*)	Dextran-coated iron oxide NPs	28 nm	Heart	6 h	4.27±1.15% ID/g	$ApoE^{-/-}$ mice
				24 h	1.73±0.1% ID/g	
				48 h	1.41±0.05% ID/g	
				72 h	1.15±0.03% ID/g	
2013 (*5*)	^{89}Zr-dextran NPs	13.3 nm	Aorta	48 h	1.2±0.1% ID/g	$ApoE^{-/-}$ mice
			Heart		1.2±0.2% ID/g	
2014 (*6*)	Anti-Lox-1 antibody iron oxide NPs	28.2 nm	Aorta	24 h	3.5% ID/g	$ApoE^{-/-}$ mice
			Heart		0.5% ID/g	
2015 (*7*)	Simvastatin-loaded HDL NPs	N/A	Aorta	24 h	1.0% ID/g	$ApoE^{-/-}$ mice

2016 (*8*)	Viral macrophage inflammatory protein-II-polymer NPs	15.8 nm	Aortic arch	24 h	Early atherosclerosis (20 weeks) 6.12±0.88% ID/g	ApoE$^{-/-}$ mice
					Late atherosclerosis (37 weeks) 8.88±1.75% ID/g	
2016 (*9*)	HDL NPs	30 nm	Aortic root and arch	24 h	0.07% ID	ApoE$^{-/-}$ mice
		40 nm			0.05% ID	
		70 nm			0.04% ID	
		70 nm			0.03% ID	
2016 (*10*)	11-MUDA -AuNPs	31.5 nm	Heart	5 d	5% ID/g	ApoE$^{-/-}$ mice
2017 (*11*)	Hyaluronan NPs	32 nm	Aorta	24 h	6 week-HFD ~0.018% ID	ApoE$^{-/-}$ mice
					12 week-HFD ~0.017% ID	
2019 (*12*)	SR-BI and CD36 targeting biomimetic NPs	122.1 nm	Aortic tree	4 h	1-dose: ~0.18% ID	ApoE$^{-/-}$ mice
					4-week treatment (twice a week): ~0.58% ID	
2020 (*13*)	CD44-targeting hyaluronan-based NPs	122 nm	Aorta	24 h	1.7% ID/g	ApoE$^{-/-}$ mice

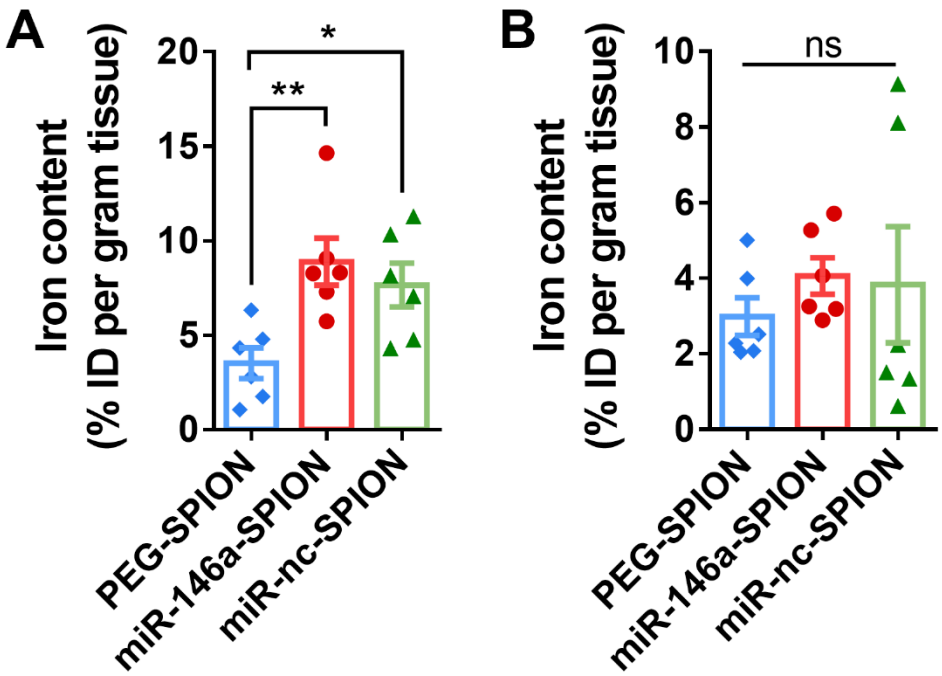

Fig. S1. ICP-MS measurements of the iron content in the aorta and heart (sites of plaques for ApoE$^{-/-}$ mice) in terms of %ID per gram tissue. (**A**) 2 h post-injection and (**B**) 24 h post-injection. The typical total weight of the aorta and heart of plaque-bearing ApoE$^{-/-}$ mice is 120 mg. The same data plotted in terms of %ID tissue are found in Fig. 2A (2 h post-injection) and Fig. S22 (24 h post-injection). Data are presented as means ± SEM. Statistical significance was calculated by one-way ANOVA with Tukey's Test for post-hoc analysis. *P < 0.05, **P < 0.01, ns: not significant (P > 0.05). n = 6; across 2 experiments.

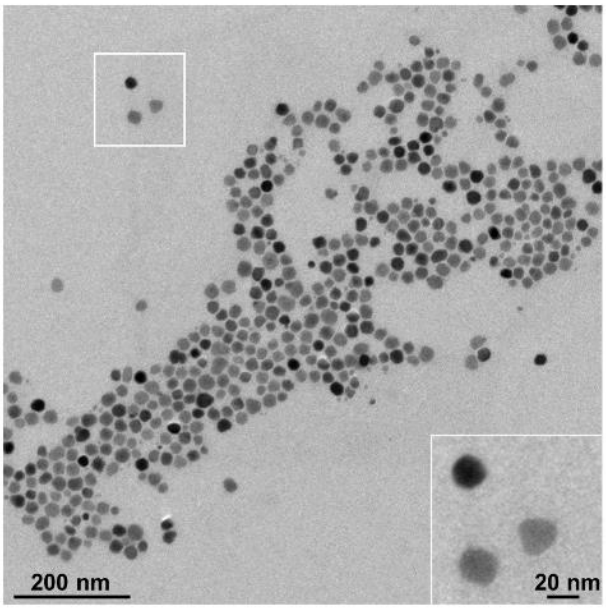

Fig. S2. Representative TEM images of PEG-SPIONs show a core diameter of ~20 nm.

Table S2. List of oligonucleotide sequences and their associated applications

Name	Sequence	Associated applications	Molecular weight (Da)
miR-146a	5'-/5AmMC6/rU*rG*rA* rG*rA*rA* rC*rU*rG* rA*rA*rU* rU*rC*rC* rA*rU*rG* rG*rG*rU* rU-3'	Cytotoxicity test; ICP-MS*;* qRT-PCR; *In vivo* efficacy studies	7559.7
Cy5-miR-146a	5'-/5AmMC6/rU*rG*rA* rG*rA*rA* rC*rU*rG* rA*rA*rU* rU*rC*rC* rA*rU*rG* rG*rG*rU* rU/3Cy5Sp/-3'	Confocal microscopy; *Ex vivo* fluorescence imaging; *In vivo* flow cytometry; quantitation of loading density of miRNA	8230.4
miR-nc	5'-/5AmMC6/rU*rU*rU* rG*rU*rA* rC*rU*rA* rC*rA*rC* rA*rA*rA* rA*rG*rU* rA*rC*rU* rG-3'	Cytotoxicity test; ICP-MS*; In vitro* cellular uptake; qRT-PCR; *In vivo* efficacy studies	7487.7
Cy5-miR-nc	5'-/5AmMC6/rU*rU*rU* rG*rU*rA* rC*rU*rA* rC*rA*rC* rA*rA*rA* rA*rG*rU* rA*rC*rU* rG/3Cy5Sp/-3'	Confocal microscopy; *In vivo* flow cytometry; quantitation of loading density of miRNA	8158.3
abasic	5'/5AmMC6/T*T*T* T*T*T* T*T*T* T*/idSp/*/idSp/* /idSp/*/idSp/*/idSp/* /idSp/*/idSp/*/idSp/* /idSp/*/idSp/*/idSp/* /3dSp/-3'	ICP-MS	5657.6
Cy5-abasic	5'/5AmMC6/T*T*T* T*T*T* T*T*T* T*/idSp/*/idSp/* /idSp/*/idSp/*/idSp/* /idSp/*/idSp/*/idSp/* /idSp/*/idSp/*/idSp/* /idSp//3Cy5Sp/-3'	*In vivo* flow cytometry; quantitation of loading density of DNA	6328.3

NOTE: In each abasic oligonucleotide, more than half of the bases (12 out of 22) contains neither a nucleobase; rather, the abasic sites only contain the negatively charged phosphate and ribose. It is challenging to synthesize a purely abasic oligonucleotide because the absence of ultraviolet light-absorbing nucleobases renders subsequent purification by liquid chromatography infeasible.
/5AmMC6/: 5' Amino Modifier C6
/3Cy5Sp/: 3' Cy5™-Sp
/idSp/: Int dSpacer
/3dSp/: 3' dSpacer
*: phosphorothioate

Table S3. Physicochemical characterization of different SPION types (in both Cy5-labeled and nonfluorescent forms) by dynamic light scattering (DLS)

Sample	In H_2O		In DMEM+10% FBS after 24 h at 37 °C		ζ-Potential In 1 mM KCl (mV)
	HD (nm)	PDI	HD (nm)	PDI	
PEG-SPION	59.3 ± 0.7	0.200	72.1 ± 3.1	0.183	-8.2 ± 0.8
miR-146a-SPION	72.7 ± 2.5	0.182	85.4 ± 3.6	0.237	-21.8 ± 1.8
miR-nc-SPION	76.6 ± 0.9	0.217	85.2 ± 7.0	0.246	-16.1 ± 2.7
Abasic -SPION	70.7 ± 4.9	0.126	75.8 ± 1.9	0.192	-18.8 ± 3.7
Cy5-labeled PEG-SPION	66.6 ± 3.4	0.137	79.2 ± 2.4	0.290	-8.8 ± 1.4
Cy5-labeled miR-146a-SPION	79.3 ± 1.2	0.175	86.4 ± 3.4	0.207	-14.0 ± 0.9
Cy5-labeled miR-nc-SPION	82.3 ± 0.9	0.226	87.6 ± 3.5	0.237	-13.1 ± 1.2
Cy5-labeled Abasic-SPION	73.7 ± 2.9	0.219	80.2 ± 3.3	0.276	-14.9 ± 3.9

HD refers to hydrodynamic diameter (HD) of in water at RT or upon incubation in Dulbecco's Modified Eagle Medium (DMEM) containing 10% fetal bovine serum (FBS) at 37°C for 24 h. PDI refers to the polydispersity index. Of all NP types tested, the size distribution is homogeneous, as evidenced by their small polydispersity indices (<0.25). Upon incubation in DMEM containing 10% FBS, the hydrodynamic size of the SPIONs increases by 5–13 nm, suggesting serum adsorption without evident aggregation. The increased hydrodynamic size (from ~59 nm to ~75 nm) and more negative surface charge (from -8 mV to -20 mV) indicate attachment of oligonucleotides to the surface of PEG-SPIONs to form miRNA-conjugated SPIONs. There are 275 dyes on Cy5-labeled miR-146a-SPIONs, 263 dyes on Cy5-labeled miR-nc-SPIONs, and 217 dyes on Cy5-labeled PEG-SPIONs. There are 352 dyes on Cy5-labeled abasic-SPIONs, a higher loading than that of miR-146a-SPIONs possibly because the lower molecular weight of abasic oligonucleotides (Table S2) facilities denser loading of oligonucleotides to the SPION core. Cy5 conjugation only led to a ~10 nm increase in hydrodynamic size for all SPION types tested.

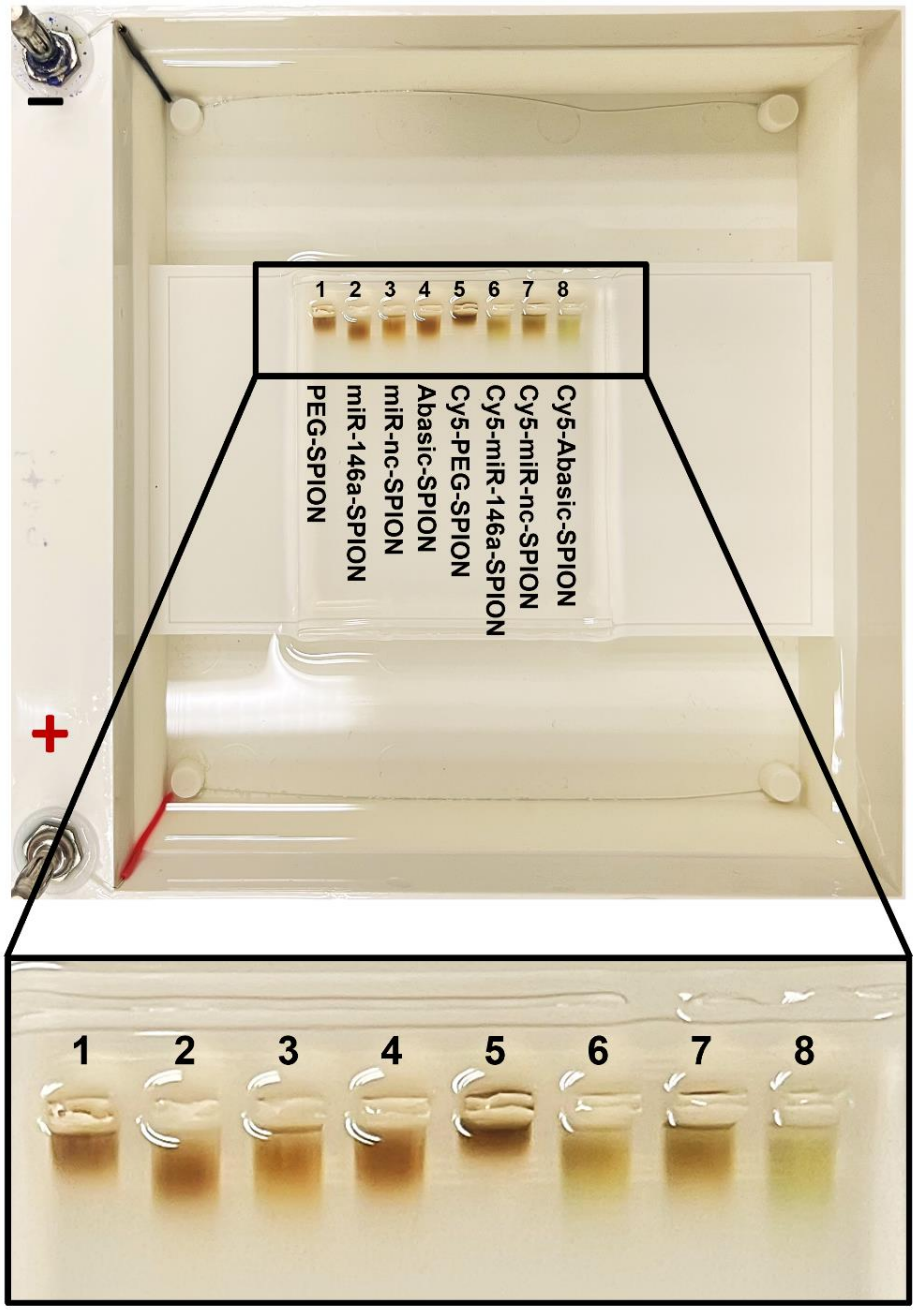

Fig. S3. Agarose gel electrophoresis of different SPION types. Faster migration of miR-146a-SPIONs, miR-nc-SPIONs, and abasic-SPIONs in both nonfluorescent and Cy5-labeled forms, toward the positive electrode indicates their more negative surface charge than PEG-SPIONs. These data agree with the zeta potential data in Table S3 and suggest oligonucleotide attachment on the miR-SPIONs. Top: original gel. Bottom: Enlargement of the boxed region in the top panel.

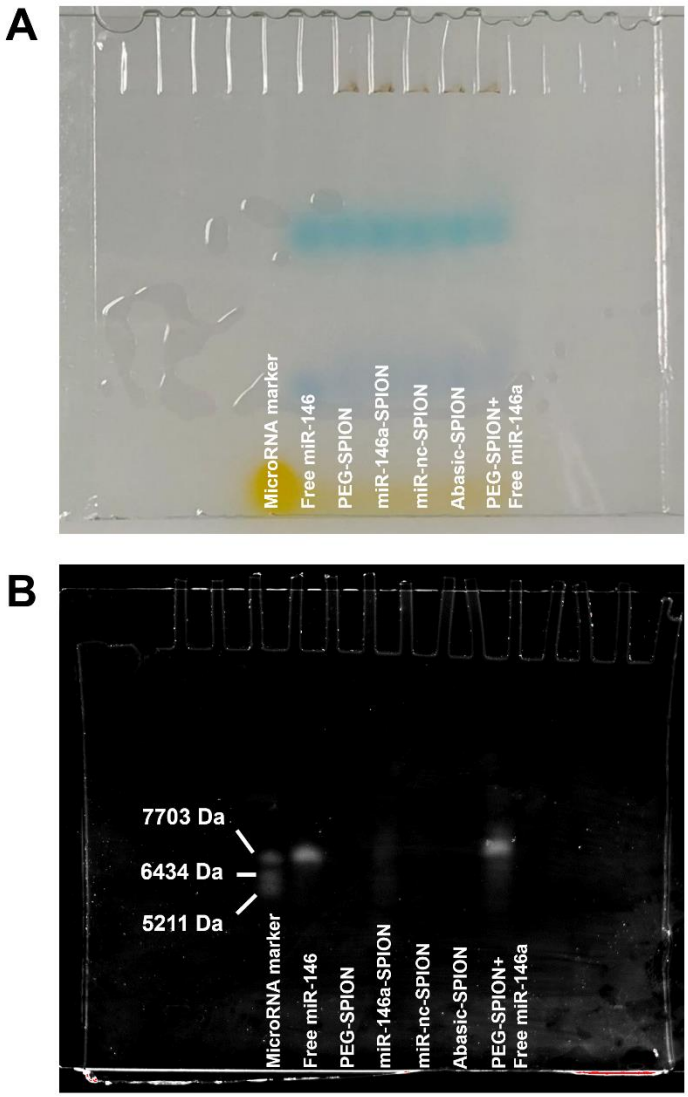

Fig. S4. Denaturing polyacrylamide gel electrophoresis (PAGE) of different SPION types. From left to right, the samples are a commercial microRNA marker, free miR-146a, PEG-SPIONs, miR-nc-SPIONs, miR-146a-SPIONs, and abasic-SPIONs, and a physical mixture of PEG-SPIONs and free miR-146a. **(A)** After electrophoresis, optical imaging reveals brown color only in the loading wells of all SPION types but not free miR-146a or the RNA ladder. This result indicates that SPIONs remain in the loading wells without traversing down the PAGE gel. (**B)** The PAGE gel from the gel cassette and immersed it in a SYBR Gold Gel Staining solution to reveal any nucleic acid bands in the gel. Fluorescence imaging reveals bands only in the lanes of miRNA ladder, free miR-146a, and the physical mixture of PEG-SPIONs and free miR-146a; these bands are absent for PEG-SPIONs, miR-SPIONs, or abasic-SPIONs. (Removal of the gel from the cassette inevitably led to the loss of all types of SPIONs originally in the loading wells.) Because only free oligonucleotides (not SPION-attached oligonucleotides) are small enough to move down the gel, we conclude that the oligonucleotides are conjugated to the SPION for miR-146a-SPIONs, miR-nc-SPIONs, and abasic-SPIONs.) The molecular weight of miR-146a (phosphorothioate backbone) is 7559.9 Da, closer to that of the 25-base miRNA (phosphodiester; 5´AGAGCAGUGGCUGGUUGAGAUUUAA 3'; MW: 7702.9 Da) than that of the 21-base miRNA (phosphodiester; 5´AGCAGUGGCUGGUUGAGAUUU 3´; MW: 6434.1 Da) as part of the miRNA marker. The 17-base miRNA in the miRNA marker is 5´CAGUGGCUGGUUGAGAU 3'; MW: 5211.3 Da).

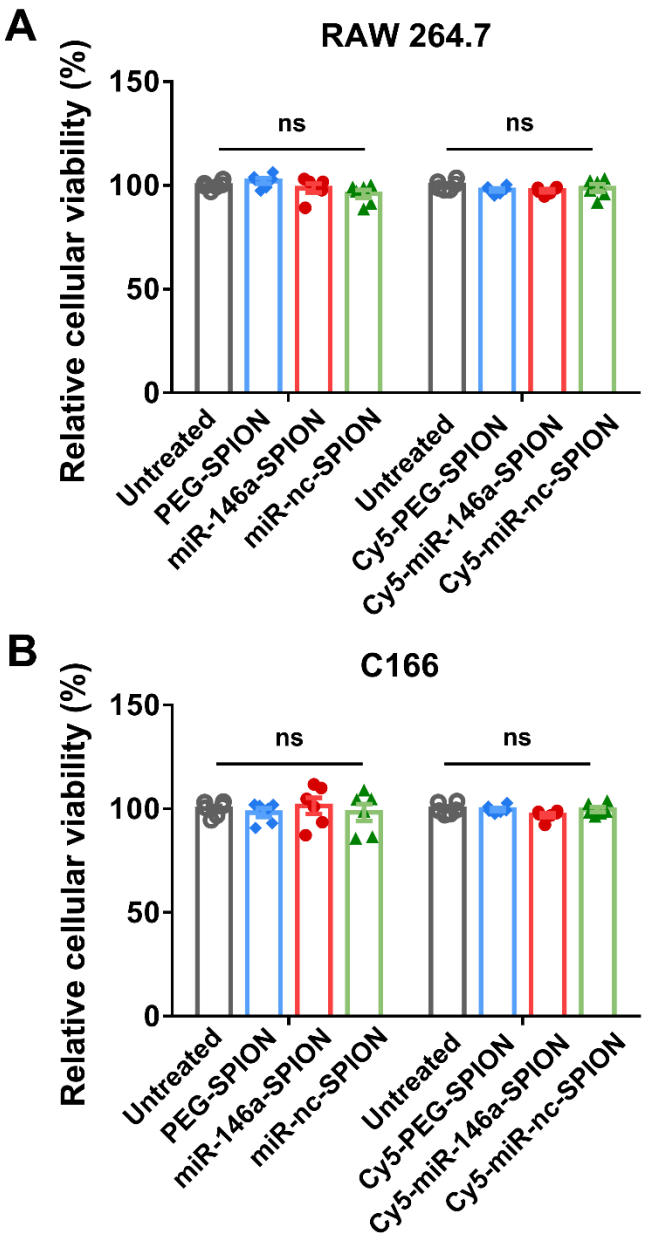

Fig. S5. Cytotoxicity of PEG-SPIONs and miR-SPIONs. (**A**) RAW 264.7 macrophages and (**B**) C166 endothelial cells were incubated with 5 nM PEG-SPIONs (blue), miR-146a-SPIONs (red), and miR-nc-SPIONs (green) in DMEM with 10% FBS for 24 h. By the alamarBlue assay, the treated cells remain largely viable after incubation with all types of NPs tested. Data are presented as mean ± SEM. Statistical significance was calculated by one-way ANOVA with Tukey's Test for post-hoc analysis. ns: not significant ($P > 0.05$). n = 6 per group, across 1 experiment.

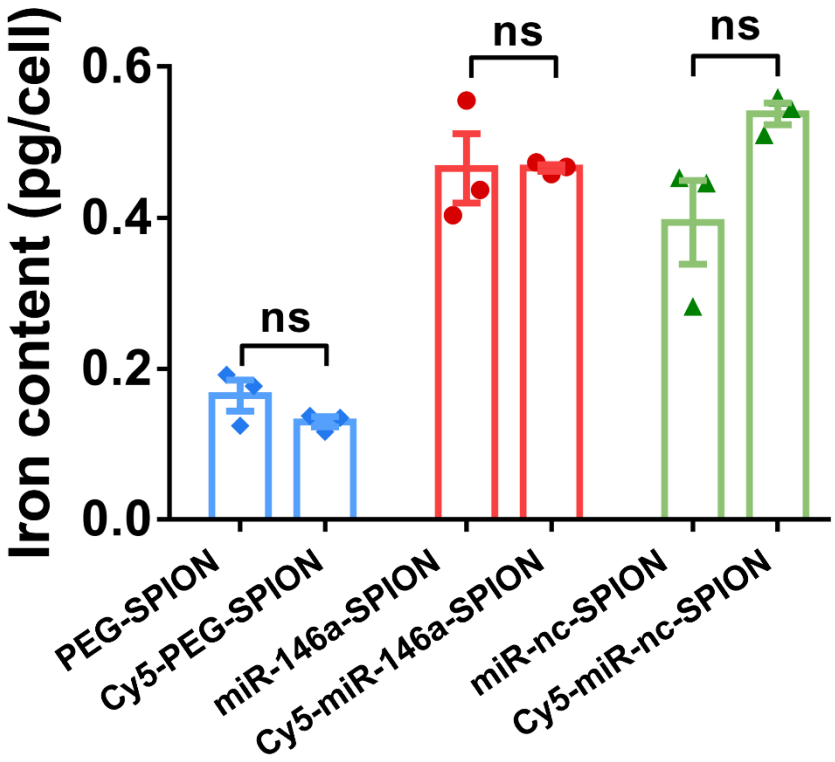

Fig. S6. Cellular uptake of different SPION types by ICP-MS measurements. Fluorescence labeling by Cy5 dye molecules did not affect the uptake of PEG-SPIONs (blue), miR-146a-SPIONs (red), or miR-146a-SPIONs (green) by RAW 264.7 cells after 2 h of incubation. Data are presented as mean ± SEM. Statistical significance was calculated by Student's t test, ns: not significant ($P > 0.05$). n=3 per group, across 1 experiment.

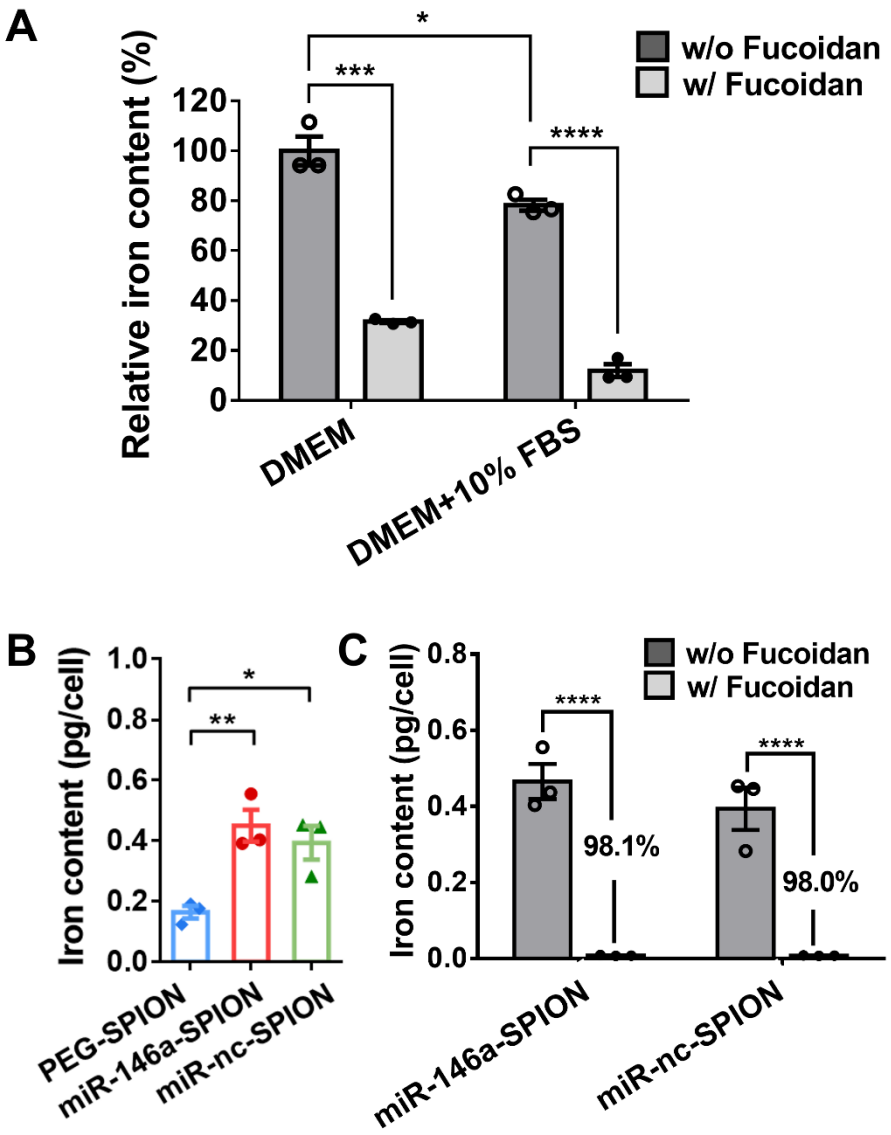

Fig. S7. Effect of serum adsorption on the cellular uptake of miR-146a-SPIONs via SR-A. (**A**) *In vitro* cellular uptake of miR-146a-SPIONs by RAW 264.7 macrophages after 2 h of incubation in DMEM with or without 10% fetal bovine serum (FBS) by ICP-MS-measurements. Pretreatment of fucoidan significantly reduced the uptake of miR-146a-SPIONs by RAW 264.7 cells in both serum-containing and serum-free medium. Data are presented as mean ± SEM. Statistical significance was calculated by Student's t-test. *P < 0.05, ***P < 0.001, ****P < 0.0001. n = 3 cell samples per group, across 1 experiment. (**B**) *In vitro* uptake of PEG-SPIONs (blue), miR-146a-SPIONs (red), and miR-nc-SPIONs (green) by RAW 264.7 macrophages by ICP-MS-measurements. Data are presented as mean ± SEM. Statistical significance was calculated by one-way ANOVA with Tukey's Test for post-hoc analysis. *P<0.05, **P<0.01. n = 3 cell samples per group, across 1 experiment. (**C**) Pretreatment of fucoidan significantly reduced the uptake of miR-146a-SPIONs and miR-nc-SPIONs by RAW 264.7 cells after 2 h of incubation. Data are presented as mean ± SEM. Statistical significance was calculated by Student's t-test. ****P < 0.0001. n = 3 cell samples per group, across 1 experiment. Collectively, these results indicate that the serum protein corona did not severely reduce the cellular uptake of miR-SPIONs and targeting of SR-A.

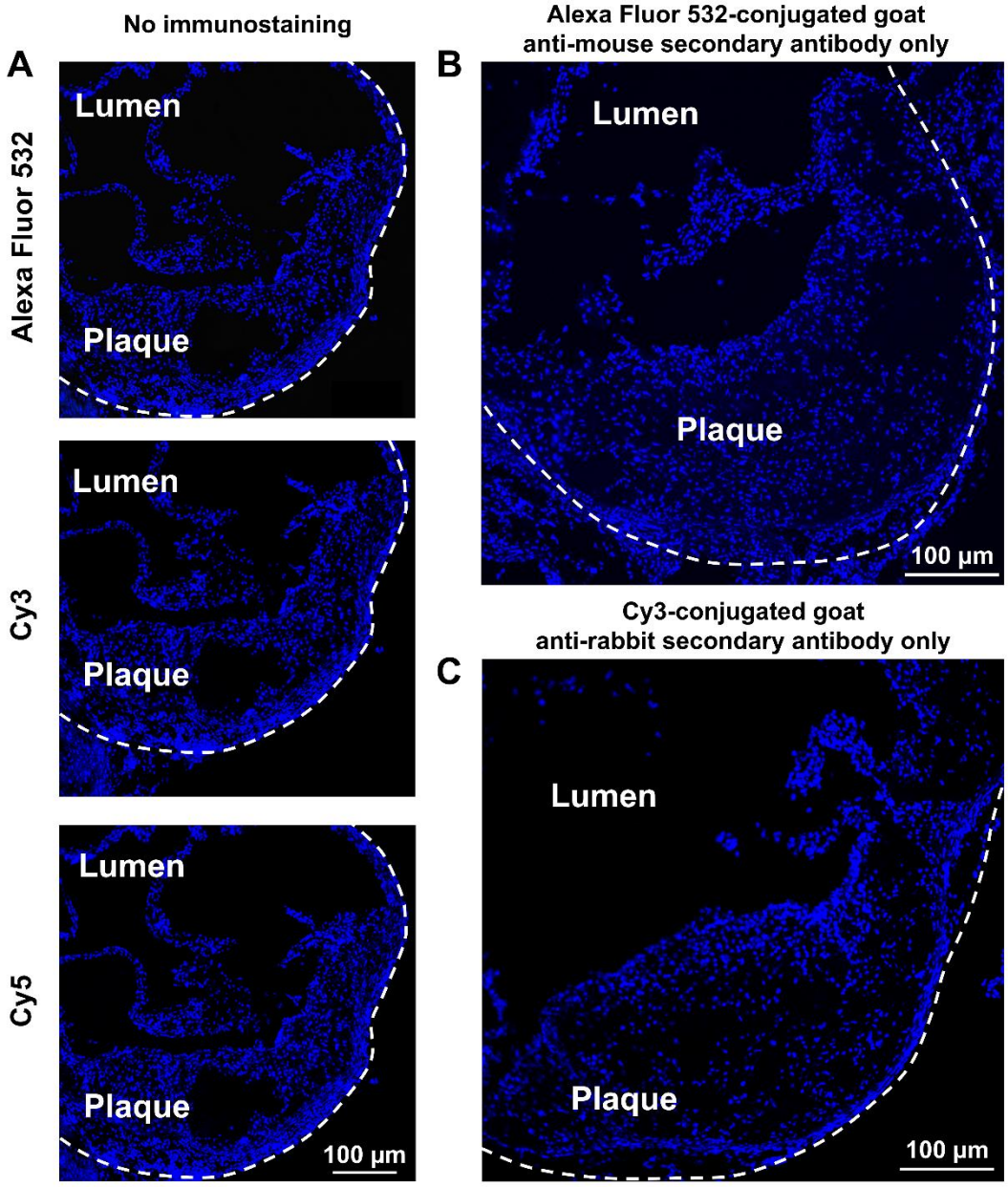

Fig. S8. Staining controls of the aortic root of uninjected plaque-bearing ApoE$^{-/-}$ mice fed with high-cholesterol diet (HCD) for 12 weeks. (A) Representative confocal immunofluorescence (IF) images of aortic root tissue sections do not emit detectable tissue autofluorescence in the Alexa Fluor 532, Cy3 (both dyes for labeling the secondary antibodies), or Cy5 wavelength (dye for labeling all SPION types tested). **(B–C)** Representative confocal IF images of aortic roots were stained with (**B**) Alexa Fluor 532-conjugated goat anti-mouse secondary antibody or (**C**) Cy3-conjugated goat anti-rabbit secondary antibody, but without primary antibodies against the marker of the plaque [e.g., ICAM-1 for endothelial cells (ECs) and CD68 for macrophages]. No Alexa Fluor 532 or Cy3 fluorescence was detected in these sections under imaging conditions that were identical to those shown in Fig. 1C, Fig. 2B, and Fig. 4A–B of the main text. These data support the specificity of the IF staining data in in Fig. 1C, Fig. 2B, and Fig. 4A–B and eliminate potential bias in interpretation of the confocal IF images. Blue: DAPI, cell nucleus. White dotted lines indicate the border of the vascular wall.

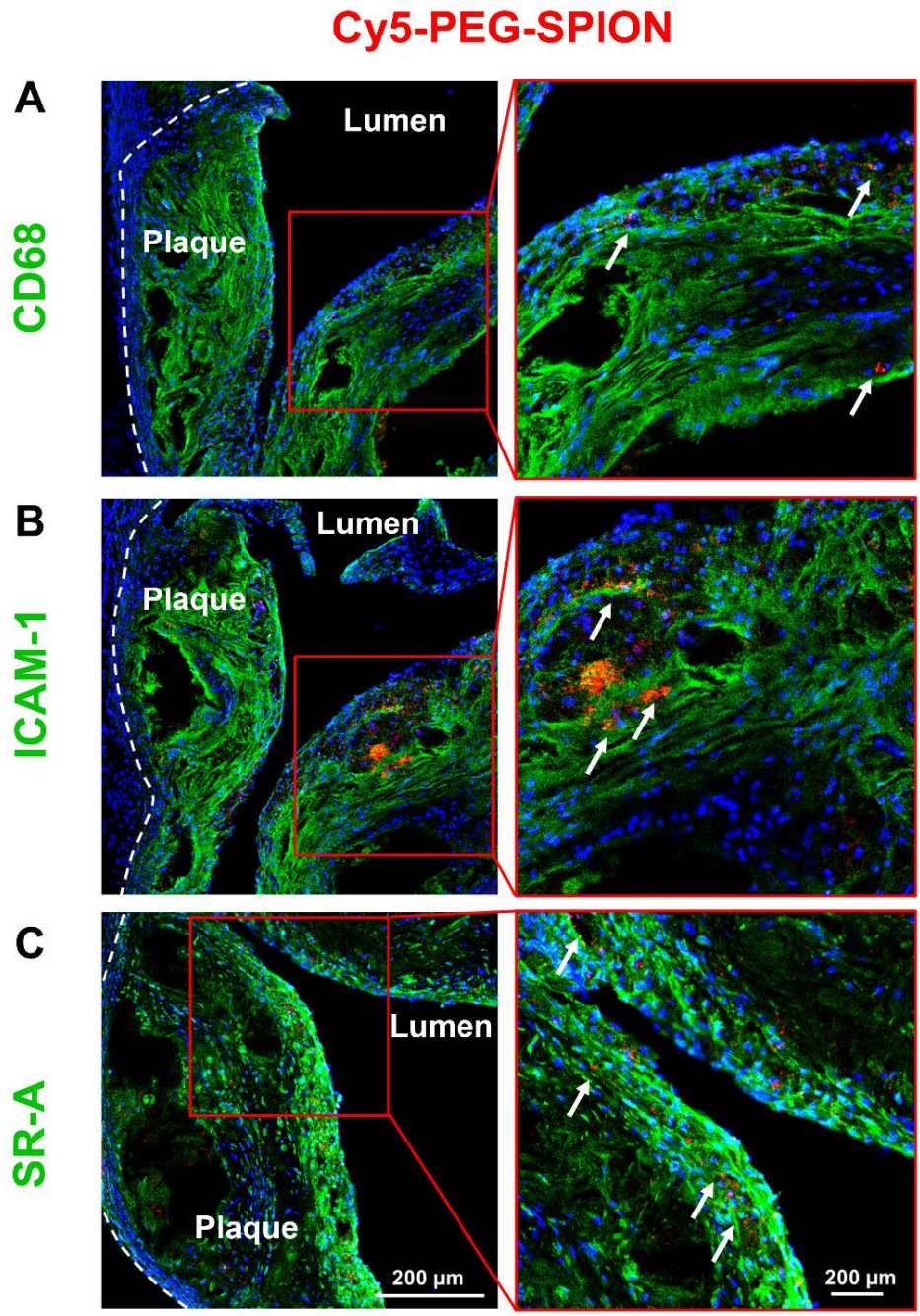

Fig. S9. *Ex vivo* binding of PEG-SPIONs to ECs and macrophages in the atherosclerotic plaque of ApoE$^{-/-}$ mice after 2 h of incubation. Representative confocal images show *ex vivo* association of Cy5-labeled PEG-SPIONs (red; with white arrows) to (**A**) macrophages, (**B**) ECs, and (**C**) SR-A in atherosclerotic plaques from the aortic root. Green pseudo color: CD68 (macrophages), ICAM-1 (ECs), or SR-A; Blue: DAPI. White dotted lines indicate the border of the vascular wall. The right panel shows the enlargement of the red boxed area in the left panel.

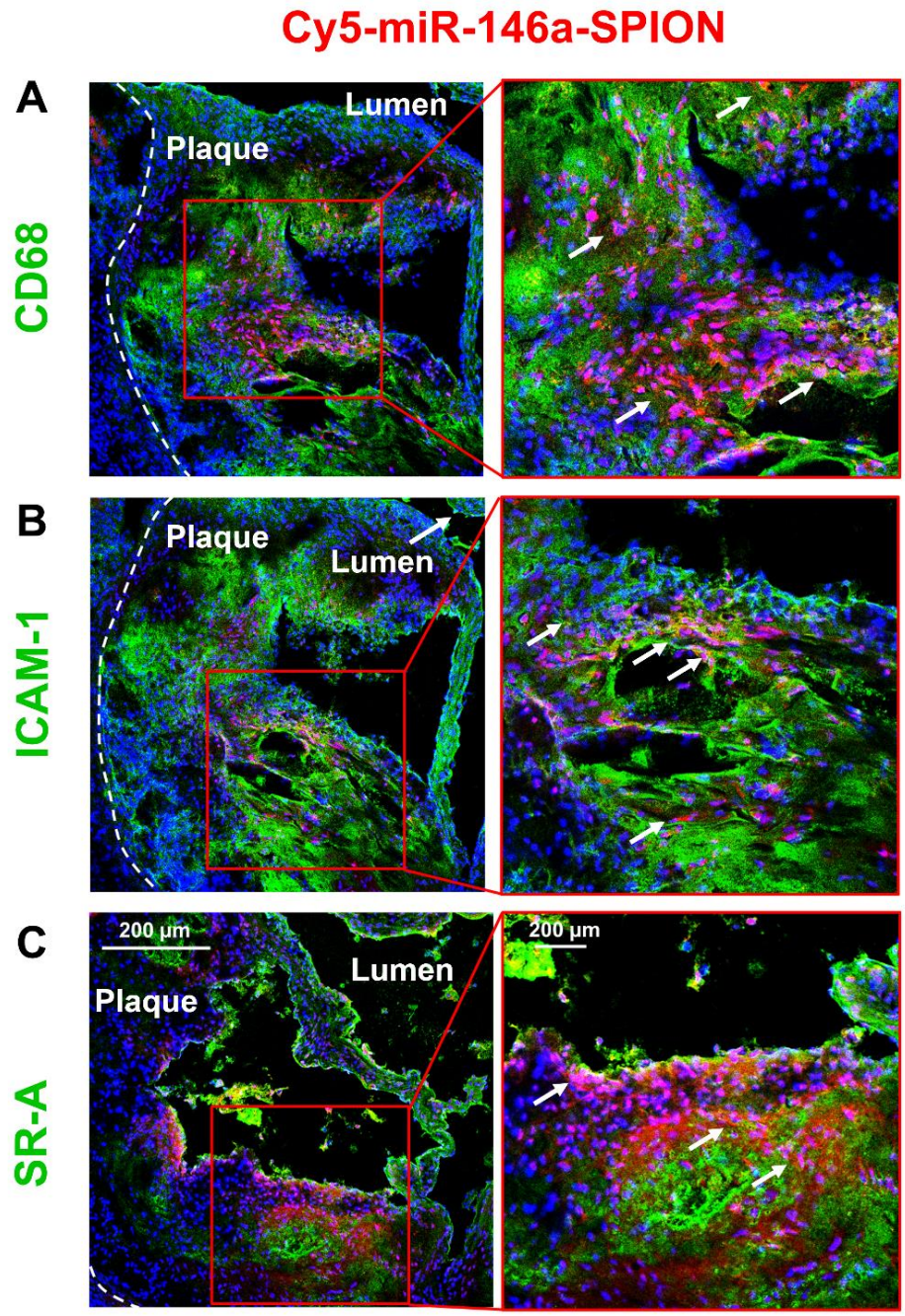

Fig. S10. *Ex vivo* binding of miR-146a-SPIONs to ECs and macrophages in the atherosclerotic plaque of ApoE$^{-/-}$ mice after 2 h of incubation. Representative confocal images show *ex vivo* association of Cy5-labeled miR-146a-SPIONs (red; with white arrows) to (**A**) macrophages, (**B**) ECs, and (**C**) SR-A in atherosclerotic plaques from the aortic root. Green pseudo color: CD68 (macrophages), ICAM-1 (ECs) or SR-A; Blue: DAPI. White dotted lines indicate the border of the vascular wall. The right panel shows the enlargement of the red boxed area in the left panel.

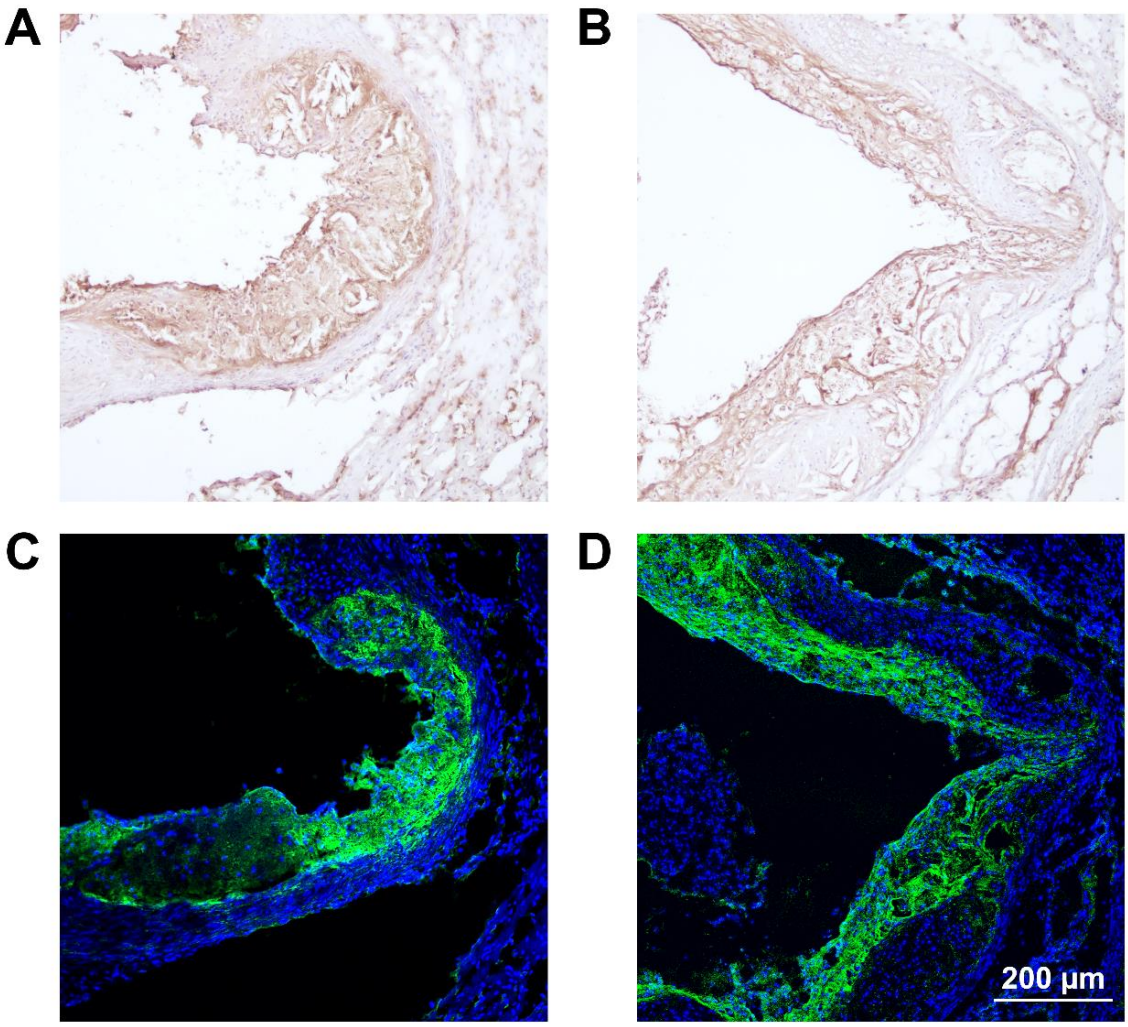

Fig. S11. Staining of ICAM-1-expressing regions of the atherosclerotic plaque of ApoE$^{-/-}$ mice that were fed with HCD for 12 weeks. Representative (**A**) (**B**) immunohistochemistry (IHC) images and (**C**) (**D**) confocal IF images of serial sections of the aortic roots from two different uninjected mice reveal consistent ICAM-1-positive signals (brown in IHC images; green pseudo color in confocal images). These data further bolster the validity of the IF signals in Fig. 1C and Fig. 4B of the main text and Fig. S9–10 in SI. These data also eliminate any potential bias due to tissue autofluorescence. Blue: DAPI.

Confocal IF staining controls from non-atherosclerotic untreated C57BL/6 mice
We confirmed that the aortic root tissue sections collected from non-atherosclerotic untreated C57BL/6 mice do not emit detectable autofluorescence in the Alexa Fluor 532 or Alexa Fluor 647 wavelengths (Fig. S12A). For these studies, we used Alexa Fluor 532-tagged secondary antibodies for labeling ICAM-1 (marker for inflamed ECs) and CD68 (marker for macrophages) and Alexa Fluor 647-tagged secondary antibodies for labeling CD144 (vascular endothelial (VE)-cadherin, a marker of endothelium). We also could not detect fluorescence when tissue sections from uninjected mice were stained with fluorescently labeled secondary antibodies only (without primary antibodies) as negative control (Fig. S12B).

Importantly, in aortic root sections collected from non-atherosclerotic untreated C57BL/6 mice, we detected no ICAM1 or CD68-positive regions by both primary and secondary antibodies because normal blood vessels should not express ICAM1 or contain CD68-expressing macrophages (Fig. S13A–B). To confirm that the ICAM1 and CD68 signals were undetectable, we performed an extra positive control experiment by staining the aortic root tissue sections with both primary and secondary antibodies against CD144 to verify the integrity of the endothelium. Confocal imaging revealed a thin layer of CD144-positive (red pseudo color) signals along the healthy endothelium and the autofluorescence of elastic lamina (green) on the plaque border (Fig. S13C). Collectively, these data empower us to eliminate bias of tissue autofluorescence or antibody specificity in our confocal IF data on plaque-bearing aortic roots.

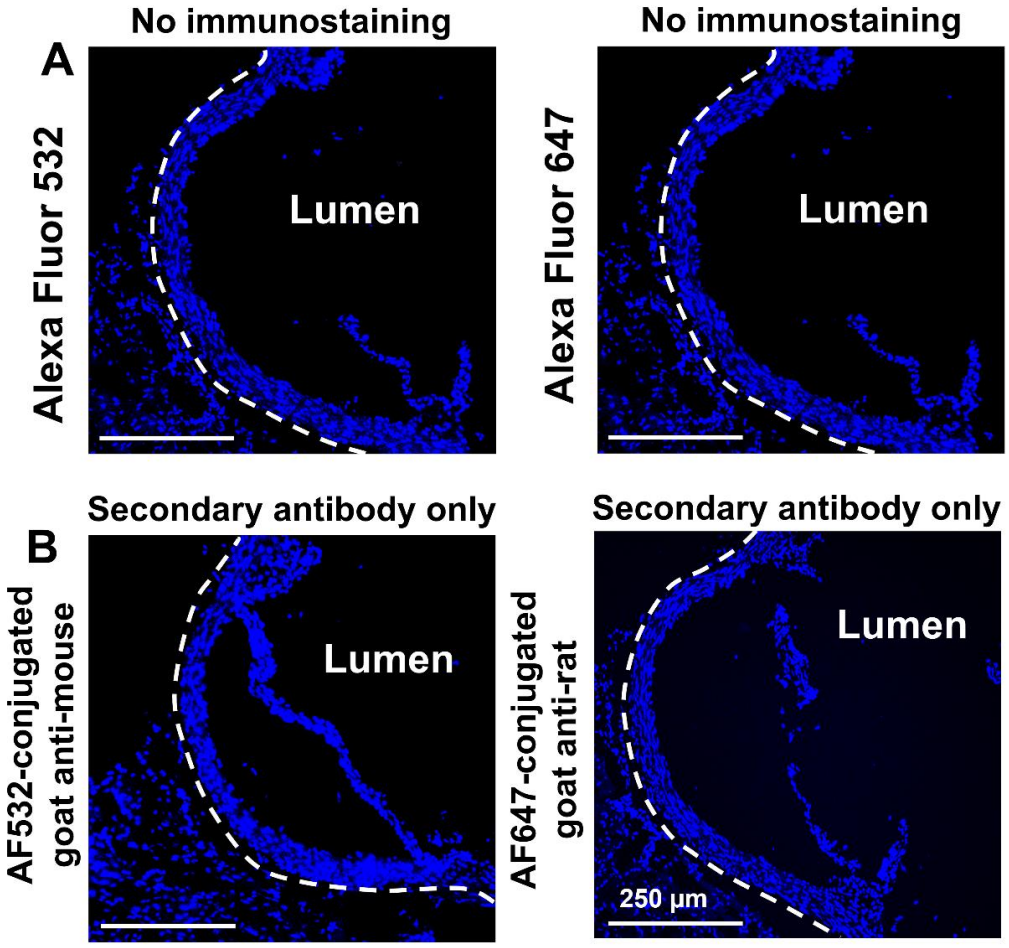

Fig. S12. Staining controls of the aortic root of healthy C57BL/6 mice without immunostaining or stained using secondary antibody only. (**A**) Representative confocal immunofluorescence (IF) images of aortic root tissue sections do not emit detectable tissue autofluorescence in the Alexa Fluor (AF) 532 or AF647 wavelengths. (**B**) Representative confocal IF images of aortic roots were stained with AF532-conjugated goat anti-mouse secondary antibody or AF647-conjugated goat anti-rat secondary antibody, but without primary antibodies against the marker of plaque (e.g., CD68 for macrophages and ICAM-1 for inflamed ECs) or the marker of endothelium (e.g., CD144 for VE–cadherin). Blue: DAPI.

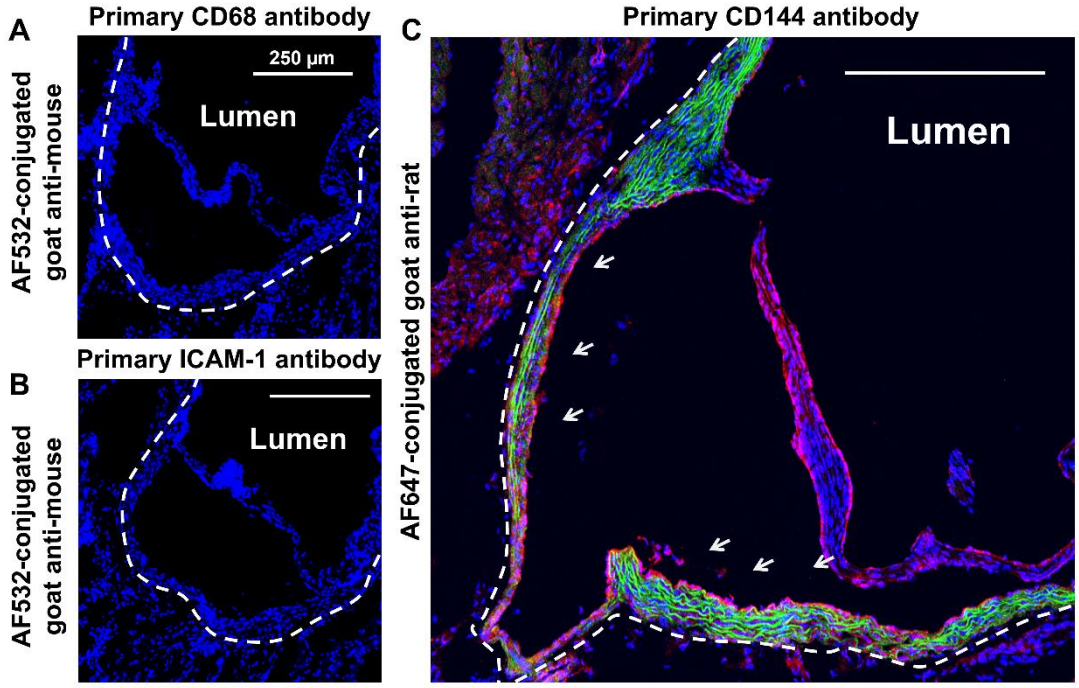

Fig. S13. Staining controls of the aortic root of healthy C57BL/6 mice. Representative confocal IF images of aortic roots were stained with primary antibodies against the marker of the plaque: (**A**) CD68 for macrophages, (**B**) ICAM-1 for inflamed ECs, or (**C**) CD144 for VE–cadherin. Their corresponding secondary antibodies are AF532-conjugated goat anti-mouse secondary antibody for CD68 and ICAM-1 as well as AF647-conjugated goat anti-rat secondary antibody for CD144. No AF532 fluorescence was detected in these normal aortic root sections under imaging conditions that were identical to those used for detecting CD68 and ICAM-1 in the plaque-bearing aortic root sections (Fig. 1C, Fig. 2B and Fig. 4A–B). As positive control, confocal imaging still revealed a thin layer of CD144-positive region along the healthy endothelium. Collectively, these data verify the intact endothelium structure in healthy mice and empower us to eliminate any bias of tissue autofluorescence or antibody specificity in our confocal IF data on plaque-bearing aortic roots. Blue: DAPI. Green: Autofluorescence of elastic lamina on the plaque border (excitation wavelength: 488 nm; emission wavelength: 500–520 nm). Red: CD144 VE–cadherin. White dotted lines indicate the border of the vascular wall. White arrows indicate the thin layer of endothelium.

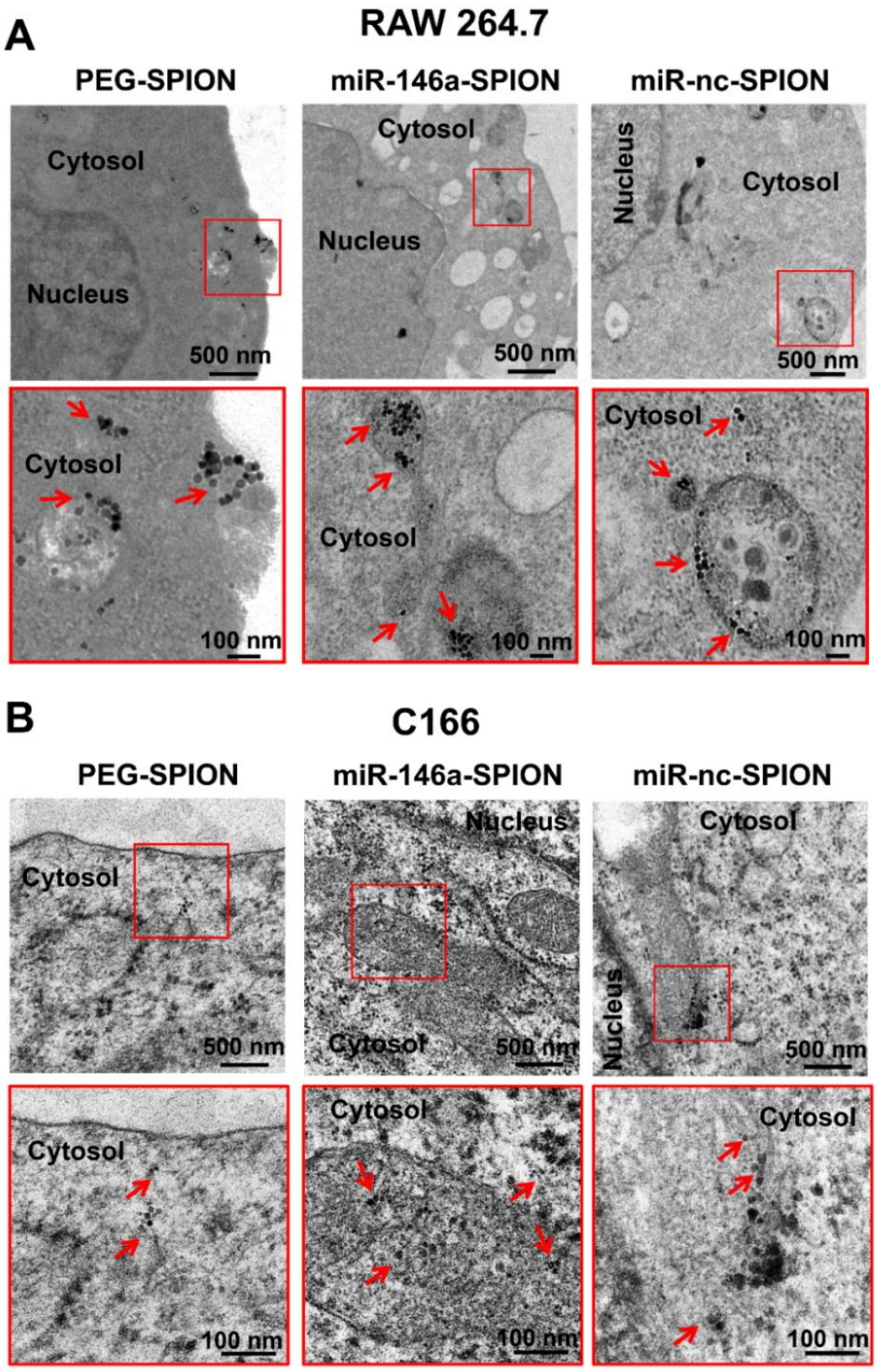

Fig. S14. Cellular association of PEG-SPIONs and miR-SPIONs by TEM. Representative TEM images verify that all types of SPIONs, including PEG-SPIONs, miR-146a-SPIONs and miR-nc-SPIONs, enter (**A**) RAW 264.7 cells and (**B**) C166 cells after incubation with the cells for 2 h. The bottom panel shows the enlargement of the boxed area in the top panel. Red arrows indicate SPIONs.

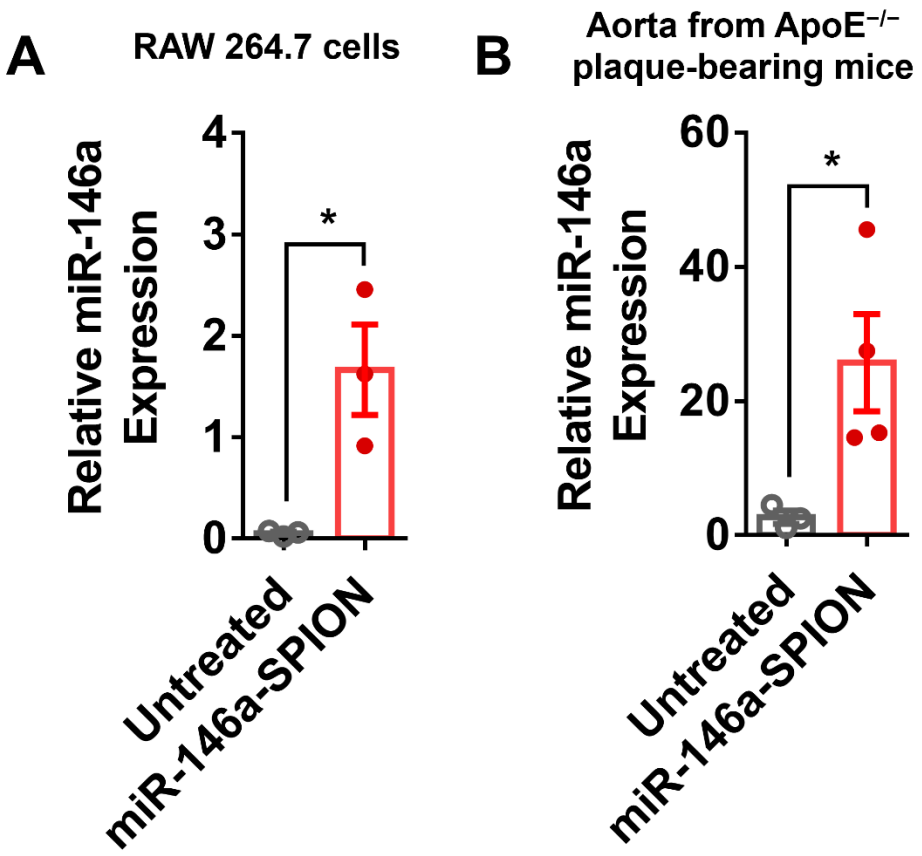

Fig. S15. Expression of miR-146a following the delivery of miR-146a-SPIONs. qRT-PCR measurements of miR-146a expression in (**A**) lipopolysaccharide (LPS)-treated RAW 264.7 macrophages after incubation with miR-146a-SPIONs for 24 h *in vitro* and (**B**) plaque-bearing ApoE$^{-/-}$ mice that underwent a complete treatment of 6 injections of miR-146a-SPIONs over three weeks *in vivo*. When compared to the untreated samples (black), the expression of miR-146a in the treated samples (red) was significantly upregulated *in vitro* and *in vivo*. qRT-PCR was performed using small nuclear RNA gene U6 as the internal control. Data are presented as mean ± SEM. Statistical significance is calculated by Student's t-test, *P < 0.05. n = 3 cell samples per group, across 1 experiment. n = 3–4 mice per group, across 2 experiments.

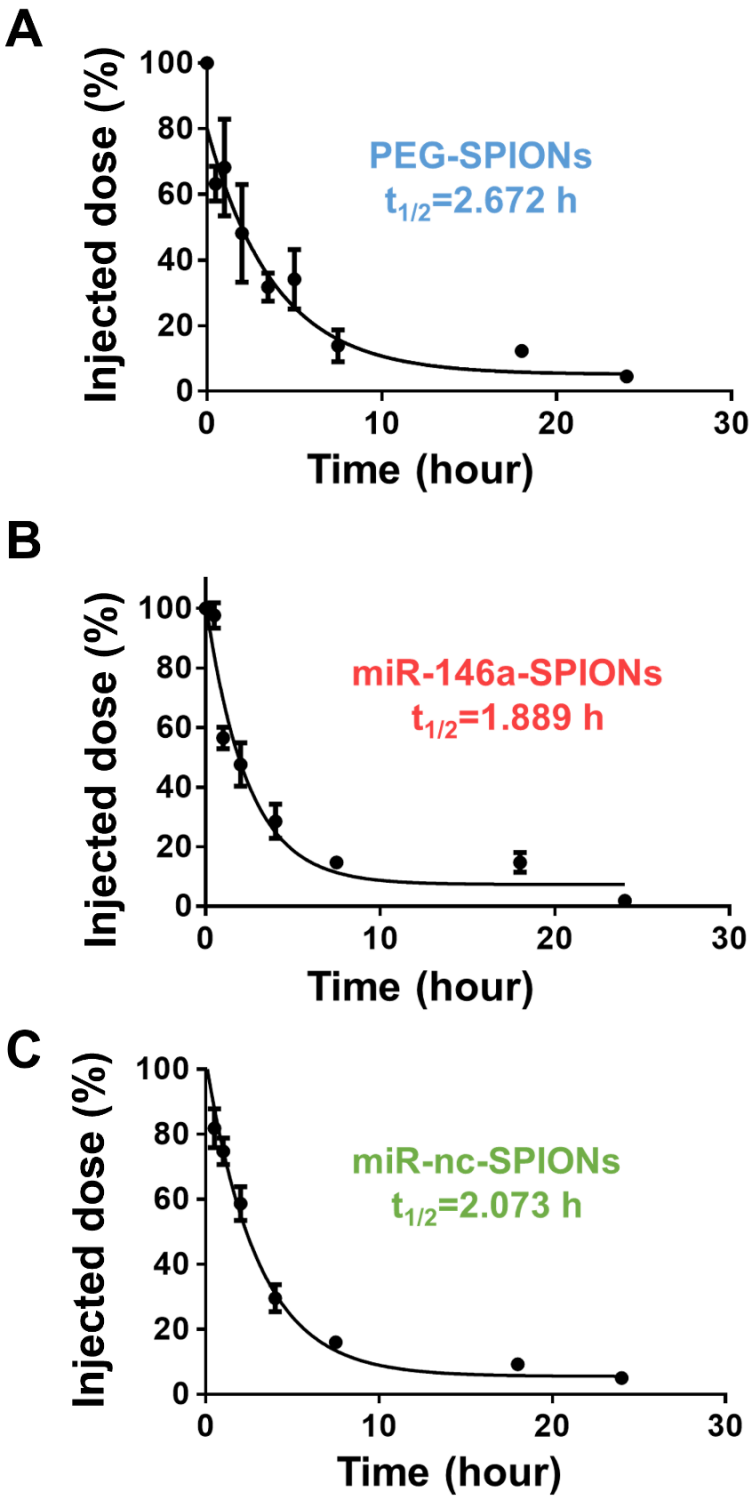

Fig. S16. Blood pharmacokinetics of PEG-SPIONs and miR-SPIONs in ApoE$^{-/-}$ mice. ICP-MS measurements of the iron content in blood reveal that (**A**) PEG-SPIONs show slightly slower blood clearance than (**B**) miR-146a-SPIONs and (**C**) miR-nc-SPIONs. Both types of miR-SPIONs show similar blood pharmacokinetics.

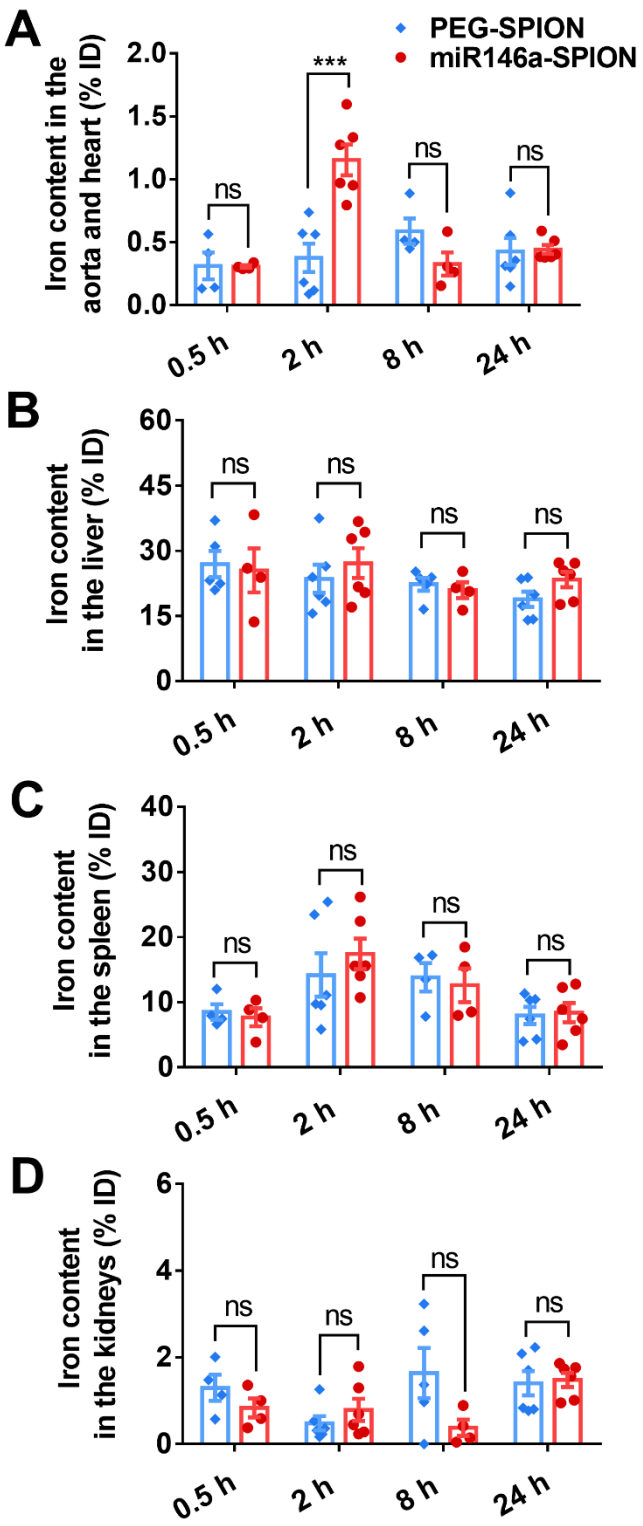

Fig. S17. Organ-level distribution of PEG-SPIONs and miR-146a-SPIONs in plaque-bearing ApoE$^{-/-}$ mice 0.5 h, 2 h, 8 h and 24 h post-injection. ICP-MS measurements of the iron content show miR-146a-SPIONs accumulate most abundantly in the (**A**) aorta and heart in plaque-bearing ApoE$^{-/-}$ mice 2 h post-injection. The iron contents of PEG-SPIONs (blue) and miR-146a-SPIONs (red) in the (**B**) liver, (**C**) spleen, and (**D**) kidneys are not significantly different in these organs at all time points. Data are presented as mean ± SEM. Statistical significance was calculated by Student's t-test, ns: not significant ($P > 0.05$), ***$P < 0.001$. n = 4–6 mice per group, across 2 experiments.

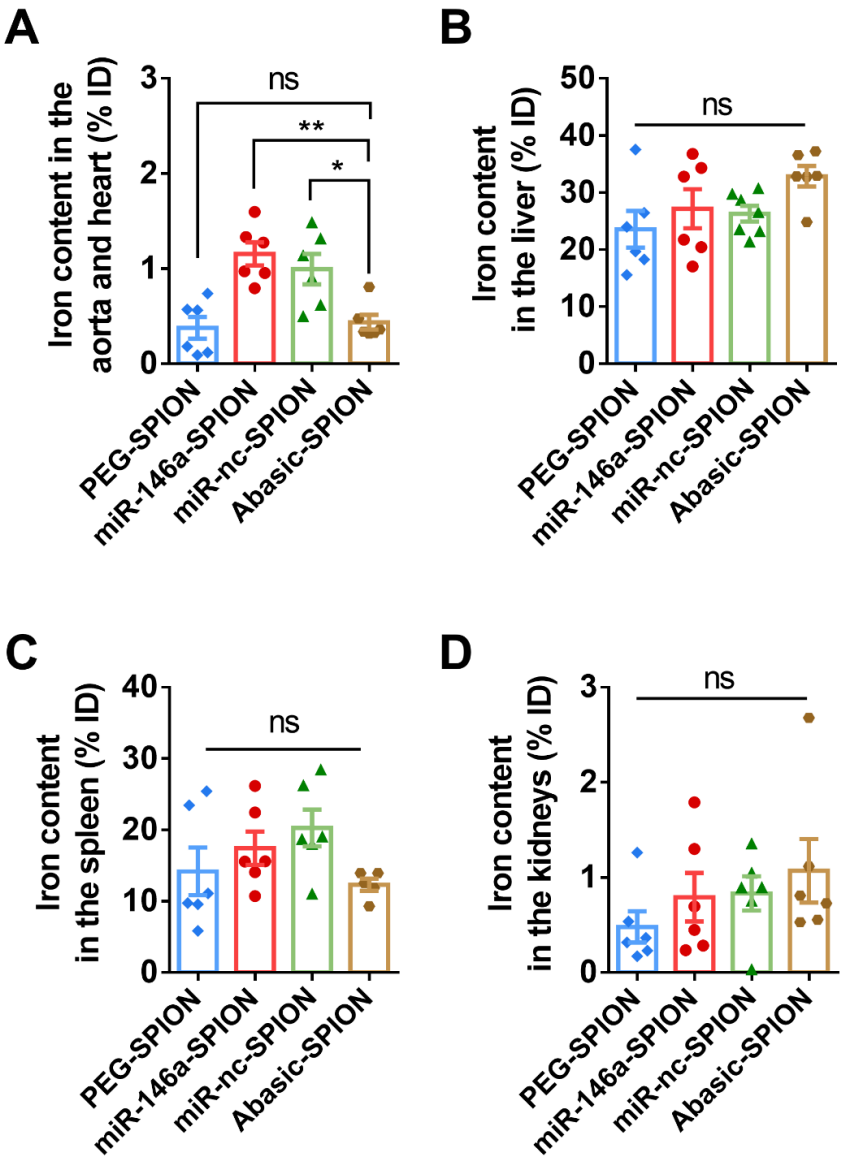

Fig. S18. Organ-level distribution of different types of SPIONs in ApoE$^{-/-}$ mice 2 h post-injection. ICP-MS measurements of the iron content in the (**A**) aorta and heart revealed a similar accumulation of abasic-SPIONs to that of PEG-SPIONs but significantly lower than those of miR-146a-SPIONs or miR-nc-SPIONs. ICP-MS measurements of the iron content in the (**B**) liver, (**C**) spleen, and (**D**) kidneys revealed no significant difference in the accumulation of PEG-SPIONs (blue), miR-146a-SPIONs (red), miR-nc-SPIONs (green), and abasic-SPIONs (brown) in these organs. Data are presented as means ± SEM. Statistical significance was calculated by one-way ANOVA with Tukey's Test for post-hoc analysis. ns: not significant ($P > 0.05$), *$P < 0.05$, **$P < 0.01$. n = 6 mice per group, across 2 experiments.

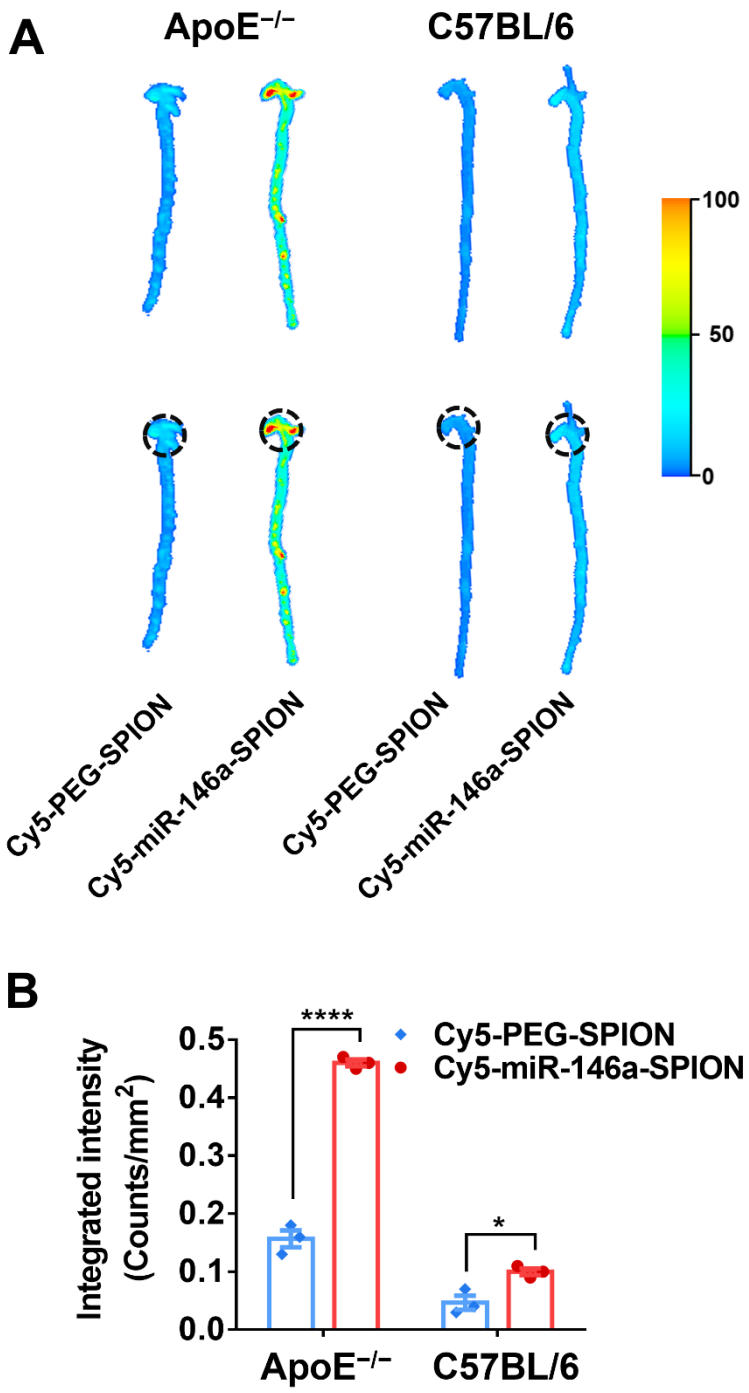

Fig. S19. Accumulation of Cy5-labeled PEG-SPIONs and miR-146a-SPIONs in the aorta and heart of plaque-bearing ApoE$^{-/-}$ mice and healthy C57BL/6 mice 2 h post-injection. (**A**) Representative *ex vivo* NIRF imaging of the aorta of plaque-bearing ApoE$^{-/-}$ mice or healthy C57BL/6 mice. Black dotted line indicates the region of interest (ROI). (**B**) The corresponding fluorescence intensities (per unit area) at the plaque sites. Accumulation of Cy5-miR-146a-SPIONs in the plaque is significantly abundant than Cy5-PEG-SPIONs. Data are presented as mean ± SEM. Statistical significance was calculated by Student's t-test, ns: not significant ($P > 0.05$), *$P<0.05$, ****$P<0.0001$. n = 3 mice per group, across 1 experiment.

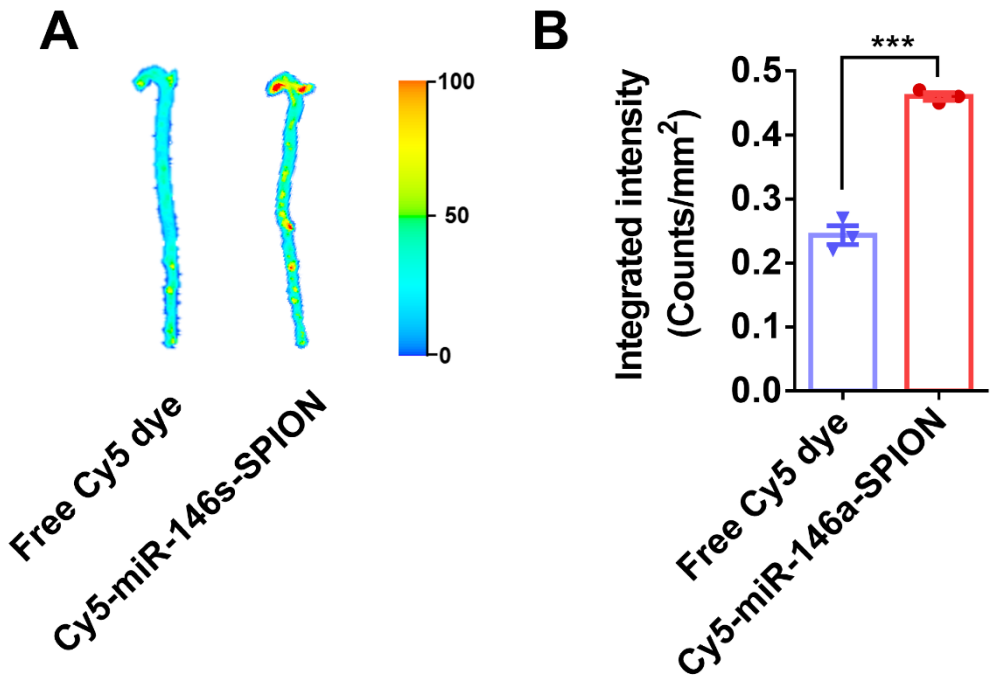

Fig. S20. Accumulation of Cy5-labeled miR-146a-SPIONs and free Cy5 dyes in the aorta of plaque-bearing ApoE$^{-/-}$ mice 2 h post-injection. (**A**) Representative e*x vivo* NIRF imaging of the aorta excised from plaque-bearing ApoE$^{-/-}$ mice. (**B**) The corresponding fluorescence intensities (per unit area) at the plaque sites. Accumulation of Cy5-miR-146a-SPIONs in the plaque is pronouncedly higher than free Cy5 dye. This experiment supports the flow cytometry data on free Cy5 dyes in Fig. S24. Data are presented as mean ± SEM. Statistical significance is calculated by Student's t-test. ***P<0.001. n = 3 mice per group, across 1 experiment.

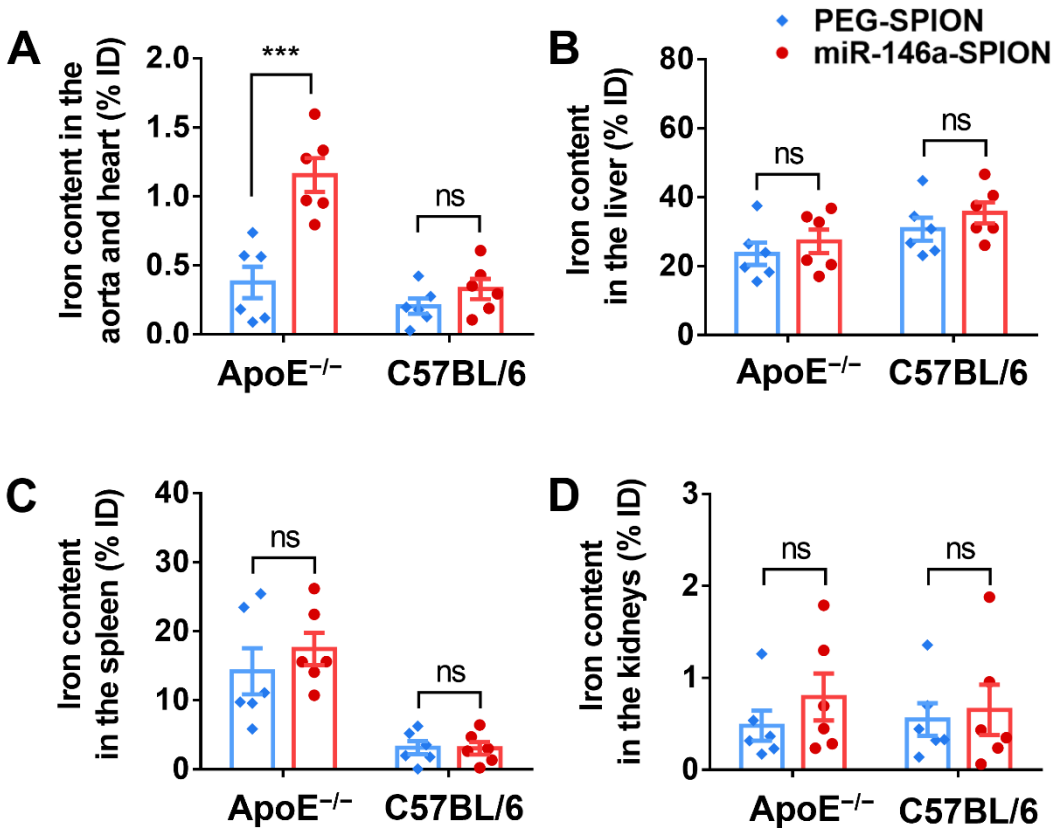

Fig. S21. Accumulation of PEG-SPIONs and miR-146a-SPIONs in the aorta and heart of plaque-bearing ApoE$^{-/-}$ mice and healthy C57BL/6 mice 2 h post-injection. By ICP-MS measurements, miR-146a-SPIONs more pronouncedly accumulate in (**A**) the aorta and heart of plaque-bearing ApoE$^{-/-}$ mice than PEG-SPIONs, but not in healthy C57BL/6 mice. The iron content in the (**B**) liver, (**C**) spleen, and (**D**) kidneys reveal no significant difference in the accumulation of PEG-SPIONs and miR-146a-SPIONs (red) for both types of mice. These results indicate the preferential delivery of miR-146a-SPIONs to atherosclerotic plaques. Data are presented as mean ± SEM. Statistical significance was calculated by one-way ANOVA with Tukey's Test for post-hoc analysis. ns: not significant ($P > 0.05$), ***$P < 0.001$. n = 6 mice per group, across 2 experiments.

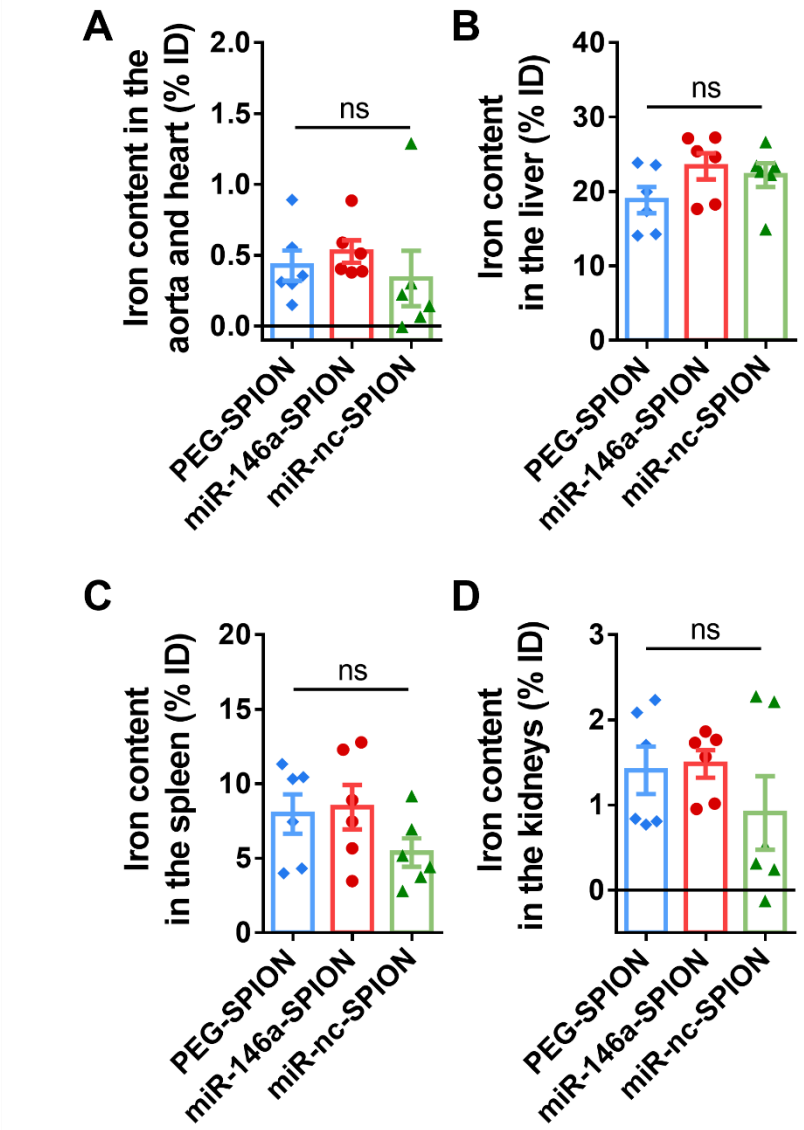

Fig. S22. Organ-level distribution of PEG-SPIONs and miR-SPIONs in plaque-bearing ApoE$^{-/-}$ mice 24 h post-injection. ICP-MS measurements of the iron content in the (**A**) aorta and heart, (**B**) liver, (**C**) spleen, and (**D**) kidneys reveal no significant difference in the accumulation of PEG-SPIONs (blue), miR-146a-SPIONs (red), and miR-nc-SPIONs (green) in these organs. Data are presented as means ± SEM. Statistical significance was calculated by one-way ANOVA with Tukey's Test for post-hoc analysis. ns: not significant ($P > 0.05$). n = 6 mice per group; across 2 experiments.

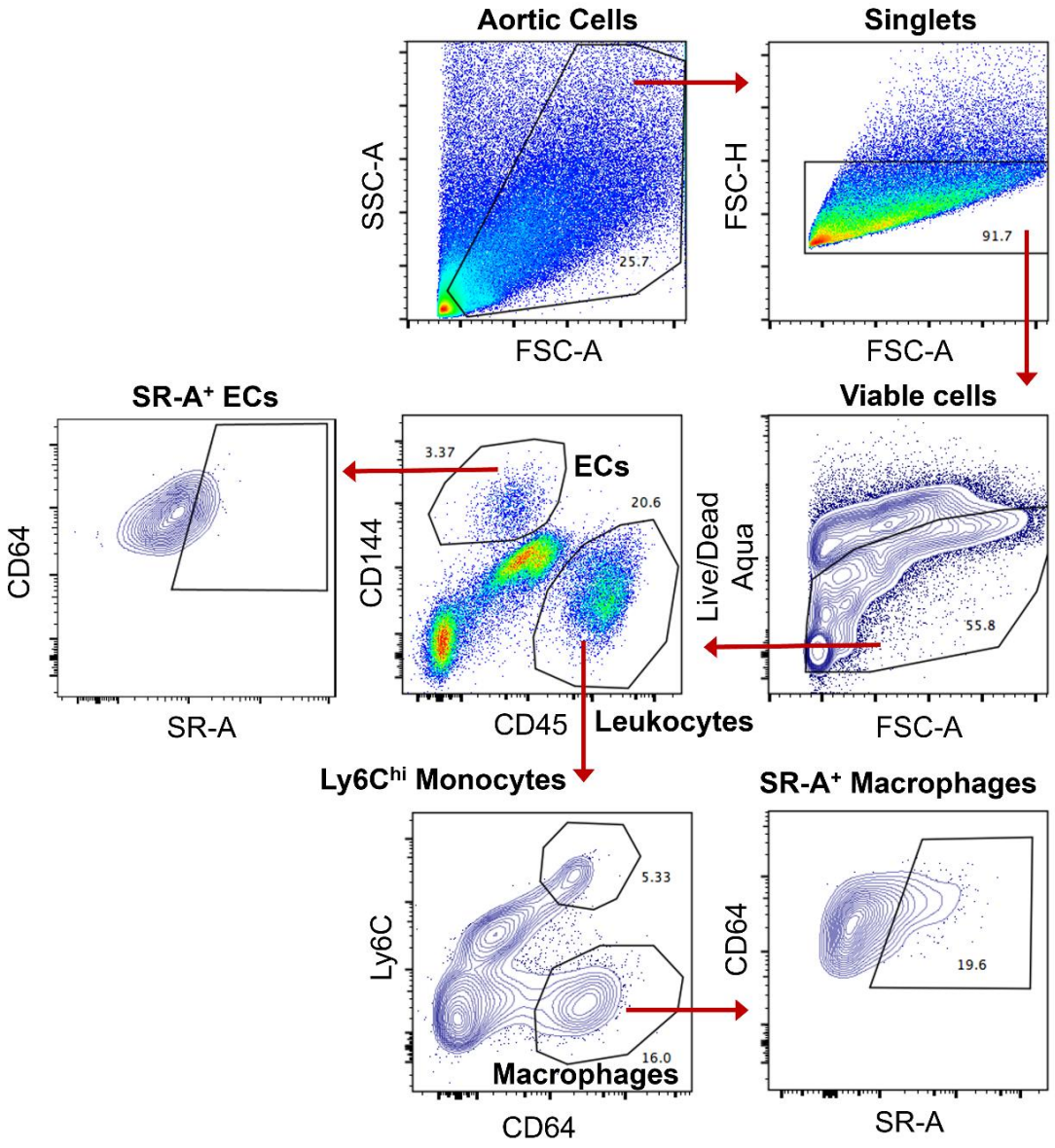

Fig. S23. Flow cytometry gating strategy for calculating the cellular-level distribution of PEG-SPIONs and miR-SPIONs to the aortic cells 2 h post-injection. A single cell suspension from the intact aorta was gated on FSC-A and SSC-A to exclude cell debris, followed by exclusion of doublets on FSC-H. Singlets were then gated on Live/Dead Aqua for viable cells. Cells were separated in different staining panels. Aortic macrophages: $CD45^{+}CD64^{+}Ly6C^{lo}$; ECs: $CD45^{-}CD144^{+}$; monocyte-macrophages: $CD45^{+}Ly6C^{hi}CD64^{mid}$. Macrophages and ECs were further gated on SR-A for $SR\text{-}A^{+}$ macrophages and $SR\text{-}A^{+}$ ECs.

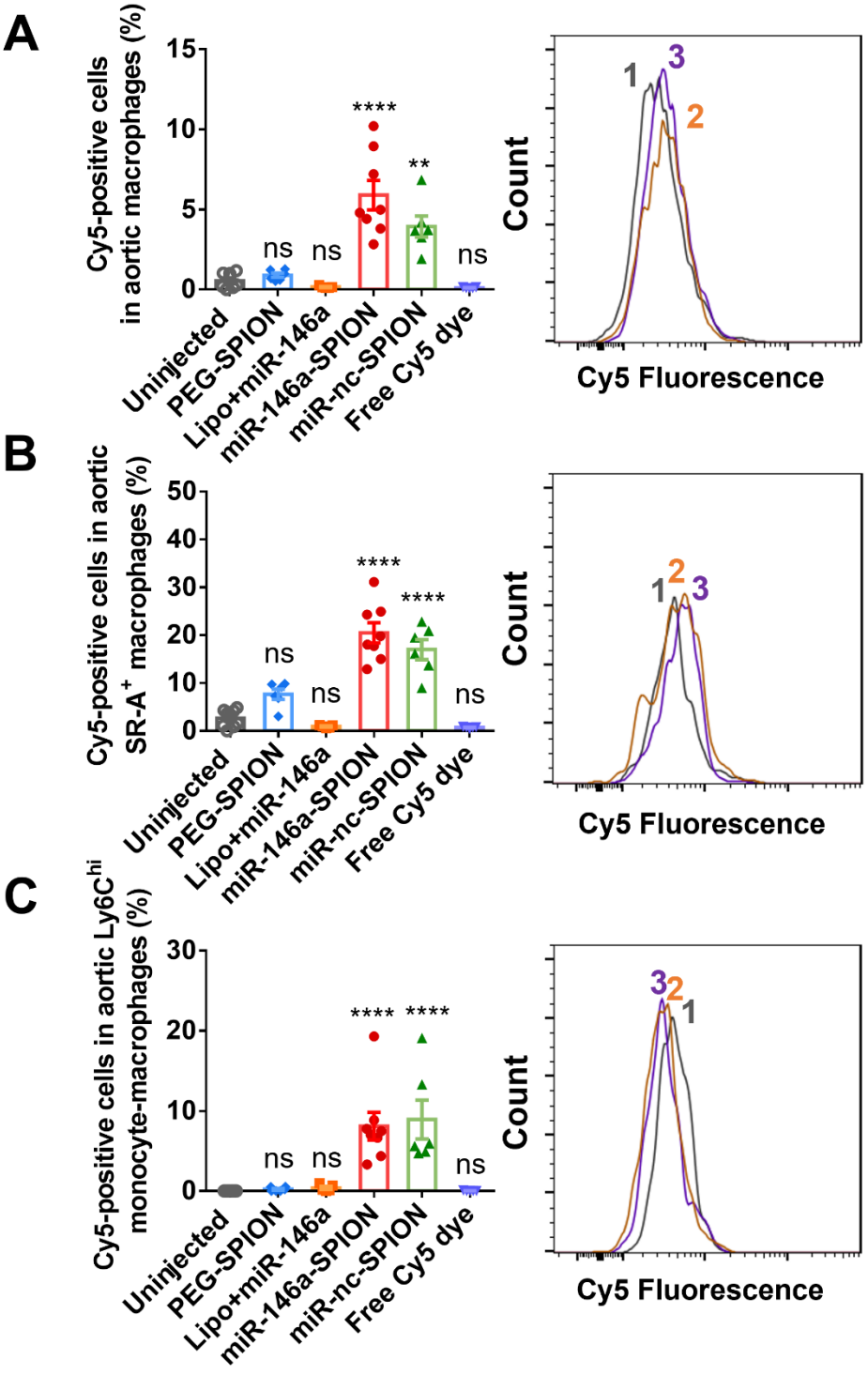

1. Uninjected 2. Lipo+Cy5-miR-146a 3. Free Cy5 dye

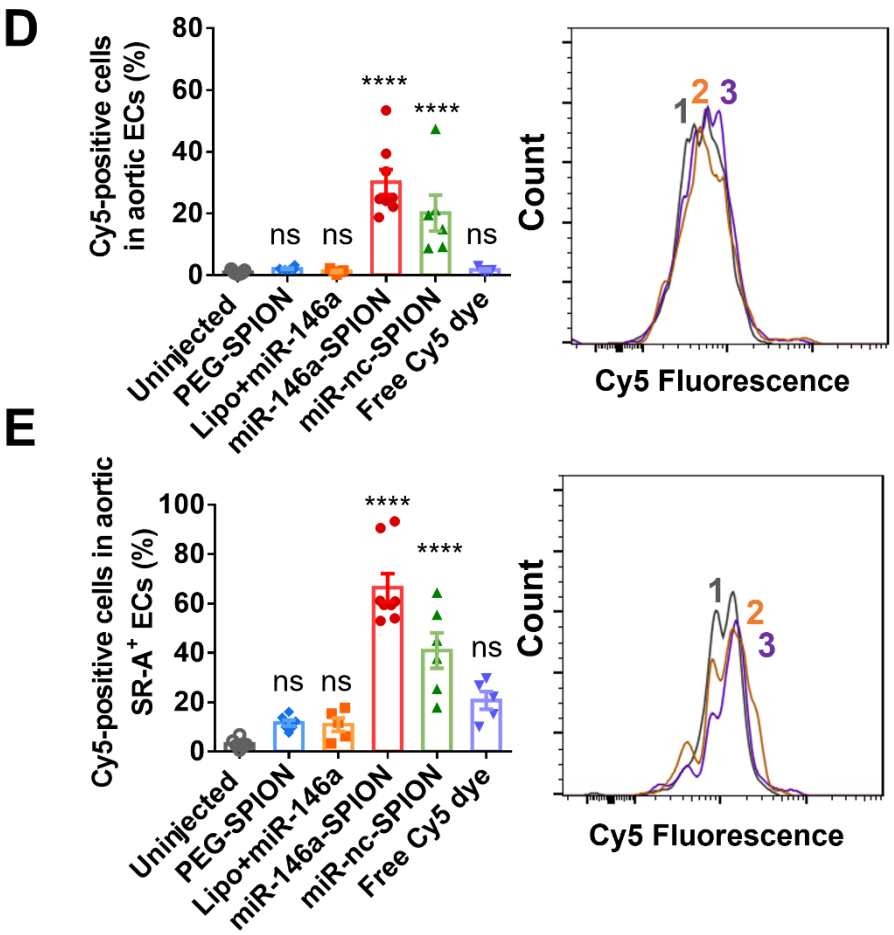

Fig. S24. Cellular-level distribution of Lipo+Cy5-miR-146a nanocomplex and free Cy5 dye in the aorta of ApoE$^{-/-}$ mice 2 h post-injection. Flow cytometric analysis and representative flow cytometry histograms of the single cells collected from the aorta indicate that Lipofectamine does not effectively deliver Cy5-miR to the (**A**) total macrophages, (**B**) SR-A^{+} macrophages, (**C**) monocyte-derived macrophages and (**D**) total ECs (**E**) SR-A^{+} ECs. The data also indicate that free Cy5 molecules show distinct histograms than Cy5-miR-146a-SPIONs. This experiment supports the data shown in Fig. 2C and 2D. Data are presented as means ± SEM. Statistical significance was calculated by one-way ANOVA with Tukey's Test for post-hoc analysis. ns: not significant (P > 0.05), *P < 0.05, ***P < 0.001, ****P < 0.0001. n =5–8 mice per group; across 2 experiments.

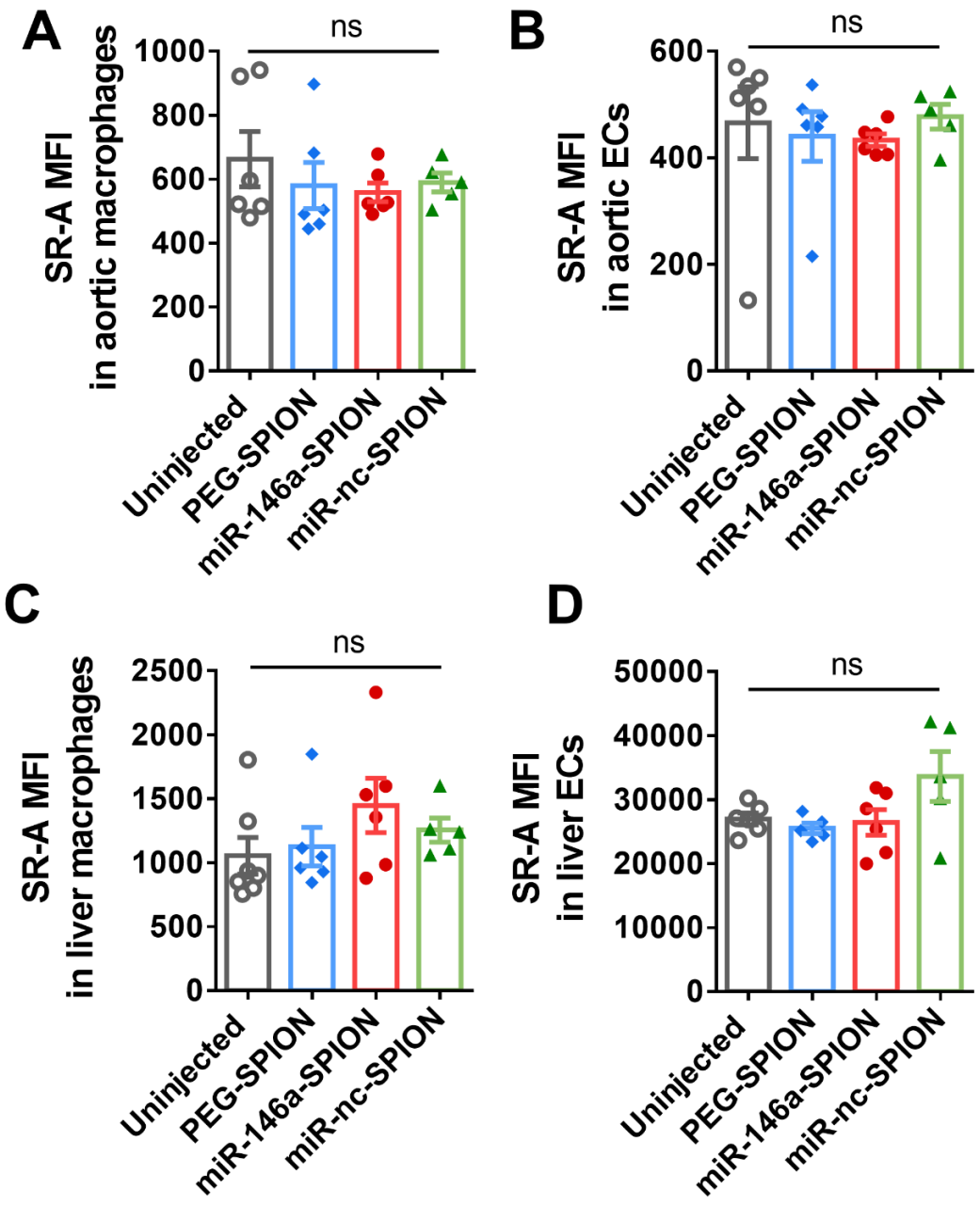

Fig. S25. SR-A expression in the aortic cells of ApoE$^{-/-}$ mice. SR-A MFI of aortic (**A**) macrophages, (**B**) ECs, liver (**C**) macrophages and (**D**) ECs were detected by flow cytometry after 2 h i.v. injection. This experiment supports the data shown in Fig. 2C and 2D. Data are presented as means ± SEM (n = 5−7; across 2 experiments). Statistical significance was calculated by one-way ANOVA with Tukey's Test for post-hoc analysis. ns: not significant (P > 0.05).

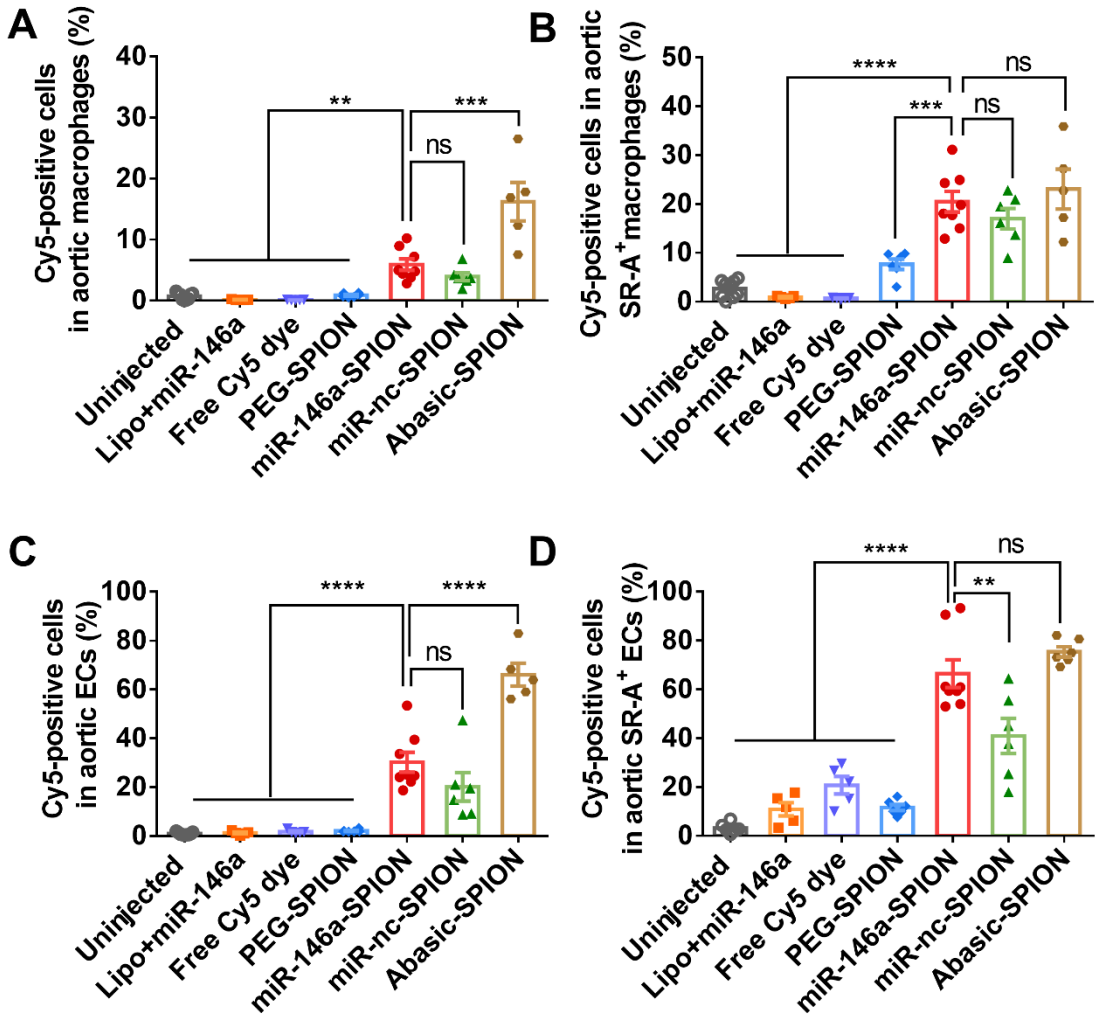

Fig. S26. Cellular-level distribution of different types of SPIONs, Lipo+Cy5-miR-146a nanocomplex, and free Cy5 dyes in the aorta of ApoE$^{-/-}$ mice 2 h post-injection. Flow cytometry analysis showed that abasic-SPIONs did not preferentially associate to (**B**) SR-A-rich macrophages and (**D**) SR-A rich endothelial cells (ECs) in the aorta, different from miR-146a-SPIONs. For abasic-SPIONs, the Cy5-positive cells in total macrophages is (16.2%) similar to that in SR-A-positive macrophages (23.0%). By contrast, for miR-146a-SPIONs, the Cy5-positive cells in SR-A positive macrophages (20.5%) is significantly higher than total macrophages (5.9%). This experiment supports the data shown in Fig. 2C, Fig. 2D and Fig. S20. Data are presented as means ± SEM. Statistical significance was calculated by one-way ANOVA with Tukey's Test for post-hoc analysis. ns: not significant ($P > 0.05$), *$P < 0.05$, **$P < 0.01$, ***$P < 0.001$, ****$P < 0.0001$. n =5–8 mice per group, across 3 experiments.

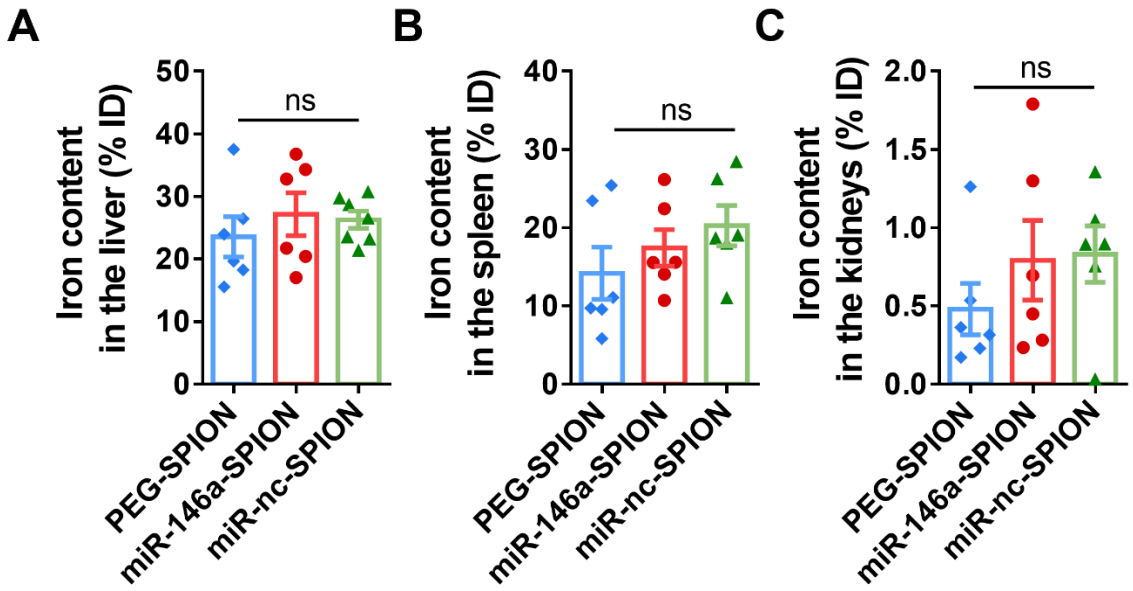

Fig. S27. Organ-level distribution of PEG-SPIONs and miR-SPIONs in ApoE$^{-/-}$ mice 2 h post-injection. ICP-MS measurements of the iron content in the (**A**) liver, (**B**) spleen, and (**C**) kidneys reveal no significant difference in the accumulation of PEG-SPIONs (blue), miR-146a-SPIONs (red), and miR-nc-SPIONs (green) in these organs. Data are presented as means ± SEM. Statistical significance was calculated by one-way ANOVA with Tukey's Test for post-hoc analysis. ns: not significant ($P > 0.05$). n = 6 per group, across 2 experiments.

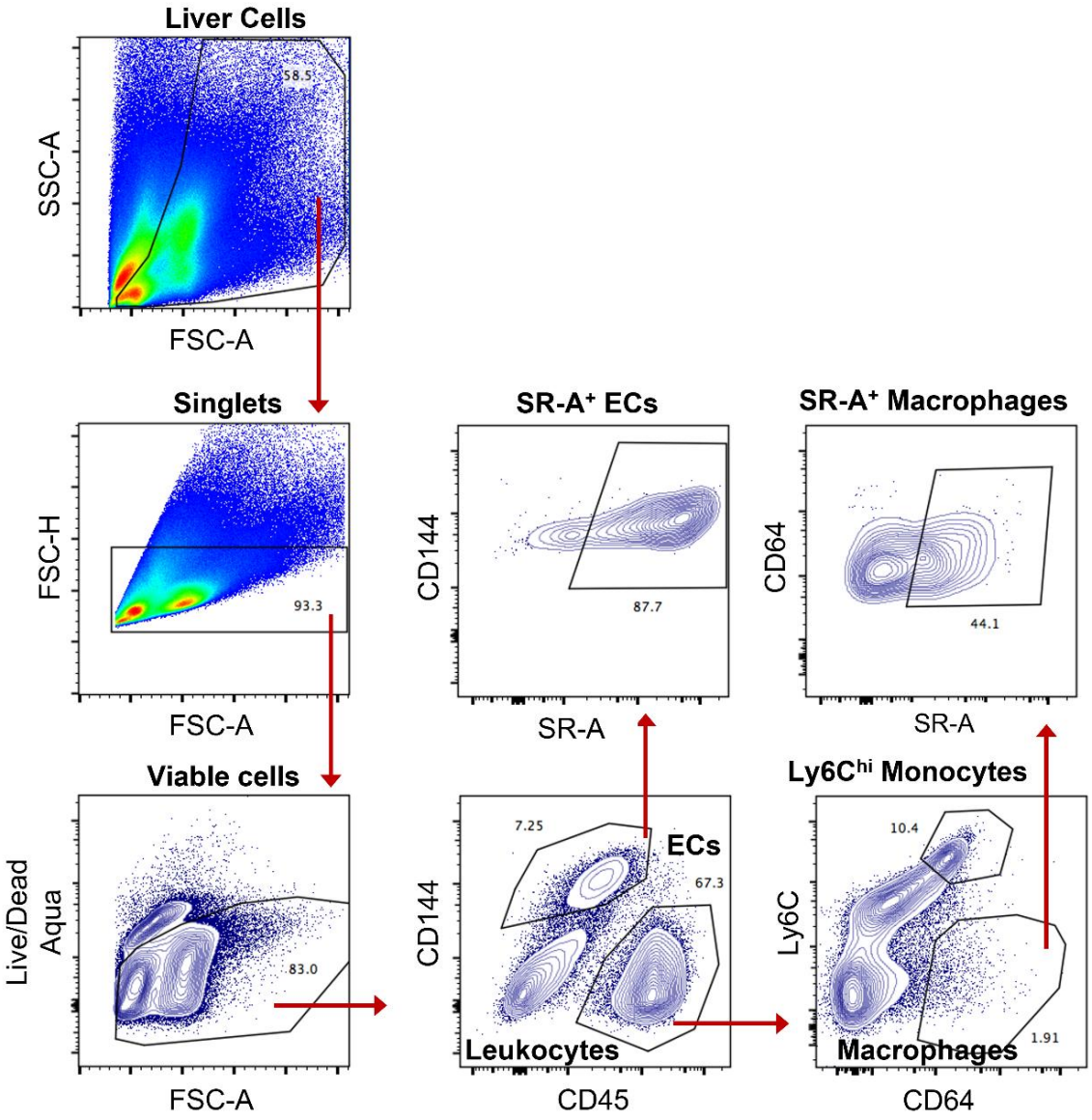

Fig. S28. Flow cytometry gating strategy for calculating the cellular-level distribution of PEG-SPIONs and miR-SPIONs to the liver cells 2h post-injection. A single cell suspension from the liver was gated on FSC-A and SSC-A to exclude cell debris, followed by exclusion of doublets on FSC-H. Singlets were gated on Live/Dead Aqua for viable cells to the liver cell population. From this point, cells were separated in different staining panels. Liver total macrophages: $CD45^{+}CD64^{+}Ly6C^{lo}$; total ECs: $CD45^{-}CD144^{+}$; monocyte-macrophage: $CD45^{+}Ly6C^{hi}CD64^{mid}$. Macrophages were further gated on SR-A for $SR\text{-}A^{+}$ macrophages.

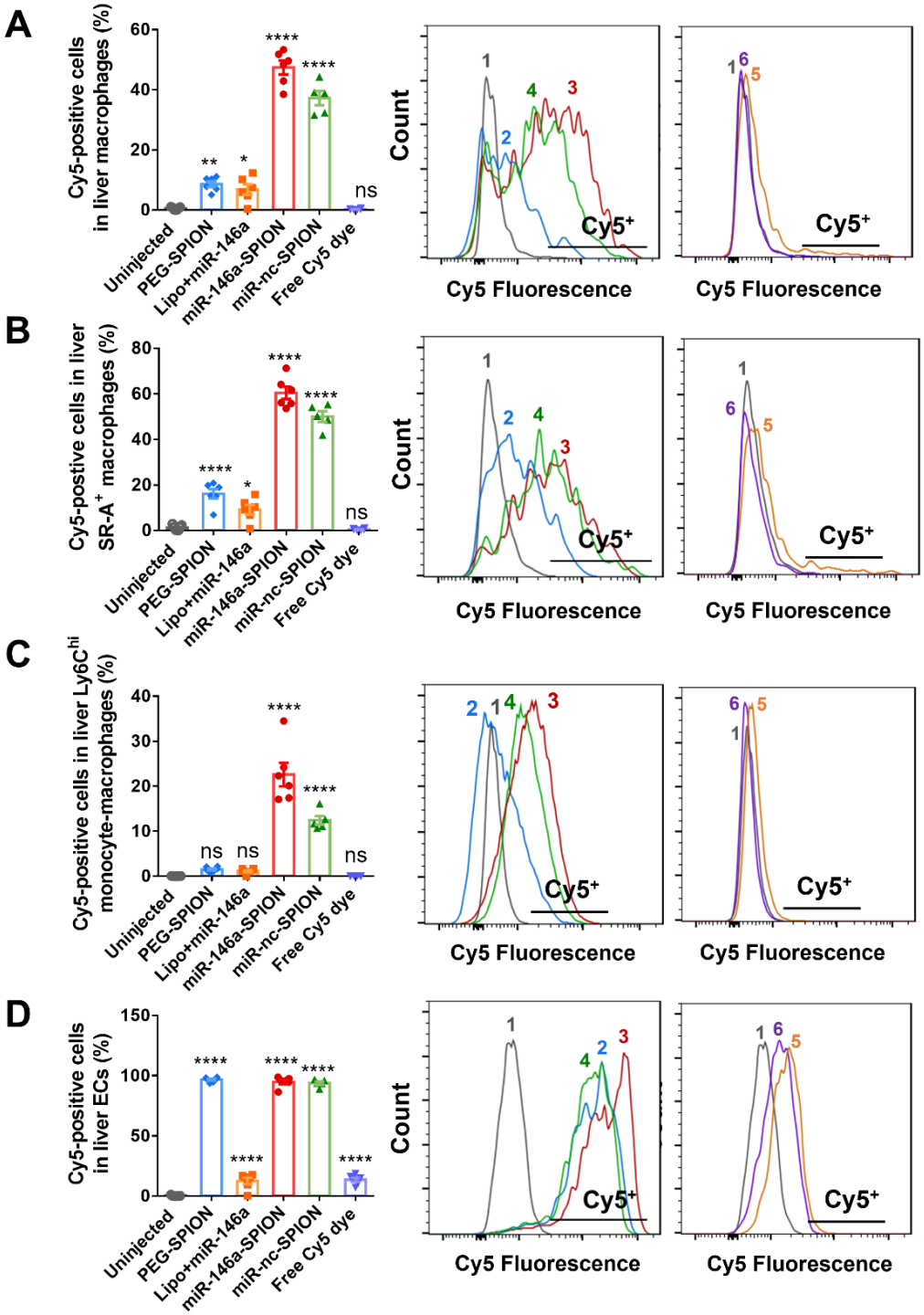

1. Uninjected 2. PEG-SPION 3. miR-146a-SPION 4. miR-nc-SPIONs 5. Lipo+Cy5-miR-146a 6. Free Cy5 dye

Fig. S29. Cellular-level distribution of Lipo+Cy5-miR-146a nanocomplex and free Cy5 dye in the liver of ApoE$^{-/-}$ mice 2 h post-injection. Flow cytometric analysis and representative flow cytometry histograms of the single cells collected from the liver indicate that Lipofectamine does not deliver Cy5-miR to the (**A**) total macrophages, (**B**) SR-A-rich macrophages, (**C**) monocyte-macrophages and (**D**) ECs as effectively as miR-SPIONs. Data on percentage of Cy5-positive cells show that liver total macrophages, monocyte-derived macrophages, and CD204^{+} macrophages most likely associate with Cy5-miR-SPIONs of all SPIONs tested, but liver ECs associate with all types of SPIONs to similar extents. The data also indicate that free Cy5 molecules show distinct histograms than Cy5-miR-146a-SPIONs.

Data are presented as means ± SEM. Statistical significance was calculated by one-way ANOVA with Tukey's Test for post-hoc analysis. ns: not significant (P > 0.05), *P < 0.05, **P < 0.01, ****P <0.0001. n = 5–7 mice per group; across two experiments.

Cellular-level distribution of SPIONs in the liver

As ~30 % ID of the SPIONs accumulate in the liver 2 h post-injection (Fig. S27A), we studied their cellular-level distribution in the liver by flow cytometry (see gating strategy in Fig. S28). The mean fractions of Cy5-positive liver total macrophages for the Cy5-miR-146a-SPION (47.4%) and Cy5-miR-nc-SPION (37.2%) groups are 4–5 folds higher than that of the Cy5-PEG-SPION group (8.6%) (Fig. S29A). Similarly, the mean fractions of Cy5-positive liver SR-A-rich macrophages for the Cy5-miR-146a-SPION (60.4%) and Cy5-miR-nc-SPION (50.0%) groups are 3–4 fold higher than that of Cy5-PEG-SPION group (16.1%) (Fig. S29B). These data agree with the findings for aortic macrophages that the miRNA shell promotes delivery to liver total macrophages, and more preferentially to liver SR-A-rich macrophages. These data also agree with the much higher SR-A expression or fraction on liver ECs than aortic ECs (Fig. S25 and Fig. S30). Contrary to aortic total ECs, the mean fractions of Cy5-positive liver total ECs are similarly high for all three SPION groups, mostly >90% (Fig. S29D). The miRNA shell does not promote delivery to liver total ECs, in line with literature precedent on the abundant clearance of i.v. injected PEG-coated gold NPs by liver total ECs, possibly due to the reduced blood flow in the liver sinusoidal capillaries that encourage interaction between the NPs and ECs (*14*). Given the high fractions of Cy5-positive liver total ECs, it was challenging to quantify the association of SPIONs to liver SR-A-rich ECs.

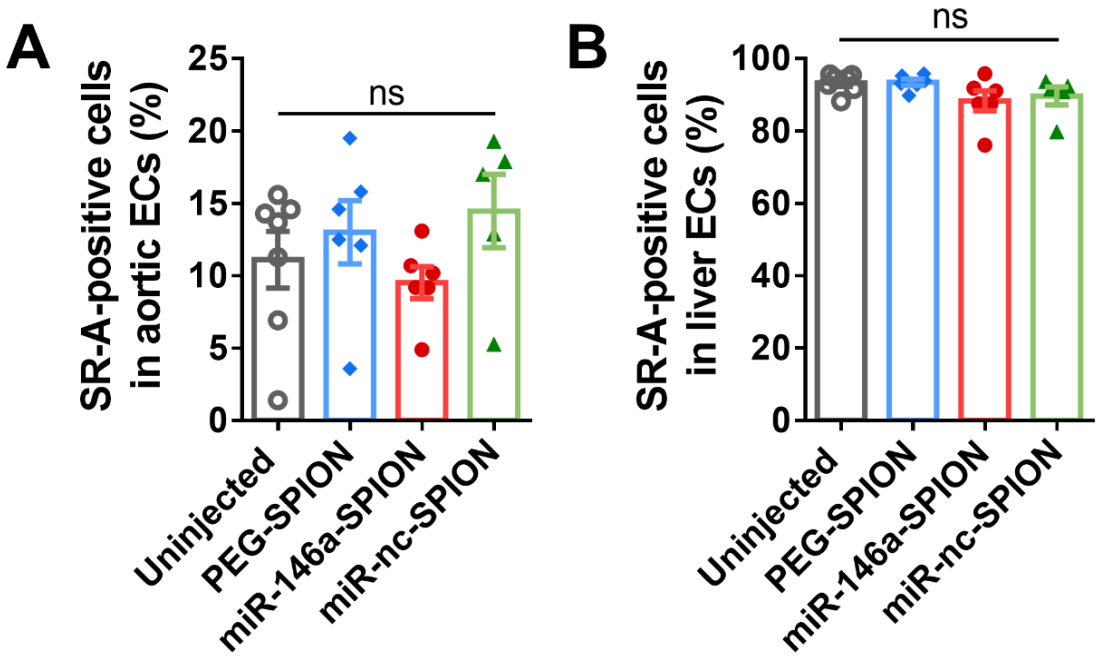

Fig. S30. The fraction of SR-A-positive cells in liver ECs of ApoE$^{-/-}$ mice. SR-A-positive cells percentage of (**A**) aortic ECs and (**B**) liver ECs were detected by flow cytometry after 2 h i.v. injection. This figure supports the data shown in Fig. 2C and Fig. S29D. Data are presented as means ± SEM Statistical significance was calculated by one-way ANOVA with Tukey's Test for post-hoc analysis. ns: not significant (P > 0.05). n = 5−7; across 2 experiments.

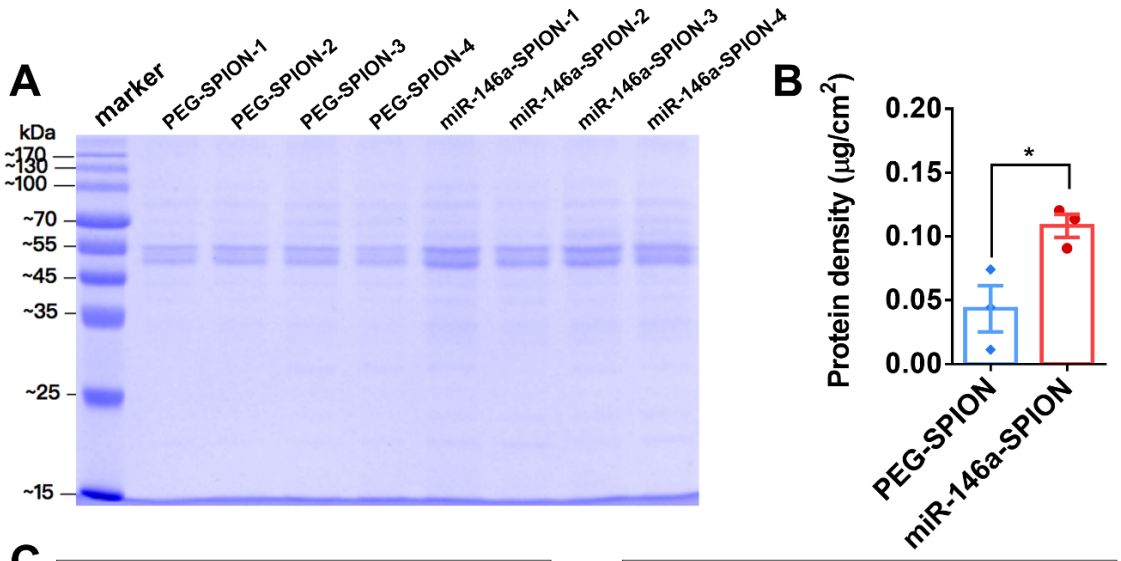

C

PEG-SPION		
Symbol	MW (kDa)	% (w/w)
Fgb	54.752	16.71
Fgg	50.349	15.69
Fga	87.428	12.13
Alb	68.692	7.40
Hbbt1	15.748	3.76
Ighm	49.943	2.98
Apoa1	30.615	2.79
Vwf	309.150	2.67
Actb	41.736	2.38
Hba2	15.112	1.94
F13b	76.195	1.72
Apob	509.430	1.59
Apoa4	45.029	1.48
Vtn	54.848	1.32
Kng1	73.100	1.25
F13a1	83.206	1.19
Abcb9	29.521	1.02
Prss1	26.134	0.94
Slc4a1	103.130	0.92
Plg	90.807	0.87

miR-146a-SPION		
Symbol	MW (kDa)	% (w/w)
Fgb	54.752	21.37
Fgg	50.349	17.87
Fga	87.428	11.52
Alb	68.692	3.69
Apoa1	30.615	2.94
Hbbt1	15.748	2.47
F13b	76.195	2.03
Apob	509.430	2.02
Kng1	73.100	1.96
Hba2	15.112	1.73
Ighm	49.943	1.73
F13a1	83.206	1.70
Vtn	54.848	1.66
Apoa4	45.029	1.60
Vwf	309.150	1.45
Actb	41.736	1.31
Plg	90.807	1.27
Abcb9	29.521	1.21
Klkb1	71.382	1.13
Hrg	60.438	1.04

Fig. S31. Protein corona composition of PEG-SPIONs and miR-146a-SPIONs upon incubation in blood plasma of of ApoE$^{-/-}$ mice that were fed with a high-cholesterol diet for 12 weeks for 2 h. (**A**) Polyacrylamide gel electrophoresis (PAGE) analysis of adsorbed proteins after incubation of PEG-SPIONs and miR-146a-SPIONs in blood plasma at 37 ºC for 2 h. The darker bands in the miR-146a-SPION sample indicate more serum proteins bound to the SPION. (**B**) Density of adsorbed proteins on PEG-SPIONs and miR-146a-SPIONs by bicinchoninic acid (BCA) assay. More proteins were bound to miR-146a-SPIONs than PEG-SPIONs. Data are presented as mean ± SEM. Statistical significance was calculated by Student's t-test, *P <0.05. n = 3 cell samples per group, across 1 experiment. (**C**) The most abundant 20 proteins of the protein corona surrounding PEG-SPIONs and miR-146a-SPIONs as detected by label free liquid chromatograph-tandem mass spectrometry (LC−MS/MS) in triplicates. All blood plasma samples were collected from plaque-bearing ApoE$^{-/-}$ mice that

were fed with high-cholesterol diet for 12 weeks. Relative abundance (%) represents the weight percentage of each constituent protein. Proteins are represented by MGI symbols. (Abcb9) ATP-binding cassette sub-family B member 9; (Actb) Actin, cytoplasmic 1; (Alb) Albumin; (Apoa1) Apolipoprotein A-I; (Apoa4) Apolipoprotein A-IV; (Apob) Apolipoprotein B; (Fga) Fibrinogen alpha chain; (Fgb) Fibrinogen beta chain; (Fgg) Fibrinogen gamma chain; (F13a1) Coagulation factor XIII A chain; (F13b) Coagulation factor XIII B chain; (Hba2) Hemoglobin, alpha 2; (Hbbt1) Beta-globin; (Hrg) Histidine-rich glycoprotein; (Ighm) Immunoglobulin heavy constant mu; (Klkb1) Plasma kallikrein; (Kng1) Kininogen-1; (Plg) Plasminogen; (Prss1) Serine protease 1; (Slc4a1) Solute carrier family 4 member 1; (Vwf) von Willebrand factor. Values represent the percentage of each protein by weight.

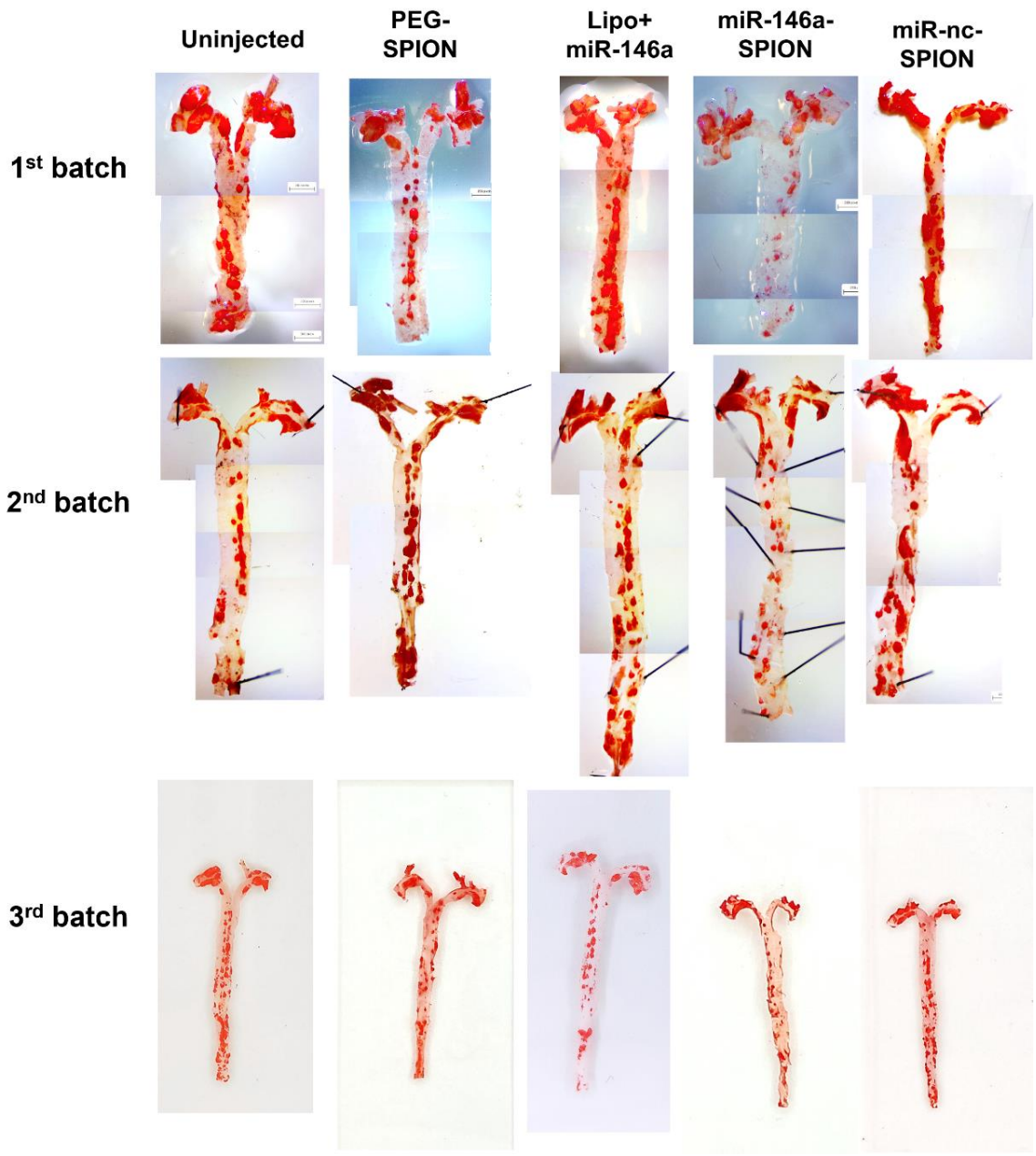

Fig. S32. Representative images of Oil Red O-stained intact aortas excised from ApoE$^{-/-}$ mice. These mice were either uninjected or received treatments of PEG-SPIONs, Lipo+miR-146a, miR-146a-SPIONs, or miR-nc-SPIONs. The 1st and 2nd batch of images were photographed using a CCD camera attached to a dissection microscope (Zeiss, Stemi 305) and optically stitched together. The 3rd batch of images was photographed by a regular camera.

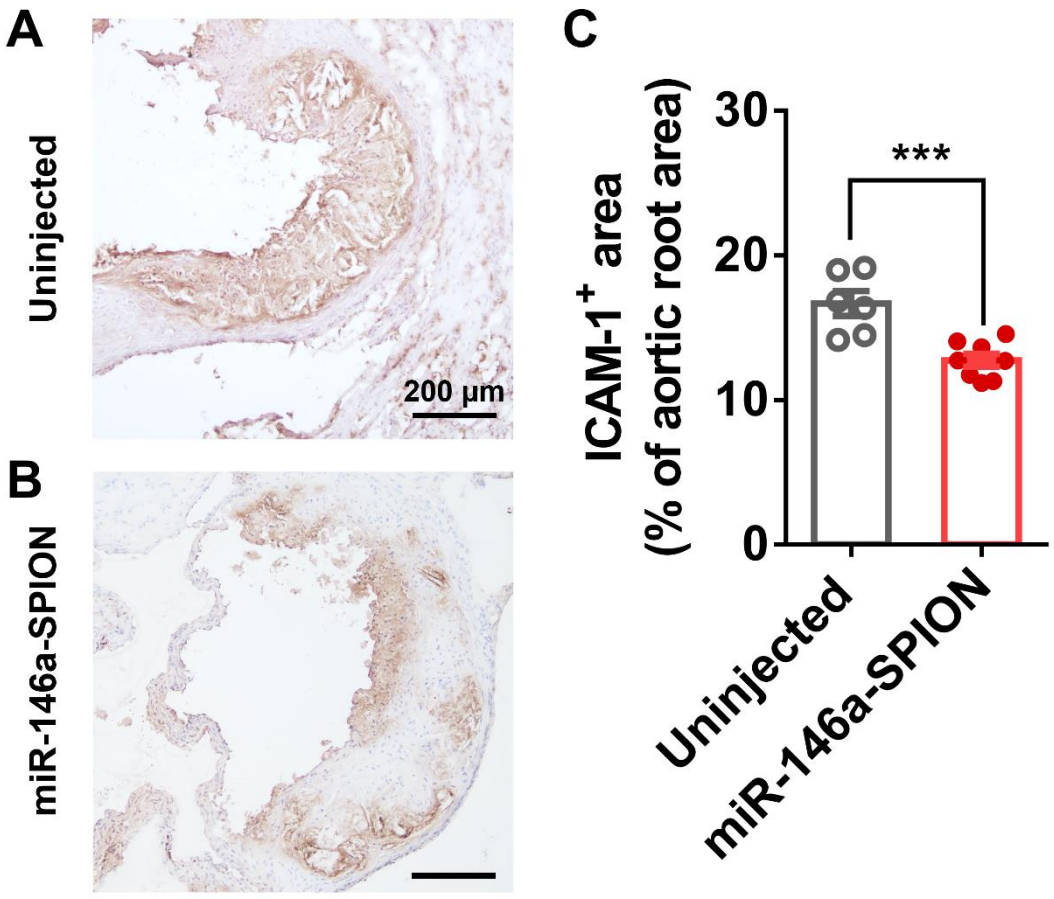

Fig. S33. Validation of the anti-atherosclerosis efficacy of miR-146a-SPOINs in ApoE$^{-/-}$ mice by IHC. The full treatment includes 6 doses of miR-146a-SPIONs over a period of 3 weeks. Representative IHC images of the sections of aortic roots from (**A**) uninjected and (**B**) miR-146a-SPIONs-treated groups reveal attenuated expression of ICAM-1 (brown) for the miR-146a-SPION group. (C) ICAM-1-positive area in the aortic root for the miR-146a-SPION group is significantly lower than that for the uninjected group. These data bolster the validity of the immunofluorescence-based efficacy evaluation in Fig. 4B of the main text. Data are presented as mean ± SEM. Statistical significance was calculated by Student's t-test, ***P < 0.001. n = 6–8 mice per group, across 3 experiments.

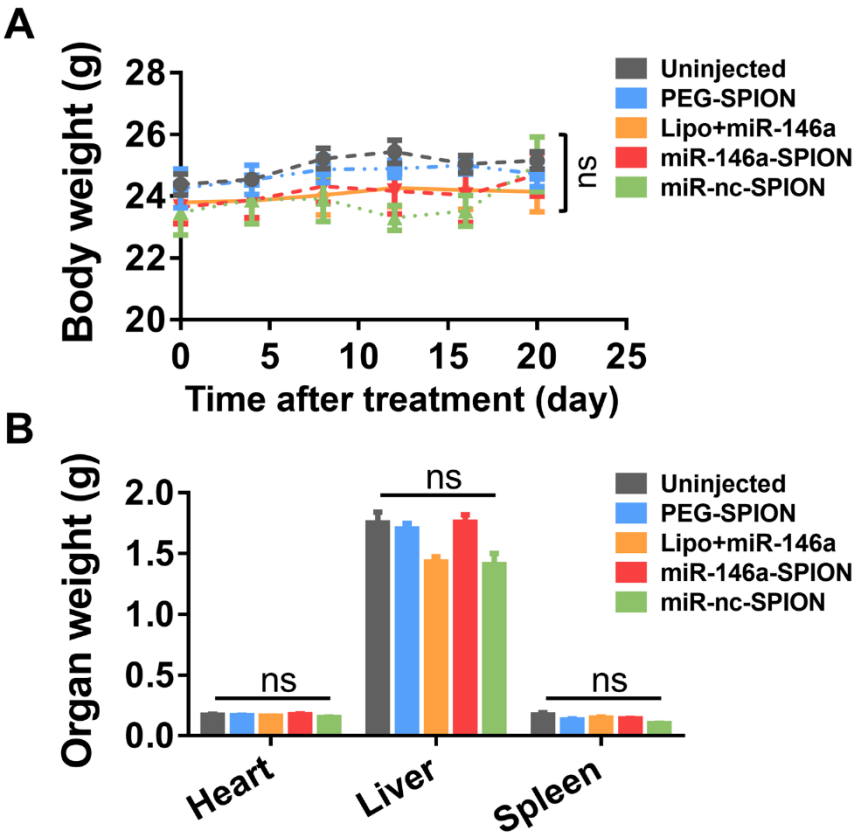

Fig. S34. *In vivo* toxicity following multiple administrations of various treatment groups to ApoE$^{-/-}$ mice. The administrations are based on the dose and dosing frequency of our treatment. (**A**) Body weight of mice from various treatment groups throughout the treatment. (**B**) Weight of major organs all treatment groups. Data are presented as means ± SEM. Statistical significance was calculated by one-way ANOVA with Tukey's Test for post-hoc analysis, ns: not significant ($P > 0.05$). n = 6–8 mice per group, across 3 experiments.

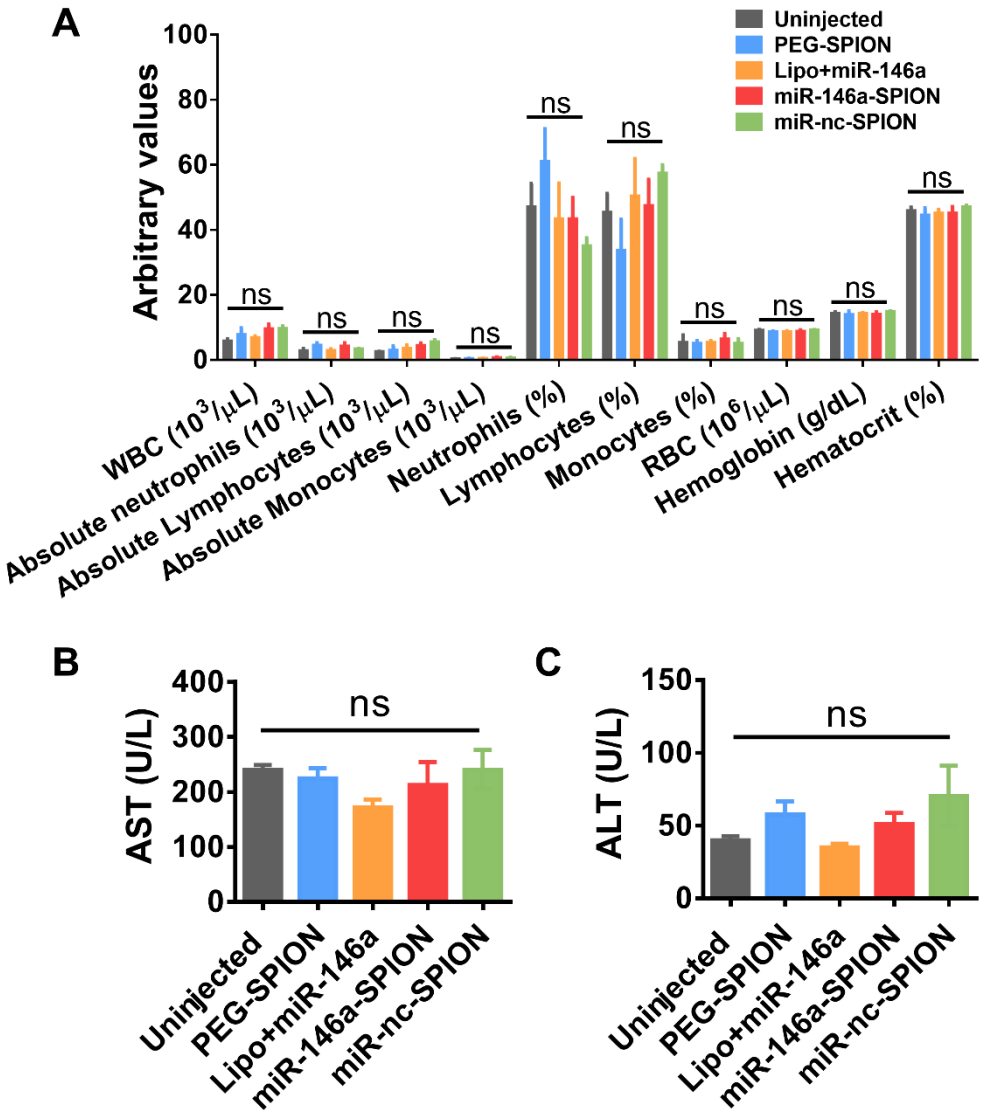

Fig. S35. *In vivo* toxicity of various treatment groups of ApoE$^{-/-}$ mice by complete blood cell count. Blood was collected 24 h after the last injection of PEG-SPIONs (blue), Lipo+miR-146a nanocomplex, miR-146a-SPIONs (red), or miR-ns-SPIONs (green). (**A**) Compared to uninjected mice (black), all treatment groups show no significant difference in blood chemistry markers or cell counts WBC: white blood cell. RBC: red blood cell. Absolute neutrophils, lymphocytes, or monocytes (10^3/μL): cell number per volume of blood. Neutrophils %, lymphocytes %, monocytes %: percentage cells among total WBC. RBC (10^6/μL): cell number per volume of blood. Liver toxicity examined by measuring levels of serum (**B**) aspartate transaminase (AST) and (**C**) alanine transaminase (ALT). Data are presented as mean ± SEM. Statistical significance was calculated by one-way ANOVA with Tukey's Test for post-hoc analysis, ns: not significant ($P > 0.05$). n=3 mice per group, across 1 experiment.

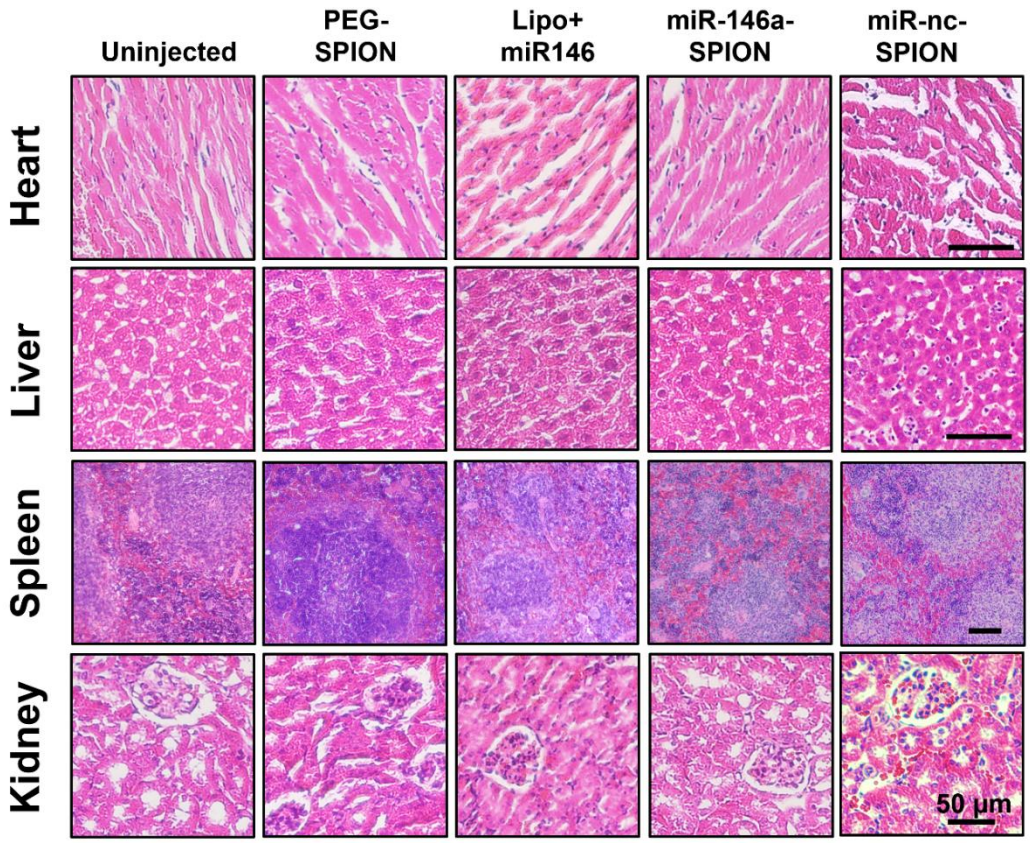

Fig. S36. Histological examination of major internal organs in various treatment groups. Histological examination of the heart, liver, spleen, and kidney harvested from ApoE$^{-/-}$ mice with advanced atherosclerotic plaques that were subject to different treatments shows no appreciable change in tissue morphology. Representative images were chosen from n = 6–8 mice per group, across 3 experiments.

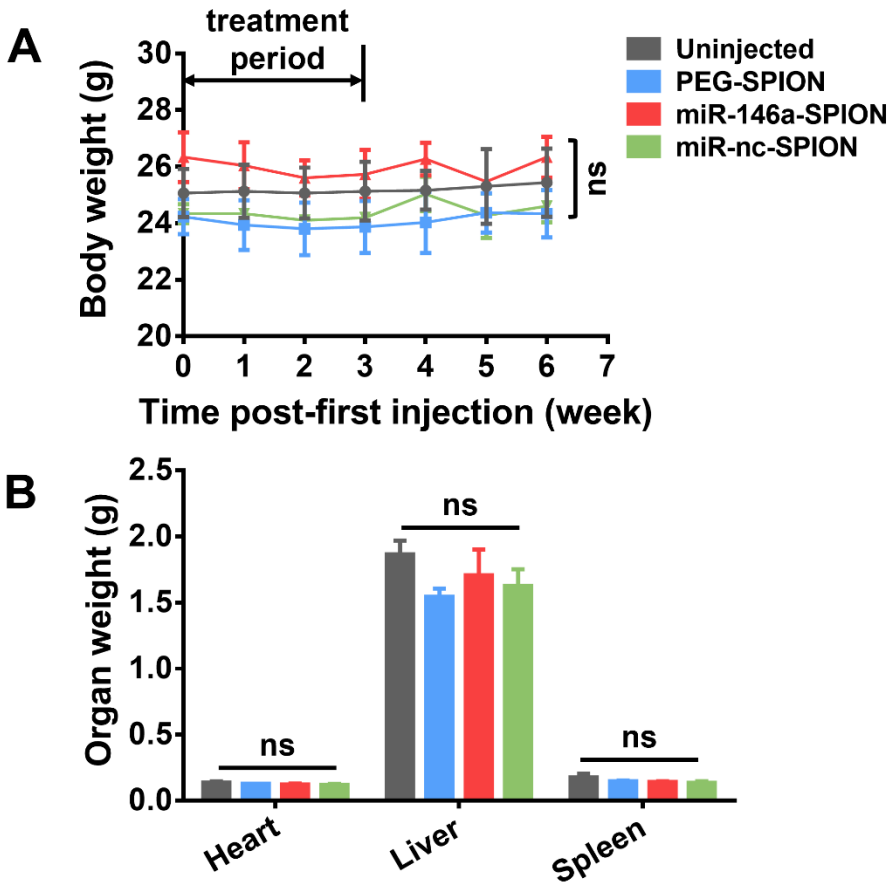

Fig. S37. *In vivo* long-term toxicity of various types of SPIONs following a complete treatment in ApoE$^{-/-}$ mice. The treatment includes 6 doses over a period of 3 weeks, followed by a 4-week treatment period to observe the effect of treatment on long-term toxicity. (**A**) Body weight of mice from various treatment groups throughout the treatment and 4 weeks post-treatment period. (**B**) Weight of major organs of all treatment groups. Data are presented as means ± SEM. Statistical significance was calculated by one-way ANOVA with Tukey's Test for post-hoc analysis, ns: not significant ($P > 0.05$). n = 6 mice per group, across 2 experiments.

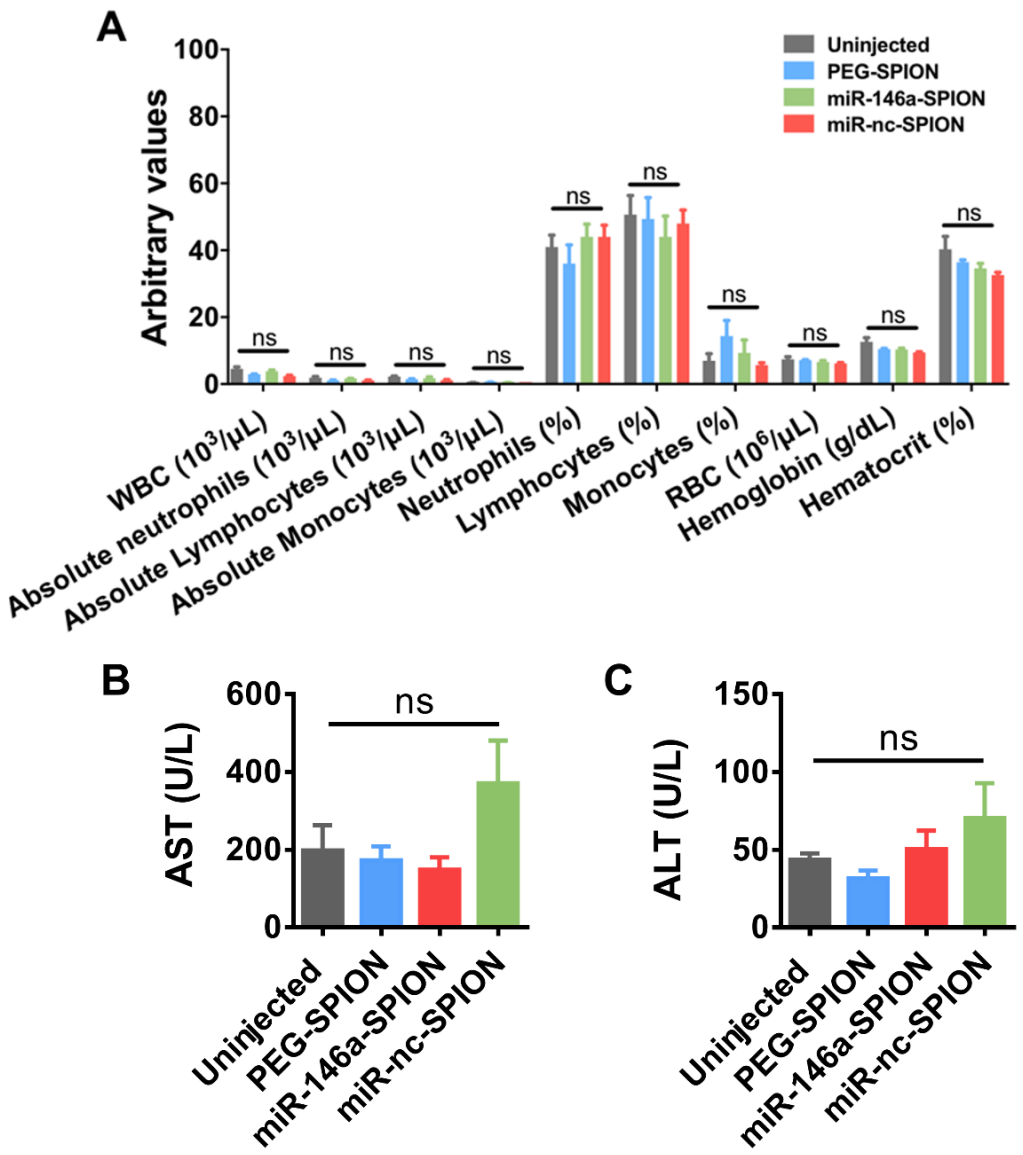

Fig. S38. *In vivo* long-term toxicity of various types of SPIONs following a complete treatment in ApoE$^{-/-}$ mice by complete blood cell count and liver function. The treatment includes 6 doses over a period of 3 weeks, followed by a 4-week treatment period to observe the effect of treatment on long-term toxicity. (**A**) Compared to uninjected mice (black), PEG-SPIONs (blue), miR-146a-SPIONs (red), or miR-nc-SPIONs (green) showed no significant difference in blood chemistry markers or cell counts. WBC: white blood cell. RBC: red blood cell. Absolute neutrophils, lymphocytes, or monocytes (10^3/μL): cell number per volume of blood. Neutrophils %, lymphocytes %, monocytes %: percentage cells among total WBC. RBC (10^6/μL): cell number per volume of blood. Data are presented as mean ± SEM. Statistical significance was calculated by one-way ANOVA with Tukey's Test for post-hoc analysis, ns: not significant ($P > 0.05$). Liver toxicity examined by measuring levels of serum (**B**) aspartate aminotransferase (AST) and (**C**) alanine transaminase (ALT). Data are presented as means ± SEM. Statistical significance was calculated by one-way ANOVA with Tukey's Test for post-hoc analysis, ns: not significant ($P > 0.05$). n = 3 mice per group, across 1 experiment.

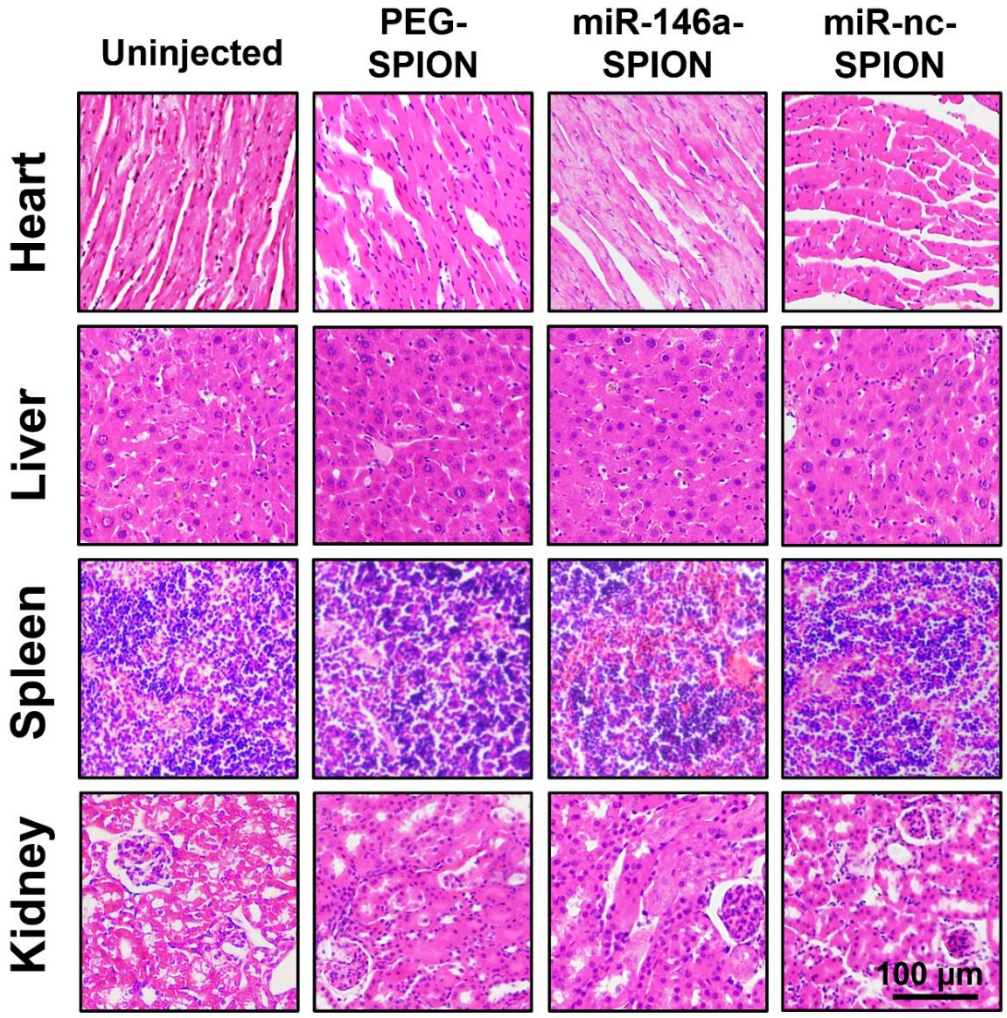

Fig. S39. *In vivo* long-term toxicity of various types of SPIONs following a complete treatment in ApoE$^{-/-}$ mice by histological examination. The treatment includes 6 doses over a period of 3 weeks, followed by a 4-week treatment period to observe the effect of treatment on long-term toxicity. Histological examination of the heart, liver, spleen, and kidney harvested from ApoE$^{-/-}$ mice with advanced atherosclerotic plaques that were subject to different treatments showed no appreciable change in tissue morphology. Representative images were chosen from n = 6 mice per group, across 2 experiments.

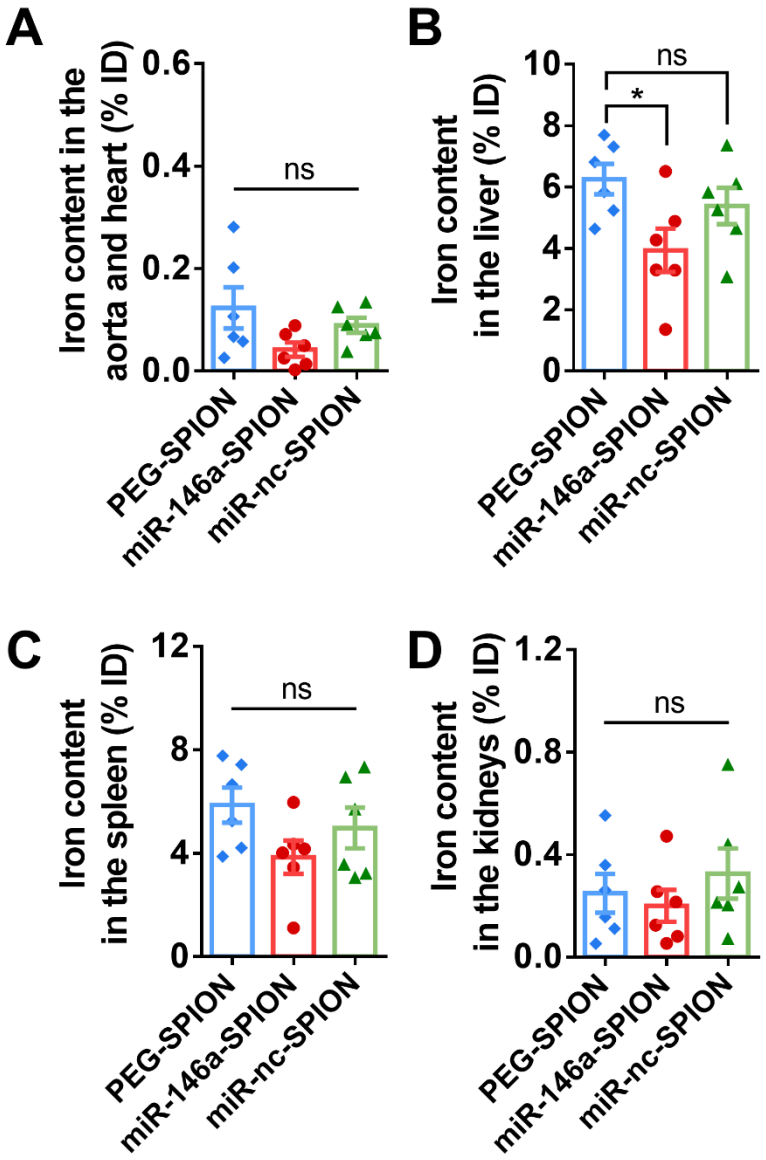

Fig. S40. *In vivo* long-term clearance of various types of SPIONs following a complete treatment in ApoE$^{-/-}$ mice. The treatment includes 6 doses over a period of 3 weeks. Four weeks after the treatment, major organs such as (**A**) aorta and heart, (**B**) liver, (**C**) spleen and (**D**) kidneys were collected after sacrificing the mice for ICP-MS measurement. The iron contents in these major organs four-week after treatment are lower than those in the same organs 24 h after a single injection (Fig. S22). Data are presented as means ± SEM. Statistical significance was calculated by one-way ANOVA with Tukey's Test for post-hoc analysis. ns: not significant ($P > 0.05$), *$P<0.05$. n = 6 mice per group, across 2 experiments.

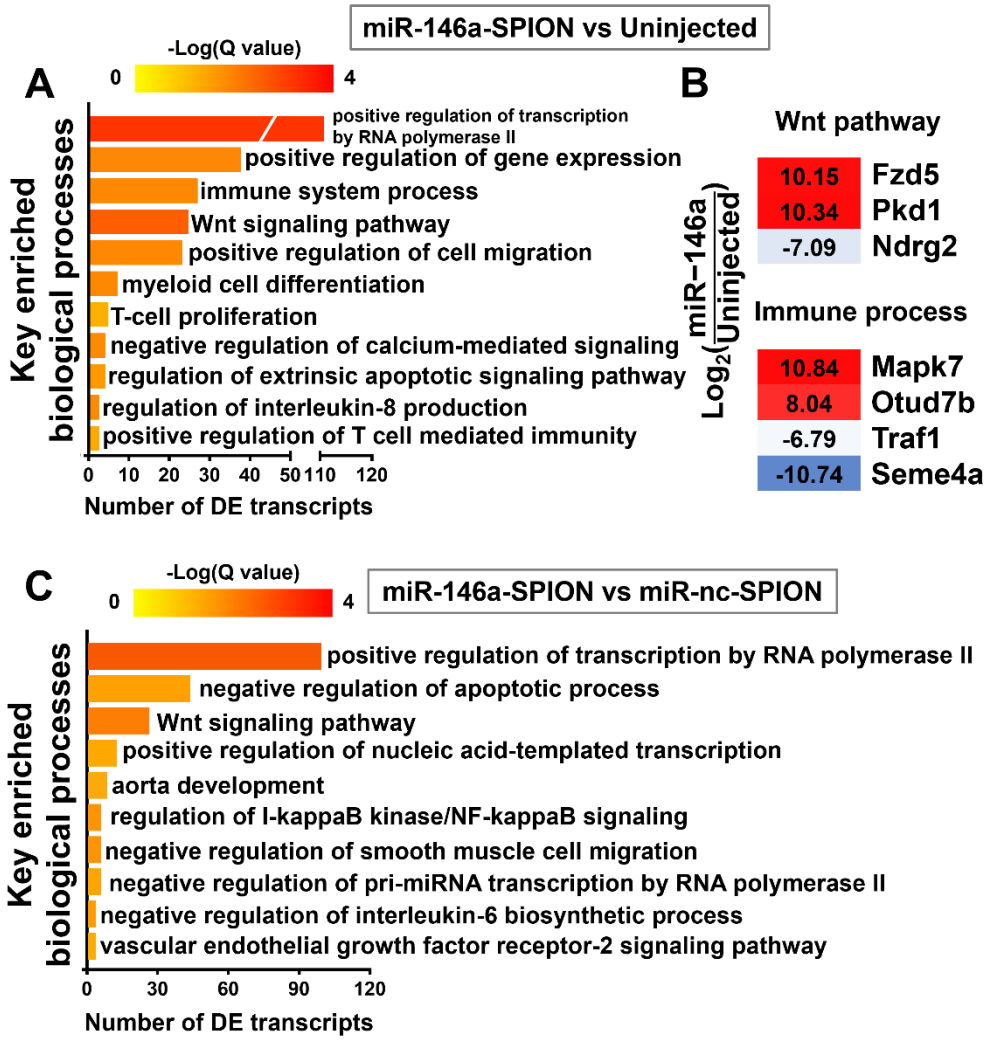

Fig. S41. Statistically enriched gene ontology (GO) terms. Key enriched biological processes found by comparing the (**A**) "miR-146a-SPION" group to the "Untreated" group and (**C**) "miR-146a-SPION" group to the "miR-nc-SPION" group. n=3; Q < 0.05. (**B**) Representative DETs found in the comparison between "miR-146a-SPION" and "Uninjected" groups indicate the effect of miR-146a-SPION treatment on gene expression. Panels A and C corresponds to the pairwise comparisons listed on Tables S5 and S6, respectively. Panel B also shows representative DETs found in comparisons between "miR-146a-SPION" and "Untreated" groups.

Table S4. Enriched biological process found in the pairwise comparison "miR-146a-SPION" vs "PEG-SPION" (Q value < 0.05).

GO_ Biological Process	Q value
phosphorylation	5.27554E-08
positive regulation of transcription, DNA-templated	0.00041
positive regulation of cell migration	0.00059
positive regulation of transcription by RNA polymerase II ##	0.00059
negative regulation of transcription by RNA polymerase II	0.00082
chromatin organization	0.00082
regulation of cardiac muscle cell proliferation	0.00109
positive regulation of GTPase activity	0.00170
peptidyl-serine phosphorylation	0.00345
positive regulation of gene expression ##	0.00373
embryonic hemopoiesis	0.01158
rhythmic process	0.01158
endocytosis	0.01221
innate vocalization behavior	0.01221
anoikis	0.01956
ventricular trabecula myocardium morphogenesis	0.02045
cellular response to tumor necrosis factor ##	0.02148
interleukin-21 secretion ##	0.02148
ubiquitin-dependent protein catabolic process	0.02471
Wnt signaling pathway ##	0.02471
peptidyl-threonine phosphorylation	0.02471
interleukin-1 alpha production ##	0.02471
endothelial cell activation ##	0.02471
positive regulation of proteasomal protein catabolic process	0.02471
NLRP1 inflammasome complex assembly ##	0.02471
cellular response to ionomycin	0.02504
pre-B cell differentiation	0.02956
positive regulation of multicellular organism growth	0.03183
regulation of protein binding	0.03183
regulation of monocyte differentiation ##	0.03183
negative regulation of transcription, DNA-templated	0.03183
regulation of macrophage colony-stimulating factor production ##	0.03183
immune system process ##	0.03741
forebrain development	0.03741
homeostasis of number of cells	0.03741
positive regulation of epithelial cell proliferation	0.03741
cardiovascular system development	0.03741
regulation of non-motile cilium assembly	0.03781
osteoclast development	0.04145
regulation of I-kappaB kinase/NF-kappaB signaling ##	0.04145
regulation of defense response to bacterium	0.04208
positive regulation of apoptotic signaling pathway ##	0.04350
negative regulation of interleukin-6 biosynthetic process ##	0.04525
protein phosphorylation	0.04553
striatum development	0.04553
lung secretory cell differentiation	0.04553
regulation of lung goblet cell differentiation	0.04553
negative regulation of lung goblet cell differentiation	0.04553
angiogenesis	0.04588
chemokine (C-C motif) ligand 2 secretion ##	0.04635
regulation of protein complex assembly	0.04635
T follicular helper cell differentiation ##	0.04635
positive regulation of hydrogen peroxide-induced cell death	0.04635

cerebral cortex development	0.04676
mammary gland epithelial cell proliferation	0.04676
lateral mesoderm development	0.04676
smooth muscle tissue development	0.04676
pigment granule localization	0.04676
pigment granule transport	0.04676
regulation of neural crest cell differentiation	0.04676
regulation of neural crest cell fate specification	0.04676
lipid metabolic process ##	0.04791
N-acetylneuraminate metabolic process	0.04809
sensory perception	0.04998
positive regulation of endothelial cell migration ##	0.04998
heart formation	0.04998

Note: The lines indicated by "##" are the enriched biological processes shown in Fig. 5B that are directly related to the anti-atherosclerosis efficacy of the miR-146a-coating.

Table S5. Enriched biological process found in the pairwise comparison "miR-146a-SPION" vs "Untreated" (Q value < 0.05).

GO_Biological Process	Q value
positive regulation of transcription by RNA polymerase II ##	0.00065
chromatin organization	0.00281
Wnt signaling pathway ##	0.00281
post-embryonic development	0.00601
response to denervation involved in regulation of muscle adaptation	0.00855
positive regulation of protein tyrosine phosphatase activity	0.00956
immune system process ##	0.01186
myeloid cell differentiation ##	0.01186
positive regulation of cell migration ##	0.01186
regulation of heart growth	0.01186
positive regulation of gene expression ##	0.01255
phosphorylation	0.01411
multicellular organism growth	0.01457
regulation of humoral immune response mediated by circulating immunoglobulin	0.01474
regulation of B cell proliferation	0.01474
regulation of interleukin-8 production ##	0.01474
plasma membrane raft distribution	0.01474
negative regulation of calcium-mediated signaling ##	0.01474
positive regulation of antigen receptor-mediated signaling pathway	0.01474
immunoglobulin biosynthetic process	0.01985
ubiquitin-dependent protein catabolic process	0.02497
digestive tract development	0.02853
histone H4 deacetylation	0.02853
regulation of extrinsic apoptotic signaling pathway ##	0.02853
B cell differentiation	0.03145
embryonic camera-type eye development	0.03611
response to gamma radiation	0.03909
actin polymerization or depolymerization	0.03921
regulation of cell cycle	0.03921
positive regulation of hematopoietic stem cell migration	0.03921
protein O-linked glycosylation	0.03979
regulation of gene expression	0.03979
positive regulation of ARF protein signal transduction	0.03979
mammary gland epithelial cell proliferation	0.03979
positive regulation of transcription, DNA-templated	0.03979
regulation of protein tyrosine kinase activity	0.04028
embryonic organ development	0.04053
positive regulation of GTPase activity	0.04234
reproductive structure development	0.04234
positive regulation of T cell mediated immunity ##	0.04321
angiogenesis involved in wound healing	0.04321
protein polyubiquitination	0.04642
glandular epithelial cell development	0.04642
negative regulation of cell adhesion involved in substrate-bound cell migration	0.04642
visceral muscle development	0.04642
negative regulation of interleukin-2 biosynthetic process	0.04642
SCF-dependent proteasomal ubiquitin-dependent protein catabolic process	0.04716
positive regulation of stem cell proliferation	0.04716
histone deacetylation	0.04774
brain renin-angiotensin system	0.0478
T cell proliferation ##	0.0478
regulation of myeloid cell differentiation	0.0478

regulation of B cell receptor signaling pathway	0.0478
embryonic placenta morphogenesis	0.0478
cellular response to BMP stimulus	0.0478

Note: The lines indicated by "##" are the enriched biological processes shown in Fig. S41A that are directly related to the anti-atherosclerosis efficacy of the miR-146a-SPIONs.

Table S6. Enriched biological process found in the pairwise comparison "miR-146a-SPION" vs "miR-nc-SPION" (Q value < 0.05).

GO_Biological Process	Q value
chromatin organization	0.00160
hematopoietic stem cell proliferation	0.00160
phosphorylation	0.00260
positive regulation of transcription by RNA polymerase II ##	0.00260
histone deacetylation	0.00778
embryonic placenta development	0.00868
positive regulation of MAPK cascade ##	0.00893
Wnt signaling pathway	0.01691
positive regulation of GTPase activity	0.01709
ubiquitin-dependent protein catabolic process	0.02047
negative regulation of smooth muscle cell migration ##	0.02047
histone H4 deacetylation	0.02047
negative regulation of pri-miRNA transcription by RNA polymerase II ##	0.02047
regulation of insulin-like growth factor receptor signaling pathway	0.02107
cell motility involved in cerebral cortex radial glia guided migration	0.02146
protein deacetylation	0.02224
protein ubiquitination	0.02224
secretory granule organization	0.02224
vascular endothelial growth factor receptor-2 signaling pathway ##	0.02224
reelin-mediated signaling pathway	0.02224
proteasome-mediated ubiquitin-dependent protein catabolic process	0.02224
rhythmic process	0.02224
negative regulation of blood pressure	0.02702
protein polyubiquitination	0.02813
regulation of growth	0.02813
negative regulation of cellular protein catabolic process	0.02841
heterochromatin assembly	0.03311
negative regulation of apoptotic process ##	0.03382
positive regulation of nucleic acid-templated transcription ##	0.04001
cell cycle	0.04244
positive regulation of transcription, DNA-templated	0.04244
positive regulation of protein autoubiquitination	0.04244
wound healing	0.04308
skeletal system development	0.04614
lysosome organization	0.04614
phospholipid transport	0.04614
aorta development ##	0.04614
regulation of I-kappaB kinase/NF-kappaB signaling ##	0.04614
regulation of stress fiber assembly	0.04614
positive regulation of neuron migration	0.04614
negative regulation of interleukin-6 biosynthetic process ##	0.04698

Note: The lines indicated by "##" are the enriched biological processes shown in Fig. S41C that are directly related to the anti-atherosclerosis efficacy of the miR-146a-SPIONs.

SI References

1. L. Zhang *et al.*, Promoting the delivery of nanoparticles to atherosclerotic plaques by DNA coating. *ACS Appl. Mater. Interfaces* **11**, 13888–13904 (2019).
2. M. Nahrendorf *et al.*, Noninvasive vascular cell adhesion molecule-1 imaging identifies inflammatory activation of cells in atherosclerosis. *Circulation* **114**, 1504–1511 (2006).
3. A. Maiseyeu *et al.*, In vivo targeting of inflammation-associated myeloid-related protein 8/14 via gadolinium immunonanoparticles. *Arterioscler. Thromb. Vasc. Biol.* **32**, 962–970 (2012).
4. A. L. de Barros *et al.*, Assessment of global cardiac uptake of radiolabeled iron oxide nanoparticles in apolipoprotein-E-deficient mice: implications for imaging cardiovascular inflammation. *Mol. Imaging Biol.* **16**, 330–339 (2014).
5. M. D. Majmudar *et al.*, Polymeric nanoparticle PET/MR imaging allows macrophage detection in atherosclerotic plaques. *Circ. Res.* **112**, 755–761 (2013).
6. S. Wen *et al.*, In vivo MRI detection of carotid atherosclerotic lesions and kidney inflammation in ApoE-deficient mice by using LOX-1 targeted iron nanoparticles. *Nanomedicine* **10**, 639–649 (2014).
7. J. Tang *et al.*, Inhibiting macrophage proliferation suppresses atherosclerotic plaque inflammation. *Sci. Adv.* **1**, e1400223 (2015).
8. H. P. Luehmann, *et al.*, PET/CT imaging of chemokine receptors in inflammatory atherosclerosis using targeted nanoparticles. *J. Nucl. Med.* **57**, 1124–1129 (2016).
9. J. Tang *et al.*, Immune cell screening of a nanoparticle library improves atherosclerosis therapy. *Proc. Natl. Acad. Sci. U. S. A.* **113**, E6731–E6740 (2016).
10. P. Chhour *et al.*, Labeling monocytes with gold nanoparticles to track their recruitment in atherosclerosis with computed tomography. *Biomaterials* **87**, 93–103 (2016).
11. T. J. Beldman *et al.*, Hyaluronan nanoparticles selectively target plaque-associated macrophages and improve plaque stability in atherosclerosis. *ACS Nano* **11**, 5785–5799 (2017).
12. C. Jiang *et al.*, Dynamically enhancing plaque targeting via a positive feedback loop using multifunctional biomimetic nanoparticles for plaque regression. *J. Control. Release* **308**, 71–85 (2019).
13. S. H. Nasr *et al.*, Effective atherosclerotic plaque inflammation inhibition with targeted drug delivery by hyaluronan conjugated atorvastatin nanoparticles. *Nanoscale* **12**, 9541–9556 (2020).
14. K. M. Tsoi, *et al.*, Mechanism of hard-nanomaterial clearance by the liver. *Nat. Mater*. **15**, 1212–1221 (2016).